

Jordan Journal of P H Y S I C S

An International Peer-Reviewed Research Journal

Volume 11, No. 3, December 2018, Rabi Al-Thani 1440 H

Jordan Journal of Physics (JJP): An International Peer-Reviewed Research Journal funded by the Scientific Research Support Fund, Jordan, and published biannually by the Deanship of Research and Graduate Studies, Yarmouk University, Irbid, Jordan.

EDITOR-IN-CHIEF:

Ibrahim O. Abu Al-Jarayesh

Department of Physics, Yarmouk University, Irbid, Jordan.

ijaraysh@yu.edu.jo

EDITORIAL BOARD:	ASSOCIATE EDITORIAL BOARD
<p>Prof. Dia-Eddin M. Arafah <i>Department of Physics, University of Jordan, Amman, Jordan.</i> <i>darafah@ju.edu.jo</i></p> <p>Prof. Nabil Y. Ayoub <i>President, American University of Madaba, Madaba, Jordan.</i> <i>nabil.ayoub@giu.edu.jo</i></p> <p>Prof. Jamil M. Khalifeh <i>Department of Physics, University of Jordan, Amman, Jordan.</i> <i>jkalifa@ju.edu.jo</i></p> <p>Prof. Sami H. Mahmood <i>Department of Physics, University of Jordan, Amman, Jordan.</i> <i>s.mahmood@ju.edu.jo</i></p> <p>Prof. Nihad A. Yusuf <i>Department of Physics, Yarmouk University, Irbid, Jordan.</i> <i>nihadyusuf@yu.edu.jo</i></p> <p>Prof. Marwan S. Mousa <i>Department of Physics, Mu'tah University, Al-Karak, Jordan.</i> <i>mmousa@mutah.edu.jo</i></p> <p>Prof. Akram A. Rousan <i>Department of Applied Physical Sciences, Jordan University Of Science and Technology, Irbid, Jordan.</i> <i>akram@just.edu.jo</i></p> <p>Prof. Mohammad Al-Sugheir <i>Department of Physics, The Hashemite University, Zarqa, Jordan.</i> <i>msugh@hu.edu.jo</i></p>	<p>Prof. Mark Haggmann <i>Desert Electronics Research Corporation, 762 Lacey Way, North Salt Lake 84064, Utah, U. S. A.</i> <i>MHaggmann@NewPathResearch.Com</i></p> <p>Prof. Richard Forbes <i>University of Surrey, FEPS (X1), Guildford, Surrey GU2 7XH, U. K.</i> <i>R.Forbes@surrey.ac.uk</i></p> <p>Prof. Roy Chantrell <i>Physics Department, The University of York, York, YO10 5DD, UK.</i> <i>roy.chantrell@york.ac.uk</i></p> <p>Prof. Susamu Taketomi <i>2-35-8 Higashisakamoto, Kagoshima City, 892-0861, Japan.</i> <i>staketomi@hotmail.com</i></p>

Editorial Secretary: Majdi Al-Shannaq.

Languages Editor: Haider Al-Momani

Manuscripts should be submitted to:

Prof. Ibrahim O. Abu Al-Jarayesh
Editor-in-Chief, Jordan Journal of Physics
Deanship of Research and Graduate Studies
Yarmouk University-Irbid-Jordan
Tel. 00 962 2 7211111 Ext. 2075
E-mail: jjp@yu.edu.jo
Website: <http://Journals.yu.edu.jo/jjp>

Jordan Journal of PHYSICS

An International Peer-Reviewed Research Journal

Volume 11, No. 3, December 2018, Rabi Al-Thani 1440 H

INTERNATIONAL ADVISORY BOARD

Prof. Dr. Ahmad Saleh

Department of Physics, Yarmouk University, Irbid, Jordan.
salema@yu.edu.jo

Prof. Dr. Aurore Savoy-Navarro

*LPNHE Université de Paris 6/IN2P3-CNRS, Tour 33, RdC 4,
Place Jussieu, F 75252, Paris Cedex 05, France.*
auore@lpnhep.in2p3.fr

Prof. Dr. Bernard Barbara

*Laboratoire Louis Neel, Salle/Room: D 108, 25, Avenue des
Martyrs BP 166, 38042-Grenoble Cedex 9, France.*
Barbara@grenoble.cnrs.fr

Prof. Dr. Bruno Guiderdoni

*Observatoire Astronomique de Lyon, g, avenue Ch. Antre-F-69561,
Saint Genis Laval Cedex, France.*
Bruno.guiderdoni@olos.univ-lyon1.fr

Prof. Dr. Buford Price

*Physics Department, University of California, Berkeley, CA 94720,
U. S. A.*
bprice@berkeley.edu

Prof. Dr. Colin Cough

*School of Physics and Astronomy, University of Birmingham, B15
2TT, U. K.*
c.gough@bham.ac.uk

Prof. Dr. Desmond Cook

*Department of Physics, Condensed Matter and Materials Physics
Research Group, Old Dominion University, Norfolk, Virginia
23529, U. S. A.*
Dcook@physics.odu.edu

Prof. Dr. Evgeny Sheshin

MIPT, Institutskij per. 9, Dogoprudnyi 141700, Russia.
sheshin@lafeet.mipt.ru

Prof. Dr. Hans Ott

*Laboratorium Fuer Festkorperphysik, ETH Honggerberg, CH-
8093 Zurich, Switzerland.*
ott@solid.phys.ethz.ch

Prof. Dr. Herwig Schopper

*President SESAME Council, Chairman Scientific Board UNESCO
IBSP Programme, CERN, 1211 Geneva, Switzerland.*
Herwig.Schopper@cern.ch

Prof. Dr. Humam Ghassib

*Department of Physics, The University of Jordan, Amman 11942,
Jordan.*
humamg@ju.edu.jo

Prof. Dr. Khalid Touqan

Chairman of Jordan Atomic Energy Commission, Amman, Jordan.

Prof. Dr. Nasr Zubeidey

President: Al-Zaytoonah University of Jordan, Amman, Jordan.
President@alzaytoonah.edu.jo

Prof. Dr. Patrick Roudeau

*Laboratoire de l'Accelérateur, Lineaire (LAL), Université Paris-
Sud 11, Batiment 200, 91898 Orsay Cedex, France.*
roudeau@mail.cern.ch

Prof. Dr. Paul Chu

*Department of Physics, University of Houston, Houston, Texas
77204-5005, U. S. A.*
Ching-Wu.Chu@mail.uh.edu

Prof. Dr. Peter Dowben

*Nebraska Center for Materials and Nanoscience, Department of
Physics and Astronomy, 255 Behlen Laboratory (10th and R
Streets), 116 Brace Lab., P. O. Box 880111, Lincoln, NE 68588-
0111, U. S. A.*
pdowben@unl.edu

Prof. Dr. Peter Mulser

*Institute fuer Physik, T.U. Darmstadt, Hochschulstr. 4a, 64289
Darmstadt, Germany.*
Peter.mulser@physik.tu-darmstadt.de

Prof. Dr. Rasheed Azzam

*Department of Electrical Engineering, University of New Orleans
New Orleans, Louisiana 70148, U. S. A.*
razzam@uno.edu

Prof. Dr. Shawqi Al-Dallal

*Department of Physics, Faculty of Science, University of Bahrain,
Manamah, Kingdom of Bahrain.*

Prof. Dr. Wolfgang Nolting

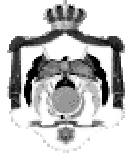
*Institute of Physics / Chair: Solid State Theory, Humboldt-
University at Berlin, Newtonstr. 15 D-12489 Berlin, Germany*
Wolfgang.nolting@physik.hu-berlin.de

Prof. Dr. Ingo Hofmann

GSI Darmstadt, Planckstr. 1, 64291, Darmstadt, Germany.
i.hofmann@gsi.de

Prof. Dr. Jozef Lipka

*Department of Nuclear Physics and Technology, Slovak University
of Technology, Bratislava, Ilkovicova 3, 812 19 Bratislava,
Slovakia.*
Lipka@elf.stuba.sk



The Hashemite Kingdom of Jordan



Yarmouk University

Jordan Journal of
PHYSICS

An International Peer-Reviewed Research Journal
Funded by the Scientific Research Support Fund

Volume 11, No. 3, December 2018, Rabi Al-Thani 1440 H

Instructions to Authors

Instructions to authors concerning manuscript organization and format apply to hardcopy submission by mail, and also to electronic online submission via the Journal homepage website (<http://jjp.yu.edu.jo>).

Manuscript Submission

1- **E-mail to :** jjp@yu.edu.jo

2- **Online:** Follow the instructions at the journal homepage website.

Original *Research Articles*, *Communications* and *Technical Notes* are subject to critical review by minimum of two competent referees. Authors are encouraged to suggest names of competent reviewers. *Feature Articles* in active Physics research fields, in which the author's own contribution and its relationship to other work in the field constitute the main body of the article, appear as a result of an invitation from the Editorial Board, and will be so designated. The author of a *Feature Article* will be asked to provide a clear, concise and critical status report of the field as an introduction to the article. *Review Articles* on active and rapidly changing Physics research fields will also be published. Authors of *Review Articles* are encouraged to submit two-page proposals to the Editor-in-Chief for approval. Manuscripts submitted in *Arabic* should be accompanied by an Abstract and Keywords in English.

Organization of the Manuscript

Manuscripts should be typed double spaced on one side of A4 sheets (21.6 x 27.9 cm) with 3.71 cm margins, using Microsoft Word 2000 or a later version thereof. The author should adhere to the following order of presentation: Article Title, Author(s), Full Address and E-mail, Abstract, PACS and Keywords, Main Text, Acknowledgment. Only the first letters of words in the Title, Headings and Subheadings are capitalized. Headings should be in **bold** while subheadings in *italic* fonts.

Title Page: Includes the title of the article, authors' first names, middle initials and surnames and affiliations. The affiliation should comprise the department, institution (university or company), city, zip code and state and should be typed as a footnote to the author's name. The name and complete mailing address, telephone and fax numbers, and e-mail address of the author responsible for correspondence (designated with an asterisk) should also be included for official use. The title should be carefully, concisely and clearly constructed to highlight the emphasis and content of the manuscript, which is very important for information retrieval.

Abstract: A one paragraph abstract not exceeding 200 words is required, which should be arranged to highlight the purpose, methods used, results and major findings.

Keywords: A list of 4-6 keywords, which expresses the precise content of the manuscript for indexing purposes, should follow the abstract.

PACS: Authors should supply one or more relevant PACS-2006 classification codes, (available at <http://www.aip.org/pacs/pacs06/pacs06-toc.html>)

Introduction: Should present the purpose of the submitted work and its relationship to earlier work in the field, but it should not be an extensive review of the literature (e.g., should not exceed 1 ½ typed pages).

Experimental Methods: Should be sufficiently informative to allow competent reproduction of the experimental procedures presented; yet concise enough not to be repetitive of earlier published procedures.

Results: should present the results clearly and concisely.

Discussion: Should be concise and focus on the interpretation of the results.

Conclusion: Should be a brief account of the major findings of the study not exceeding one typed page.

Acknowledgments: Including those for grant and financial support if any, should be typed in one paragraph directly preceding the References.

References: References should be typed double spaced and numbered sequentially in the order in which they are cited in the text. References should be cited in the text by the appropriate Arabic numerals, enclosed in square brackets. Titles of journals are abbreviated according to list of scientific periodicals. The style and punctuation should conform to the following examples:

1. Journal Article:

- a) Heisenberg, W., Z. Phys. 49 (1928) 619.
- b) Bednorz, J. G. and Müller, K. A., Z. Phys. B64 (1986) 189
- c) Bardeen, J., Cooper, L.N. and Schrieffer, J. R., Phys. Rev. 106 (1957) 162.
- d) Asad, J. H., Hijjawi, R. S., Sakaji, A. and Khalifeh, J. M., Int. J. Theor. Phys. 44(4) (2005), 3977.

2. Books with Authors, but no Editors:

- a) Kittel, C., "Introduction to Solid State Physics", 8th Ed. (John Wiley and Sons, New York, 2005), chapter 16.
- b) Chikazumi, S., C. D. Graham, JR, "Physics of Ferromagnetism", 2nd Ed. (Oxford University Press, Oxford, 1997).

3. Books with Authors and Editors:

- a) Allen, P. B. "Dynamical Properties of Solids", Ed. (1), G. K. Horton and A. A. Maradudin (North-Holland, Amsterdam, 1980), p137.
- b) Chantrell, R. W. and O'Grady, K., "Magnetic Properties of Fine Particles" Eds. J. L. Dormann and D. Fiorani (North-Holland, Amsterdam, 1992), p103.

4. Technical Report:

Purcell, J. "The Superconducting Magnet System for the 12-Foot Bubble Chamber", report ANL/HEP6813, Argonne Natl. Lab., Argonne, III, (1968).

5. Patent:

Bigham, C. B., Schneider, H. R., US patent 3 925 676 (1975).

6. Thesis:

Mahmood, S. H., Ph.D. Thesis, Michigan State University, (1986), USA (Unpublished).

7. Conference or Symposium Proceedings:

Blandin, A. and Lederer, P. Proc. Intern. Conf. on Magnetism, Nottingham (1964), P.71.

8. Internet Source:

Should include authors' names (if any), title, internet website, URL, and date of access.

9. Prepublication online articles (already accepted for publication):

Should include authors' names (if any), title of digital database, database website, URL, and date of access.

For other types of referenced works, provide sufficient information to enable readers to access them.

Tables: Tables should be numbered with Arabic numerals and referred to by number in the Text (e.g., Table 1). Each table should be typed on a separate page with the legend above the table, while explanatory footnotes, which are indicated by superscript lowercase letters, should be typed below the table.

Illustrations: Figures, drawings, diagrams, charts and photographs are to be numbered in a consecutive series of Arabic numerals in the order in which they are cited in the text. Computer-generated illustrations and good-quality digital photographic prints are accepted. They should be black and white originals (not photocopies) provided on separate pages and identified with their corresponding numbers. Actual size graphics should be provided, which need no further manipulation, with lettering (Arial or Helvetica) not smaller than 8 points, lines no thinner than 0.5 point, and each of uniform density. All colors should be removed from graphics except for those graphics to be considered for publication in color. If graphics are to be submitted digitally, they should conform to the following minimum resolution requirements: 1200 dpi for black and white line art, 600 dpi for grayscale art, and 300 dpi for color art. All graphic files must be saved as TIFF images, and all illustrations must be submitted in the actual size at which they should appear in the journal. Note that good quality hardcopy original illustrations are required for both online and mail submissions of manuscripts.

Text Footnotes: The use of text footnotes is to be avoided. When their use is absolutely necessary, they should be typed at the bottom of the page to which they refer, and should be cited in the text by a superscript asterisk or multiples thereof. Place a line above the footnote, so that it is set off from the text.

Supplementary Material: Authors are encouraged to provide all supplementary materials that may facilitate the review process, including any detailed mathematical derivations that may not appear in whole in the manuscript.

Revised Manuscript and Computer Disks

Following the acceptance of a manuscript for publication and the incorporation of all required revisions, authors should submit an original and one more copy of the final disk containing the complete manuscript typed double spaced in Microsoft Word for Windows 2000 or a later version thereof. All graphic files must be saved as PDF, JPG, or TIFF images.

Allen, P.B., “.....”, in: Horton, G.K., and Muradudin, A. A., (eds.), “Dynamical.....”, (North.....), pp....

Reprints

Twenty (20) reprints free of charge are provided to the corresponding author. For orders of more reprints, a reprint order form and prices will be sent with the article proofs, which should be returned directly to the Editor for processing.

Copyright

Submission is an admission by the authors that the manuscript has neither been previously published nor is being considered for publication elsewhere. A statement transferring copyright from the authors to Yarmouk University is required before the manuscript can be accepted for publication. The necessary form for such transfer is supplied by the Editor-in-Chief. Reproduction of any part of the contents of a published work is forbidden without a written permission by the Editor-in-Chief.

Disclaimer

Opinions expressed in this Journal are those of the authors and neither necessarily reflects the opinions of the Editorial Board or the University, nor the policy of the Higher Scientific Research Committee or the Ministry of Higher Education and Scientific Research. The publisher shoulders no responsibility or liability whatsoever for the use or misuse of the information published by JJP.

Indexing

JJP is currently indexing in:

	Emerging Sources Citation Index (ESCI)	
---	---	---

Jordan Journal of
P H Y S I C S

An International Peer-Reviewed Research Journal

Volume 11, No. 3, December 2018, Rabi Al-Thani 1440 H

Table of Contents:

English Articles	Pages
M1 and E2 Transitions in the Ground-State Levels of Neutral Tin Leyla Özdemir and Muhammed Serkan Şadoğlu	141-145
Study of Optical and Structural Properties of NiO Thin Films Prepared by Chemical Spray Pyrolysis (CSP) Method Mutaz Salih Hasan Aljuboori	147-152
Comparison of Different Models of Size-Dependent Thermodynamic Properties of Nanoparticles Abdulrhman Kh. Suliman	153-160
Compton Scattering of Twisted Light Mazen Nairat and L. David Voelz	161-166
Neon Soft X-Ray Yield Optimization from NX2 Dense Plasma Focus Device Walid Sahyouni and Alaa Nassif	167-172
Natural Radioactivity and Associated Radiation Hazards in Local Portland and Pozzolanic Cements Used in Jordan Mefleh S. Hamideen	173-179
Optical Constants Determination of Thermally-Evaporated Undoped Lead Iodide Films from Transmission Spectra Using the PUMA Method Mahmoud H. Saleh	181-191
Radiological Risk Measurements Due to Natural Radioactivity of Building Stones Used in Jordanian Houses H. Saleh, M. Hamideen, M. Al-Hwaiti and S. Al-Kharoof	193-200
Technical Note	Pages
Optical Properties of Chemically Synthesized Cadmium Sulphide for Solar Cell Applications M. A. SALAWU, A. B. ALABI, S. B. SHARAF A and T. AKOMOLAFE	201-207

M1 and E2 Transitions in the Ground-State Levels of Neutral Tin

Leyla Özdemir and Muhammed Serkan Şadoğlu

Department of Physics, Sakarya University, 54187 Sakarya, Turkey.

Received on: 3/7/2017;

Accepted on: 28/12/2017

Abstract: We have reported the magnetic dipole (M1) and electric quadrupole (E2) transition parameters such as transition energies, logarithmic weighted oscillator strengths and transition probabilities between the fine structure levels in the ground-state configuration of $5s^25p^2$ for neutral tin (Sn I, $Z=50$) using the multiconfiguration Hartree-Fock approximation within the framework of the Breit-Pauli Hamiltonian (MCHF+BP). The results obtained for Sn I have been compared with other available results. Also, new results on oscillator strengths for Sn I have been presented.

Keywords: Energies, Forbidden transitions, Configuration interaction, Relativistic effects.

PACS: 31.15.ag, 31.15.am, 31.15.ve, 31.30.jc, 31.30.jp.

Introduction

Although the atomic kinetics depend, in particular, on optical allowed transitions, electric dipole (E1), the weak forbidden transitions (in particular, magnetic dipole, M1 and electric quadrupole, E2) have been linked to dominant features in the optical spectra of planetary nebulae and aurora [1-3]. M1 and E2 transition rates (or probabilities) are of several orders of magnitude smaller than those for E1 transitions with a similar energy-level separation.

The forbidden transition lines (especially, magnetic dipole, M1, and electric quadrupole, E2) have great importance in astrophysics which includes the determination of the elemental abundances in different celestial objects and also in laboratory astrophysics and plasma physics studies, since they carry valuable information such as thermal Doppler effects of heavenly bodies. These lines are particularly sensitive to the collisional de-excitation and serve as indicators of electron density and temperature in the emission spectrum. They are used as the best diagnostic tools in both astrophysics and laboratory plasma research [4].

The aim of this work is to investigate the forbidden transitions (M1 and E2) between the fine structure energy levels within the ground state configuration of atomic tin (Sn I, $Z=50$) using the multiconfiguration Hartree-Fock (MCHF) approach within the framework of the Breit-Pauli Hamiltonian [5]. Sn I has the ground state configuration of [Pd] $5s^25p^2$. There are a few works on forbidden transitions (M1 and E2) [6-9], whereas the allowed transitions (electric dipole, E1) (for example, [10-14]) are widely investigated in literature. In calculations, we have selected the configuration set for including valence correlation effect. Other correlation methods (core and core-valence correlations) produce a lot of states, and in this case, the convergence problems in the radial functions occur. For valence correlation, we have only taken into account the configurations including one electron excitation from valence to other high subshells: $5s^25p^2$, $5s5p^25d$, $5s^25d^2$, $5p^25d^2$, $5s^25p5f$, $5p^4$, $5s^25p4f$, $5p^24f^2$, $5p^34f$, $5p^35f$, $5p^25f^2$, $5s^24f^2$ and $5s5p^26s$. Since the parity of upper and lower levels within the ground state configuration is the same, the electric dipole (E1) transitions are forbidden. The lowest-order

metastable levels radiatively decay corresponding to magnetic dipole (M1) and electric quadrupole (E2) transitions. M1 and E2 transition rates are several orders of magnitude smaller than those for electric dipole (E1) transitions with a similar energy level separation.

Computational Procedure

A detail of theoretical background on radiative transitions can be also found in the

$$A^{\pi k}(\gamma'J', \gamma J) = 2C_k \left[\alpha (E_{\gamma'J'} - E_{\gamma J}) \right]^{2k+1} \frac{S^{\pi k}(\gamma'J', \gamma J)}{g_{J'}}, \quad (1)$$

where $g_{J'}$ denotes statistical weight of the upper level; namely $g_{J'} = 2J' + 1$ and $S^{\pi k}$ is the line strength,

$$S^{\pi k}(\gamma'J', \gamma J) = \left| \langle \gamma J \| \mathbf{O}^{\pi(k)} \| \gamma'J' \rangle \right|^2, \quad (2)$$

$C_k = (2k+1)(k+1)/k((2k+1)!)^2$ and $\mathbf{O}^{\pi(k)}$ is the transition operator which describes each multipole. The transition probabilities for forbidden transitions depend on the third (in M1

$$f^{\pi k}(\gamma J, \gamma'J') = \frac{1}{\alpha} C_k \left[\alpha (E_{\gamma'J'} - E_{\gamma J}) \right]^{2k-1} \frac{S^{\pi k}(\gamma J, \gamma'J')}{g_J}. \quad (3)$$

A similar expression can be written for the emission oscillator strength, where $\gamma'J'$ and γJ are interchanged, making the emission oscillator strength negative. The weighted oscillator strength, or gf -value, is completely symmetrical (except sign) between the two levels. The weighted oscillator strength is given by:

$$gf^{\pi k}(\gamma'J', \gamma J) = g_{J'} f^{\pi k}(\gamma'J', \gamma J). \quad (4)$$

The weighted oscillator strength or gf -value is an important property. The intensity of the spectral line is proportional to the line strength and also to the gf -value.

In the MCHF method, the wave function (or atomic state function, ASF) in the equations above is expressed as a linear combination of configuration state functions (CSFs) $\Phi(\gamma_i LS)$,

$$\Psi(\gamma LS) = \sum_{i=1}^M c_i \Phi(\gamma_i LS), \quad \sum_{i=1}^M c_i^2 = 1, \quad (5)$$

where γ represents electronic configuration. The mixing coefficients c_i and the one-electron radial wave functions of Φ are obtained in a

literature (for example, [5, 15]). If the emitted or observed photon has angular momentum k and parity $\pi = (-1)^k$, the transition is an electric multipole transition (Ek), while the transition from absorbed photon with parity $\pi = (-1)^{k+1}$ is a magnetic multipole transition (Mk).

The transition probability (or rate) for the emission from the upper level to the lower level is given by:

transition) or fifth (in E2 transition) power of transition energy.

The oscillator strength is a dimensionless quantity. It expresses the probability of absorption or emission of electromagnetic radiation in transitions between energy levels. For absorption, the oscillator strength is expressed by:

self-consistent procedure by optimization of the energy function based on the non-relativistic Hamiltonian of an atom,

$$H_{NR} = \sum_{j=1}^N \left(\frac{1}{2} \nabla_j^2 - \frac{Z}{r_j} \right) + \sum_{j < k} \frac{1}{r_{jk}}. \quad (6)$$

In this method, the relativistic effects were included as a first-order correction to the MCHF approximation by evaluating Breit-Pauli Hamiltonian using CI method [16]. The Breit-Pauli Hamiltonian consists of a non-relativistic many-electron Hamiltonian (H_{NR}), a relativistic shift Hamiltonian (H_{RS}) including a mass correction, one- and two-body Darwin terms, a spin-spin contact term, an orbit-orbit term; and fine structure Hamiltonian (H_{FS}) including spin-orbit, spin-other-orbit and spin-spin terms. A detail for these terms in the Breit-Pauli Hamiltonian can be found in reference [5] (in Chapter 7). Also, this method includes correlation effects between electrons together with relativistic effects. The wave functions are obtained as a linear combination of CSFs in LSJ coupling and the matrix eigenvalue problem becomes:

$$\mathbf{H}\mathbf{c} = E\mathbf{c}, \quad (7)$$

where \mathbf{H} is the Hamiltonian matrix with elements

$$H_{ij} = \langle \gamma_i L_i S_i J M | H_{BP} | \gamma_j L_j S_j J M \rangle \quad (8)$$

and $\mathbf{c} = (c_1, \dots, c_M)^t$ is the column vector of the expansion coefficients. The Breit-Pauli Hamiltonian is a first-order perturbation correction to the non-relativistic Hamiltonian.

Results and Discussion

In this work, the results of transition energies, ΔE (in cm^{-1}), logarithmic weighted oscillator strengths (or logarithmic gf-value, $\log(\text{gf})$) and transition probabilities, A_{ki} (s^{-1}), for magnetic dipole, M1 and electric quadrupole, E2 transitions between the fine structure levels of the ground-state configuration $5s^25p^2$ in Sn I have been reported using the MCHF atomic-structure package [17]. In calculations, the correlation and relativistic effects in the framework of the Breit-Pauli Hamiltonian mentioned in section Computational Procedure have been considered. M1 and E2 transitions combine the states with the same parity. Therefore, we have taken into account the configurations of $5s^25p^2$, $5s5p^25d$, $5s^25d^2$, $5p^25d^2$, $5s^25p5f$, $5p^4$, $5s^25p4f$, $5p^24f^2$, $5p^34f$, $5p^35f$, $5p^25f^2$, $5s^24f^2$ and $5s5p^26s$ outside the core [Pd] for considering correlation effects. In MCHF calculations, for avoiding computer constraints, we have only selected the

states of $^3P_{2, 1, 0}$, 1D_2 and 1S_0 for all considered configurations. These are also the states of the ground-state configuration. We have obtained 139 energy levels including only these states for all of configurations. The transition energies obtained from M1 and E2 transitions between the levels of ground configuration have been listed and compared with [6, 8, 10] in Table 1. We have given $\left(\frac{E_{\text{this work}} - E_{\text{other work}}}{E_{\text{other work}}}\right) \times 100$, where the differences are in per cent (%), for the accuracy of energy results obtained from this work, as presented in Table 1. When the differences (%) between our results and other results have been investigated, the differences with [6], [8] and [10] are in the range of 1.23-18.23, 1.11-16.78 and 0.50-5.12, respectively. In Table 2, we have presented the logarithmic weighted oscillator strengths, $\log(\text{gf})$, and transition probabilities, A_{ki} , for M1 and E2 transitions between the ground levels. The A_{ki} values have been compared with those in [7]. A_{ki} values obtained from this work are in agreement with those obtained from work [7]. The weighted oscillator strength values for these lines from M1 and E2 transitions have been presented here firstly. Atomic tin has a high-Z atom and the correlation effects are dominant for this atom. The transition energy results obtained from this work are in agreement with the values available in literature in general. We have not obtained J-J'=0 transitions due to the constraint in MCHF code.

TABLE 1. Energy differences, ΔE (in cm^{-1}), between the fine structure levels of $5s^25p^2$ in atomic tin (Sn I). A: The differences (%) by comparing with [6], B: The differences (%) by comparing with [8] and C: The differences (%) by comparing with [10].

Transitions	$\Delta E(\text{cm}^{-1})$			A	B	C
	This work	Other works				
$^1D_2 - ^3P_1$	7109	6901 ^a , 6921 ^b , 7034 ^c		3.01	2.71	1.06
$^1D_2 - ^3P_0$	8517	8623 ^a , 8613 ^b , 8475 ^c		1.23	1.11	0.50
$^1D_2 - ^1S_0$	9353	8547 ^a , 8550 ^b , 8897 ^c		9.43	9.39	5.12
$^3P_2 - ^3P_1$	1565	1695 ^a , 1736 ^b , 1628 ^c		7.66	9.85	3.86
$^3P_2 - ^3P_0$	2973	3417 ^a , 3428 ^b , 3069 ^c		12.99	13.27	3.12
$^3P_2 - ^1S_0$	14897	13753 ^a , 13735 ^b , 14303 ^c		8.31	8.46	4.15
$^3P_1 - ^3P_0$	1408	1722 ^a , 1692 ^b , 1441 ^c		18.23	16.78	2.19
$^3P_1 - ^1S_0$	16461	15448 ^a , 15471 ^b , 15931 ^c		6.56	6.40	3.33

^a[6], ^b[8], ^c[10]

TABLE 2. Logarithmic weighted oscillator strengths, $\log(gf)$, and transition probabilities, A_{ki} (s^{-1}), for the magnetic dipole (M1) and electric quadrupole (E2) transitions between the fine structure levels of $5s^25p^2$ in atomic tin (Sn I). The numbers in brackets represent the power of 10.

Transitions		$\log(gf)$	A_{ki}	
		This work	This work	Other works
$^3P_1 - ^1D_2$	E2	-9.3	1.548 (-3)	4.710 (-3) ^a , 4.3(-3) ^b
	M1	-7.44	2.435(-1)	4.518 (-1) ^a , 4.6(-1) ^b
$^3P_0 - ^1D_2$	E2	-10.3	5.231 (-5)	1.654 (-4) ^a , 8.1(-5) ^b
	M1	-	-	-
$^1D_2 - ^1S_0$	E2	-7.9	0.79	1.155 ^a , 0.95 ^b
	M1	-	-	-
$^3P_1 - ^3P_2$	E2	-10.08	1.305 (-5)	3.742(-5) ^a , 3.6(-5) ^b
	M1	-6.9	4.185(-2)	5.926(-2) ^a , 6.2(-2) ^b
$^3P_0 - ^3P_2$	E2	-9.6	1.628(-4)	6.842(-4) ^a , 5.9(-4) ^b
	M1	-	-	-
$^3P_2 - ^1S_0$	E2	-8.8	2.406 (-1)	6.831(-1) ^a , 5.7(-1) ^b
	M1	-	-	-
$^3P_0 - ^3P_1$	E2	-	-	-
	M1	-7.0	4.267(-2)	8.903 (-2) ^a , 8.3(-2) ^b
$^3P_1 - ^1S_0$	E2	-	-	-
	M1	-7.7	4.288	7.076 ^a , 7.0 ^b

^a[6], ^b[7]

Conclusion

Through a systematic MCHF study within the framework of the Breit-Pauli Hamiltonian of transition energies, logarithmic weighted oscillator strengths and transition probabilities for the magnetic dipole, M1 and electric quadrupole, E2 transitions between the fine structure levels of $[Pd]5s^25p^2$ ground state configuration of neutral tin (Sn I, $Z=50$) have been reported. There is a requirement of atomic data of neutral tin, even its charged ions, to understand the erosion of vessel wall tiles in fusion power plants [1], in special, and for plasma diagnostics and modeling. These ground state levels perform weak spectral lines and they decay *via* magnetic dipole (M1) and electric quadrupole (E2) transitions. It is seen that there is an agreement when comparing our results with

those presented in other available works. Some differences among other works [6-8, 10] also appear. The studies on M1 and E2 transition parameters, such as oscillator strengths and transition probabilities for Sn I, are limited in number in the literature. Hence, we hope that the results obtained from this work will be useful for other works in the future for Sn I spectrum and provide support to further research on this atom.

Acknowledgments

The authors are very grateful to the anonymous reviewers for stimulating comments and valuable suggestions, which resulted in improving the paper.

References

- [1] Zou, Y. and Fischer, C.F., *J. Phys. B: At. Mol. Opt. Phys.*, 34 (2001) 915.
- [2] Trabert, E., *Phys. Scr.*, 61 (2000) 257.
- [3] Hu, F., Wang, C., Yang, J., Jiang G. and Hao L., *Phys. Scr.*, 84 (2011) 015302.
- [4] Dixit, G., Sahoo, B.K., Chaudhuri, R.K. and Majumder, S., *J. Phys. B: At. Mol. Opt. Phys.*, 42 (2009) 165702.
- [5] Fischer, C.F., Brage, T. and Jönsson, P., "Computational atomic structure-an MCHF approach", (IOP, 1997).
- [6] Biemont, E., Hansen, J.E., Quinet, P. and Zeippen, C.J., *Astron. Astrophys. Suppl. Ser.*, 111 (1995) 333.
- [7] Garstang, R.H., *J. Res. Nat. Bur. Stand.*, 68A (1964) 61.
- [8] Moore, C.E., "Atomic Energy Levels", Vol. III, NBS Circ. 467 (Washington D.C., 1958).
- [9] Ovechkin, G.V., Bakhtovarshoev, Sh. and Sandrigailo, L.E., *J. Appl. Spectrosc.*, 7 (1967) 309.
- [10] Oliver, P. and Hibbert, A., *J. Phys. B: At. Mol. Opt. Phys.*, 41(2008) 165003.
- [11] Sharma, L., Bharti, S. and Srivastava R., *Eur. Phys. J. D*, 71 (2017) 121.
- [12] Iqbal, J., Ahmed, R., Rafique, M., Anwarul-Haq, M. and Baig, M.A., *Laser Phys.*, 26 (2016) 076001.
- [13] Jiang, L-Y., Wang, Q., Pei, S.H., Feng, Y.Y., Zhang, J.R., Yu, X.C. and Dai, Z.W., *J. Opt. Soc. Am. B*, 29 (2012) 1486.
- [14] Alonso-Medina, A., *Spectrochim. Acta Part B*, 65 (2010) 158.
- [15] Cowan, R.D., "The Theory of Atomic Structure and Spectra", (California, USA, 1981).
- [16] Rudzikas, Z., "Theoretical Atomic Spectroscopy", (Cambridge University Press, New York, USA, 2007).
- [17] Fischer, C.F., *Comput. Phys. Commun.*, 128 (2000) 635.

Study of Optical and Structural Properties of NiO Thin Films Prepared by Chemical Spray Pyrolysis (CSP) Method

Mutaz Salih Hasan Aljuboori

Department of Physics, College of Education for Pure Science, University of Mosul, Mosul, Iraq.

Received on: 10/9/2017;

Accepted on: 23/4/2018

Abstract: In this study, NiO thin films with molarity of 0.1 M have been successfully deposited on glass substrates by chemical spray pyrolysis (CSP) technique at a substrate temperature of 400 °C and a deposited thickness of about 350 nm. The structural and optical properties of these films have been studied using Ultraviolet-visible (UV-Visible) spectroscopy and X ray diffraction (XRD). The absorbance and transmittance spectra have been recorded in the wavelength range of 300-900 nm in order to study the optical properties. The optical energy gap for allowed direct electronic transition was calculated using Tauc's equation. It is found that the band gap is equal to 3.58 eV for the prepared thin films. The optical constants, including absorption coefficient, were also calculated as a function of photon energy. Refractive index and extinction coefficient for the prepared thin films were estimated as a function of wavelength in the wavelength range 300-900 nm. The XRD results showed that the studied films are polycrystalline in nature with a cubic structure and a preferred orientation along (111) plane. The average crystallite size of the film was estimated for (111) direction by Scherrer formula and was equal to ~ 10nm.

Keywords: Thin film, NiO, Optical properties, CSP, XRD.

Introduction

Nickel(II) oxide is a chemical compound with the formula NiO. It is notable as being the only well characterized oxide of nickel. The mineralogical form of NiO, bunsenite, is very rare. NiO can be prepared using different methods. Upon heating above 400 °C, nickel powder reacts with oxygen to give NiO. In some commercial processes, green nickel oxide is made by heating a mixture of nickel powder and water at 1000 °C. The rate for this reaction can be increased by the addition of NiO [1]. The simplest and most successful method of preparation is through pyrolysis for compounds of nickel (II), such as: hydroxide, nitrate and carbonate, which yields a light green powder. The synthesis from the elements by heating the metal in oxygen can yield grey to black powders, which indicates nonstoichiometry [2]. NiO adopts the NaCl structure, with octahedral Ni(II)

and O₂. Nickel oxide (NiO) has a density of 6.67g/cm³, a molecular weight of 74.69 g/mol and a melting point of 1955 °C [3]. Nickel oxide thin films have different applications, such as: an antiferromagnetic material [4], p-type transparent conducting films [5], electro catalysis, positive electrode in batteries, fuel cell, a material for electro-chromic display devices and solar thermal absorbers [6].

Experimental Procedure

Chemical spray pyrolysis technique was used to deposit NiO thin films on glass substrates at a temperature of 400 °C. In the preparation of NiO films, an aqueous solution with a molarity of 0.1M was prepared Ni(NO₃)₂·6H₂O and mixed with distilled water by using a magnetic stirrer for 40 minutes. The resultant solution was sprayed on glass substrates. Other deposition

conditions, such as spray nozzle substrate distance (30 cm), spray interval (2 minutes) and pressure (p bar), were kept constant for each concentration. The X-ray diffraction patterns for the prepared films were obtained by using a Shimadzu XRD-6000 diffractometer using copper target (Cu K α , 1.5418 Å) and optical properties in the wavelength range of 300-900 nm were investigated by using a Shimadzu UV-1800 UV-Visible spectrophotometer.

Results and Discussion

Optical Analysis

The optical absorption spectra of the films in the spectral range of 300-900 nm were recorded by using UV-Visible spectrophotometer. The analysis of the dependence of absorption

coefficient on photon energy in the high absorption regions is performed to obtain the detailed information on the energy band gaps of the films [1]. Fig. 1a shows the relation between transmittance and wavelength for Nickel Oxide thin films. From this figure, the transmittance increases with wavelength. The spectrum shows a high transmittance in the visible and infrared regions and a low transmittance in the ultraviolet region. Fig. 1b shows the relation between absorbance (A) and wavelength for the deposited thin films. The absorbance decreases rapidly at short wavelengths corresponding to the energy gap of the film. This evident increase of energy is due to the interaction of the material electrons with the incident photons which have enough energy for the occurrence of electron transitions.

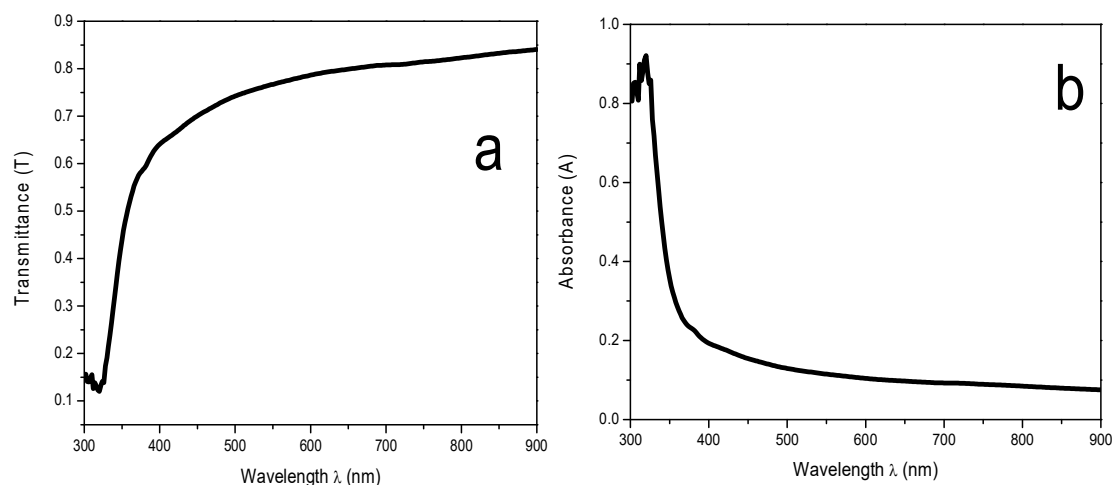


FIG. 1a. Transmittance (T), b. Absorbance (A) versus wavelength (λ) for Nickel Oxide thin film.

The absorption coefficient can be estimated from the absorbance using the well-known formula [7]:

$$\alpha = (2.303 \times A)/t, \quad (1)$$

where A is the absorbance, t is the thickness and α is the absorption coefficient. It has been noticed that all the prepared thin films have a high absorption coefficient in the visible range of the spectrum and this could be seen in Fig. 2. The absorption coefficient increases with the increase in photon energy ($h\nu$). The optical energy band gap (E_g) is given by the well known Tauc's relation [7]:

$$\alpha h\nu = A(h\nu - E_g)^r \quad (2)$$

where α is the absorption coefficient, $h\nu$ is the photon energy, E_g is the optical band gap, A is a constant which does not depend on photon energy and r has four numeric values (1/2) for allowed direct, 2 for allowed indirect, 3 for forbidden direct and 3/2 for forbidden indirect optical transitions. In this work, direct band gap was determined by plotting a graph between $(\alpha h\nu)^2$ and $(h\nu)$ in eV units, where a straight line is obtained which gives the value of the direct band gap. The extrapolation of straight line to $(\alpha h\nu)^2 = 0$ gives the value of the direct band gap of the material and this could be seen in Fig. 3. From this figure, the band gap value is equal to 3.58eV, which is in agreement with Sriram and Thaymanavan [8].

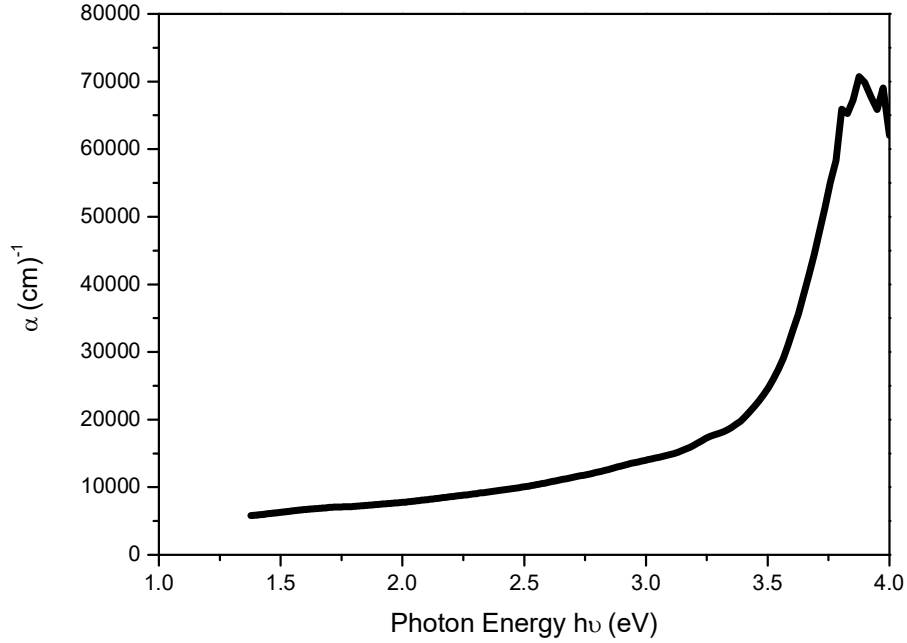


FIG. 2. Absorption coefficient *versus* photon energy for Nickel Oxide thin films.

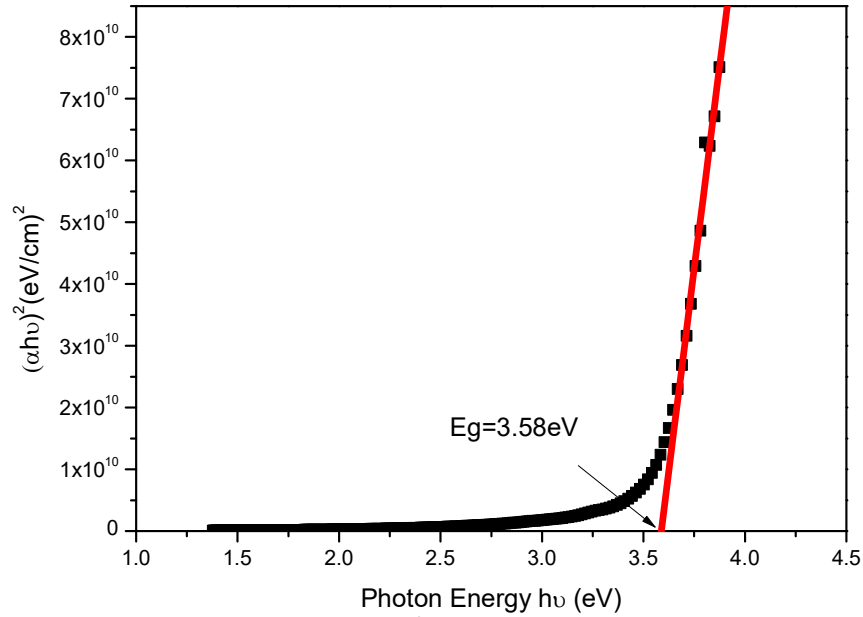


FIG.3. The relation between $(\alpha h\nu)^2$ and $(h\nu)$ for Nickel Oxide thin film.

The refractive index has been calculated using the relation [1]:

$$n = \left[\frac{(1+R)^2}{(1-R)^2} - (k_o^2 - 1) \right]^{1/2} + \frac{(1+R)}{(1-R)} \quad (3)$$

where, n : is the refractive index, R : is the reflectance (calculated from $R + A + T = 1$) and k_o : is the extinction coefficient. The relation between refractive index and wavelength for

NiO thin films is shown in Fig. 4a. It can be seen that the refractive index of the prepared films decreases with the increase in wavelength, which is in agreement with other reports [1, 9].

The extinction coefficient (k_o) was calculated using the relation [10]:

$$k_o = \frac{\alpha\lambda}{4\pi} \quad (4)$$

where: k_o is the extinction coefficient and λ : is the wavelength of the incident photon. The extinction coefficient (k_o) decreases rapidly at short wavelengths (300-400) nm and after that the value of (k_o) remains almost constant. The

rise and fall in the value of (k_o) is directly related to the absorption of light. In Fig. 4 (b), the lower value of (k_o) in the wavelength range (400-900) nm implies that these films absorb light in this region very easily.

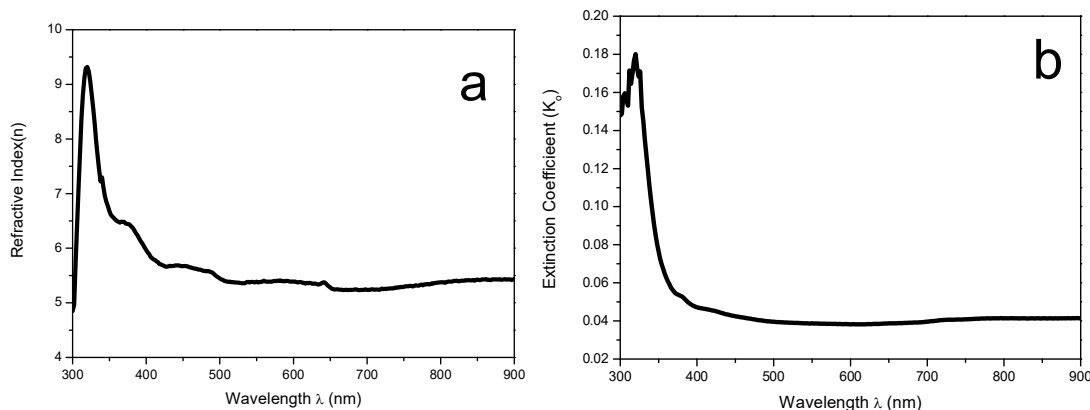


FIG.4a. Refractive index. b. Extinction coefficient versus wavelength of Nickel Oxide thin films.

Structural Analysis

XRD patterns of the nickel oxide films is shown in Fig. 5. It can be noticed that all the patterns exhibit diffraction peaks around ($2\theta \sim 37^\circ$, 43° and 63°) referred to (111), (200) and (220) favorite directions, respectively, which is in agreement with the Joint Committee of Powder Diffraction Standards (JCPDS) card number (04-0835). The strongest peak occurs at ($2\theta \sim 37^\circ$), which is referred to as (111) plane,

which is in agreement with Khoder *et al.* [7]. The positions of the peaks and the presence of more than one diffraction peak lead to the conclusion that the films are polycrystalline in nature with a cubic crystalline structure, which is in agreement with other reports [11]. The lattice constant is ($a_o = 4.179 \text{ \AA}$). It should be mentioned here that the standard a_o value for NiO is (4.176 \AA).

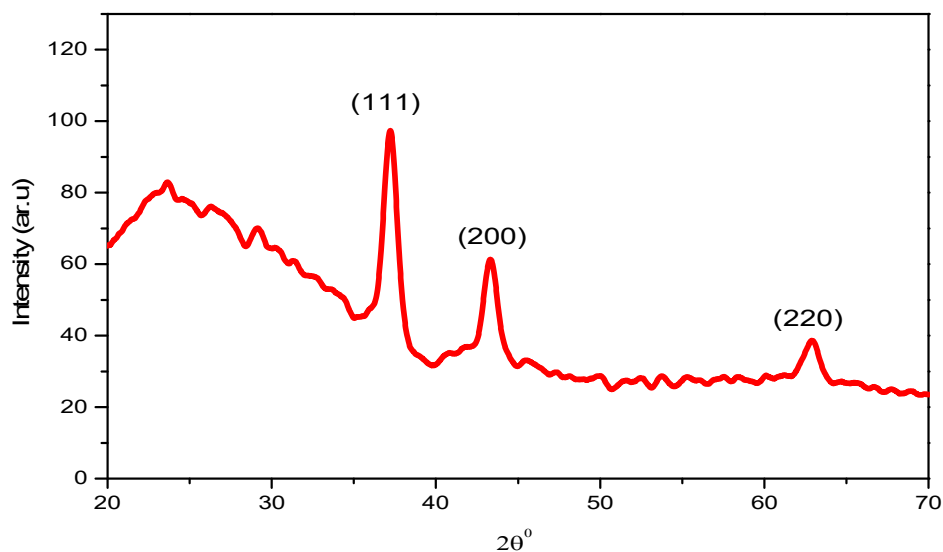


Figure 5. XRD patterns of Nickel Oxide thin films.

The average crystallite size for the films can be determined using Williamson-Hall (WH) formula [9]:

$$\beta_{hkl} \cos \theta = k\lambda / D + 4 S \sin \theta \quad (5)$$

where β_{hkl} is full width of half maximum, D is the average crystallite size, k is a constant which

was assumed to be equal to 0.9, λ is the wavelength for the Cu target of the XRD instrument, θ is Bragg's angle for all peaks and S is the micro-strain in the film. If $\beta_{hkl}\cos\theta$ is plotted with respect to $4\sin\theta$, strain and

crystallite size can be calculated from the slope and y-intercept of the fitted line, respectively, as shown in Fig. 6. It is observed that the crystallite size value is equal to (7.38 nm) and ($S=-0.00411$).

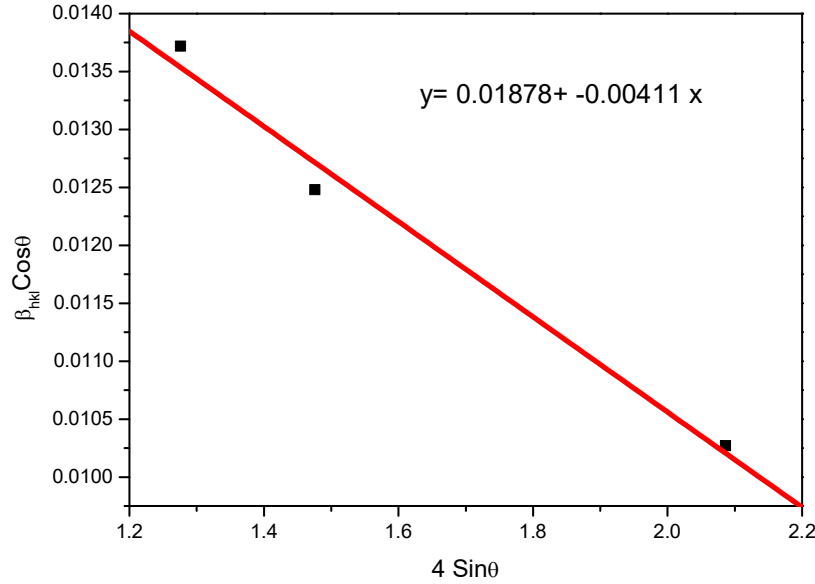


FIG. 6. The W-H analysis of NiO thin film.

The average crystallite size for all the films is also calculated for (111) direction by Scherrer's formula [11]:

$$D_{av} = k\lambda / \beta \cos\theta \quad (6)$$

where:

k : is a constant which was assumed to be equal to 0.9.

λ : is the wavelength of incident X-ray radiation, ($\lambda = 1.5406 \text{ \AA}$ for $\text{CuK}\alpha$).

β : is the full width at half maximum of the peak (in radians).

θ : is Bragg's diffraction angle of the XRD peak.

It is observed that the crystallite size for the Nickel Oxide thin films is 10 nm. These results agree qualitatively with the results of crystallite size obtained by Williamson-Hall method. The micro-strain in the films is induced during the growth of thin films by varying displacements of the atoms with respect to their reference lattice position [1]. The larger crystallite size values indicate better crystallization of the films; values of micro-strain were negative, which indicates the occurrence of compression in the lattice.

The texture coefficient (T_c) represents the texture of a particular plane, in which greater than unity values imply that there are numerous

grains in that particular direction. The texture coefficients $T_c(hkl)$ for the sample have been calculated from the X-ray data using the well-known formula [7]:

$$T_c(hkl) = \frac{I(hkl)/I_0(hkl)}{N_r^{-1} \sum I(hkl)/I_0(hkl)} \quad (7)$$

where, $I(hkl)$ is the measured intensity, $I_0(hkl)$ is taken from the JCPDS data, (N_r) is the reflection number and (hkl) represents Miller indices. The texture coefficient is calculated for crystal plane (111) of the NiO films. The value of texture coefficient was greater than 1, which indicates the abundance of grains in the (111) direction.

The Specific Surface Area (SSA) is the Surface Area (SA) per unit mass. It is a very important factor in the field of nanoparticles because of large surface to volume ratio of such small particle size materials. SSA is used in materials to determine their types and also used in case of reactions on surfaces, heterogeneous catalysis and adsorption. Mathematically, SSA can be calculated using the formula [12]:

$$SSA = 6 \times 10^3 / D \cdot \rho \quad (8)$$

where, D is the crystallite size (W-H and Scherrer) and ρ is the density of NiO (6.67 g/cm^3).

The values of the Specific Surface Area from W-H is equal to (121901m²/g) and from Scherrer is equal to (89955m²/g). According to Eq.(8), the Specific Surface Area increases with decreasing the crystallite size. There is an inverse relation between them so that Specific Surface Area was large.

Conclusion

In this study, NiO thin films with a molarity of 0.1 M were successfully deposited on glass substrates at (400 °C) by chemical spray

pyrolysis technique using Nickel nitrates as the Ni source. XRD patterns of the NiO thin films indicate that all films are polycrystalline with a cubic crystal structure. The main characteristic peaks are assigned to the (111), (200) and (220) planes and the transmittance for NiO thin films increases when wavelength increases. The band gap value is (3.58 eV).

References

- [1] Bakr, N.A., Salman, S.A. and Shano, A.M., *International Journal of Current Research*, 6 (2014) 9644.
- [2] Greenwood, N. and Earnshaw, A., "Chemistry of the Elements". (Oxford, Pergamon Press,1984).
- [3] Lascelles, K., Morgan, L.G., Nicholls, D. and Beyersmann, D., "Nickel Compounds", in: "Ullmann's Encyclopedia of Industrial Chemistry", (Wiley-VCH, Weinheim, 2005).
- [4] Fujii, E., Tomozawa, A., Torii, H. and Takayama, R., *Jpn. J. Appl. Phys.*, 35 (1996) 328.
- [5] Sato, H., Minami, T., Takata, S. and Yamada, T., *Thin Solid Films*, 236 (1993) 27.
- [6] Cerc Korosec, R., Bukovec, P., Pihlar, B., Surca Vuk, A., Orel, B. and Drazic, G., *Solid State Ionics*, 165(1-4) (2003) 191.
- [7] Khodair, Z.T., Kamil, A.A. and Abdalaah, Y.K., *Physica B*, 503 (2016) 55.
- [8] Sriram, S. and Thayumanavan, A., *Int. J. Mat. Sci. and Eng.*, 1(2) (2013) 118.
- [9] Ahmed, S.S., Hassan, E.K. and Mohamed, G.H., *International Journal of Advanced Research*, 2(2) (2014) 633.
- [10] Mote, V.D., Purushotham, Y. and Dole, B.N., *Journal of Theoretical and Applied Physics*, 6 (2012) 6.
- [11] Barret, C. and Massalki, T.B., "Structure of Metals", (Oxford Pergamon, 1980).
- [12] Khodair, Z.T., Bakr, N.A. and Mohammed, A.A., *Journal of Chemical, Biological and Physical Sciences*, 6(1) (2015) 145.

Comparison of Different Models of Size-Dependent Thermodynamic Properties of Nanoparticles

Abdulrhman Kh. Suliman

Physics Department. College of Science, Salahaddin University, Erbil, Iraq.

Received on: 8/1/2018;

Accepted on: 10/4/2018

Abstract: Surface and thermodynamic properties, such as enthalpy, cohesive energy, surface energy and melting point, of different materials (Ag, Au, Sn and In) were calculated theoretically in this study by using the following two models: firstly, the lattice vibration-based model (*LVB*) of surface atoms and secondly, the surface-to-volume atom ratio (*SV/A*) model of the free surface nanoparticle material. In this work, the melting temperature and other thermodynamic properties of the modified model of the nanoparticles improved the calculated curve compared with that of the experimental data due to the effect of lattice volume. Results of the two models showed changes in all thermodynamic properties as nanoparticle size decreased. Moreover, compared with the experimental data, a good agreement was observed between the modified *LVB* model and the experimental data.

Keywords: Cohesive energy, Enthalpy, Melting point, Surface energy, Nanoparticles, Size effects.

PACS: 67.25.bd, 65.80.-g.

Introduction

Thermodynamic properties of nanoscale materials are different from those of their corresponding bulk materials [1, 2]. Thus, understanding the surface and thermodynamic properties of nanoscale materials, for instance, crystals in carbon nanotubes and thin films of nanometer thickness, is vital because of their potential applications in microelectronics, nonlinear optics and solar energy [3-6]. The properties of bulk crystals depend on their structure. However, in addition to the structure, their size influences their properties, such as melting point, cohesive energy, entropy, thermal enthalpy, Debye temperature and surface energy, at the nanoscale [7]. Different models have been developed to explain and account for the thermodynamic properties of low-dimensional materials. These models include the liquid drop [8], bond-order-length-strength and latent heat models for size-dependent cohesive energy [9, 10]. These models also include surface area-

different and bond energy model [11], which is also used to predict the melting temperature of nanomaterials [12]. Moreover, a variety of theoretical calculation methods have been used to obtain surface energy of nanoparticles. These calculation methods include the broken-bond rule [13] and the modified embedded atom method [14]. Ouyang *et al.* (2006) and Jiang *et al.* (2010) experimentally measured the surface energies of nanocrystals and showed the dependence of nanoparticle properties on their sizes in metals and semiconductors [15, 7].

One of the important thermodynamic properties is cohesive energy, which determines a wide range of thermophysical properties, including melting point, solubility and surface energy. Surface energy is linear to cohesive energy, whereas cohesive energy is linear to melting point [16, 17]. Moreover, cohesive energy and melting point are parameters used for estimating metallic bond strength. A high

cohesive energy indicates high thermal stability of the materials [18]. Therefore, identifying the melting entropy and enthalpy is important to understand the stability of nanocrystals. Metal nanoparticles have properties intermediate between those of metals and non-metals. In this study, lattice vibration-based (**LVB**) and surface-to-volume atom ratio (**SVR**) models were applied to study the quantities that are dependent on the binding energies of nanocrystals. This investigation was performed to assess the proficiency of a model and showed results that agreed with the experimental data.

Method of Calculation

The first physical model (**LVB**), is used in the present work to derive the size-dependent enthalpy and entropy based on the Mott's expression for the vibrational melting entropy S_{vib} [19]. The second model was **SVR**, which is a simple method that was developed in 2005 by Qi, W.H. [20], who emphasized that phase stability is sensitive to the surface-to-volume ratio of atoms.

Lattice Vibration Based (**LVB**) Model

A physical model for size-dependent melting enthalpy $H_m(r)$ is related to melting temperature $T_m(r)$ and melting entropy $S_m(r)$ which is a function of the specific heat difference between solid and liquid state [19, 21]; therefore, $H_m(r)$ is equal to;

$$H_m(r) = T_m(r) \cdot S_m(r). \quad (1)$$

The modified model for melting temperature of nanoparticles $T_m(r)$ due to the effect of lattice volume can be described by the following relation [22];

$$\frac{T_m(r)}{T_{mb}} = \left(\frac{V(r)}{Vb}\right)^{2/3} \exp\left(\frac{-2S_{mb}}{3R} \frac{1}{r_0-1}\right) \quad (2)$$

where T_{mb} is the bulk melting point, Vb is the bulk lattice volume, R is the ideal gas constant and r_0 denotes the smallest size where there is no structural difference between the solid and the liquid states. At r_0 , all atoms or molecules are located on the bulk surface. r_0 can be extended for different dimensions D ; for nanoparticles $D = 0$, for nanowires $D = 1$ and for thin films $D = 2$. For nanoparticles and nanowires, r is the radius and for thin films, it is the half thickness. The relationship between r_0 and the first solid surface layer height h is shown as [8, 12, 16];

$$r_0 = (3-D) h. \quad (3)$$

For a spherical nanoparticle of $r_0 = 3h$, this value of h represents a length scale characteristic for crystallinity and is called critical radius. Its values for different elements used in this work are found in *Table 1* [23-25].

The size-dependent lattice volume $V(r)$ is calculated as follows; the size-dependent lattice parameter $a(r)$ is obtained from; $a(r) = \frac{4}{\sqrt{3}} dmean(r)$, where $dmean(r)$ is the mean bond length of nanoparticles. Its value for bulk crystal $dmean(\infty)$ is constant for all elements listed in *Table 1*. The mean bond length for nanoparticles is given by the equation [22];

$$dmean(r) = h - \Delta dmean(r). \quad (4)$$

The change of mean bond length with size $\Delta dmean(r)$ is given by;

$$\Delta dmean(r) = \Delta dmean(r_0) \exp\left(\frac{-2S_{mb}}{3R} \frac{1}{r_0-1}\right) \quad (5)$$

where $\Delta dmean(r_0)$ is the maximum increase in the mean bond length $dmean(r)$. Then, lattice volume $V(r)$ of nanoparticles is calculated from the relation [2]; $V(r) = \frac{a(r)^3}{4}$.

Melting entropy $S_m(r)$ can be described by the following expression;

$$\frac{S_m(r)}{S_{mb}} = \left(1 - \frac{1}{r_0-1}\right) \quad (6)$$

where, S_{mb} is the bulk overall melting entropy. The model suggests that the size dependence of the melting entropy for nano-semiconductor nanoparticles is determined by the size dependence of the vibrational part of the melting entropy of nanocrystal S_{vib} , [7, 26]. The melting entropy for metallic and organic crystals is mainly vibrational in nature and $S_{vib} = S_{mb}$, [27]. From Eq. (2) and Eq. (6), size-dependent melting enthalpy $H_m(r)$ from Eq. (1) is expressed as;

$$\frac{H_m(r)}{H_{mb}} = \left(\frac{V(r)}{Vb}\right)^{2/3} \left[\exp\left(\frac{2S_{vib}}{3R} \frac{1}{r_0-1}\right)\right] \cdot \left(1 - \frac{1}{r_0-1}\right) \quad (7)$$

where, H_{mb} is the bulk enthalpy and its value is given in *Table 1*, [7]. It is well known that the bulk melting point of most materials is proportional to their binding energy and their bulk cohesive energy E_{mb} is proportional to their binding energy. Transition entropy term for the

solid-vapor transition related to cohesive energy can be expressed as follows;

$$S_{mb} = E_{mb} / T_{mb}. \quad (8)$$

Bulk cohesive energy E_{mb} at T_{mb} being the bulk solid-vapor transition temperature, size-dependent cohesive energy $E(r)$ is a linear function of melting point and is given to a good approximation as [28];

$$\frac{E(r)}{E_{mb}} = \frac{T_m(r)}{T_{mb}} \cdot \frac{S_m(r)}{S_{mb}}. \quad (9)$$

From Eq. (2) and Eq. (6), size-dependent cohesive energy of nanoparticles is expressed as [17, 30];

$$\frac{E(r)}{E_{mb}} = \left(\frac{V(r)}{V_b}\right)^{2/3} \left[\exp\left(\frac{-2S_{vib}}{3R} \frac{1}{r_0-1}\right) \right] \cdot \left(1 - \frac{1}{r_0-1}\right). \quad (10)$$

The surface energy γ_{mb} is proportional to cohesive energy E_{mb} through the following relation; $\gamma_{mb} = k E_{mb}$, where k is constant and for size-dependent surface energy of nanoscale materials is [19, 31]; $\gamma(r) = k E(r)$. By comparing the equations for (γ_{mb}) and $(\gamma(r))$, the comprehensive equation of surface energy of nanoparticles will be;

$$\frac{\gamma(r)}{\gamma_{mb}} = \frac{E(r)}{E_{mb}}. \quad (11)$$

Therefore,

$$\frac{\gamma(r)}{\gamma_{mb}} = \left(\frac{V(r)}{V_b}\right)^{2/3} \left[\exp\left(\frac{-2S_{vib}}{3R} \frac{1}{r_0-1}\right) \right] \cdot \left(1 - \frac{1}{r_0-1}\right). \quad (12)$$

Surface to Volume Atom Ratio (SVA) Model

A very simple model has been developed and reported in ref. [20], showing the relation between the melting temperature of nanomaterial and bulk as;

$$\frac{T_m(r)}{T_{mb}} = \left(1 - \frac{N}{2n}\right) = \left(1 - \frac{2d}{rc}\right) \quad (13)$$

where N is the number of surface atoms of the structure and n is the total number of atoms. The method to find the rate $N/2n$ for different types of nanomaterials has been introduced by (Qi, 2006) [11, 21]. According to the (SVA)

model [20], $\frac{N}{n}$ is $\frac{4d}{r_c}$, $\frac{8d}{3L}$ and $\frac{4d}{3W}$ for spherical nanoparticles, nanowires and nanofilms, respectively, where d is the atom diameter and r_c is the diameter of spherical nanoparticles. Here, L is the diameter of nanowires and W is the height of solid nanofilms [32].

The relation between crystal vibration entropy S_{vib} and melting point T_{mb} can be described as [32, 33];

$$S_{vib}(r) - S_{mb} = \frac{3R}{2} \ln \frac{T_m(r)}{T_{mb}} = \frac{3R}{2} \ln \left(1 - \frac{2d}{rc}\right) \quad (14)$$

where S_{mb} is the melting entropy of bulk solid crystal. $H_m(r)$ is a linear function of melting point and is given as [9];

$$\frac{H_m(r)}{H_{mb}} = \left(\frac{S_m(r)}{S_{mb}}\right) \cdot \left(\frac{T_m(r)}{T_{mb}}\right). \quad (15)$$

Substituting Eq. (13) in Eq. (14), the size-dependent enthalpy for spherical nanoparticles is;

$$H_m(r) = T_{mb} \left(1 - \frac{2d}{rc}\right) \left[S_{mb} + \frac{3R}{2} \ln \left(1 - \frac{2d}{rc}\right) \right] \quad (16)$$

$$H_m(r) = \left[H_{mb} + \frac{3RT_{mb}}{2} \ln \left(1 - \frac{2d}{rc}\right) \right] \left(1 - \frac{2d}{rc}\right). \quad (17)$$

The linear relation between melting temperature and cohesive energy is [30]; $\frac{E(r)}{E_{mb}} = \frac{T_m(r)}{T_{mb}}$; therefore, size dependence cohesive energy $E(r)$ expression in this model is [15];

$$E(r) = E_{mb} \left(1 - \frac{2d}{rc}\right). \quad (18)$$

The relationship between surface energy and cohesive energy is;

$$\frac{\gamma(D)}{\gamma_b} = \frac{E(r)}{E_{mb}}. \quad (19)$$

By using the value of cohesive energy from Eq. (18) in Eq. (19), size-dependent surface energy for nanoparticles is [19];

$$\gamma(r) = \gamma_b \left(1 - \frac{2d}{rc}\right). \quad (20)$$

TABLE 1. Thermodynamic and structure parameters for some solid elements concerned in this work, such as; bulk enthalpy H_{mb} (kJ/mol), bulk cohesive energy E_{mb} [kJ/mol], surface energy γ (J/m²), entropy S_{vib} (J/mole.K), mean bond length d_{mean} (nm), first surface layer height h (nm) [15, 23-25, 27, 34].

Substance	h (nm)	d_{mean} (nm)	H_{mb} (kJ/mol)	E_{mb} (kJ/mol)	S_{vib} (J/mole.K)	γ (J/m ²)
Ag	0.3197	0.289	113	284	9.16	7.205
Au	0.3188	0.2884	125	368	9.38	1.28
In	0.3682	0.3291	328	284	7.59	1.205
Sn	0.281	0.376	720	303	9.22	0.68

Results and Discussion

Fig. 1 illustrates a comparison between the predication of modified Eq. (2) (with and without the effect of lattice volume) with Eq. (13) and experimental $T_m(r)$ data for metallic Au nanoparticles. The result of modified Eq. (2) is in agreement with the experimental data. Moreover, the bulk melting temperature of Au is 1337.58 K [25]. As shown in Fig. 1, the results of the modified LVB model, as predicated by Eq. (2) in calculating the melting temperature of nanoparticles due to the effect of lattice volume, were in good agreement with the range of the experimental data.

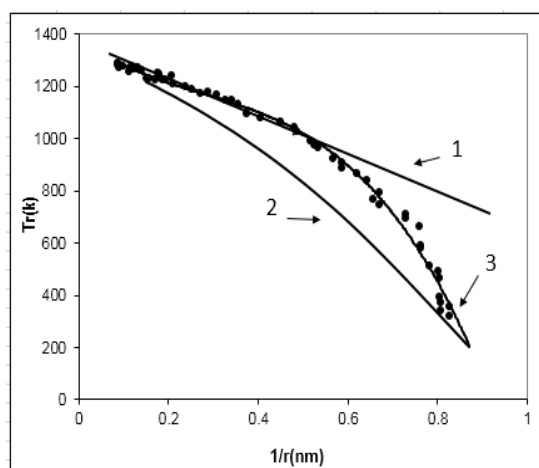


FIG. 1. $T_m(r)$ function of the Au nanoparticle size, where number (1) on the figure represents the SVA model predication of Eq. (13), whereas (2) and (3) represent the LVB model and its modified predication of Eq. (2), respectively and the solid spheres (●) represent the experimental data obtained from Ref. [36].

The SVA model in the range ($r < 10$ nm) gave higher results than the experimental results. The results of both models were different from the experimental data. Diwan and Kumar (2013) showed that the binding energy, cohesive energy and other thermodynamic properties, such as

entropy and enthalpy, approach their bulk value when the particle size is above 100 nm [17,35]. Figure 2 also shows that the cohesive energy of a nanoparticle approaches its bulk value when the nanoparticle size (r) is far beyond the atomic size ($r \gg d$).

Moreover, deviation occurred as the size of the nanocrystal was smaller than 3 nm due to the changes in the lattice structure of Au nanoparticles [2].

Fig. 2 illustrates a comparison between $E(r)$ represented by Eq. (10) and the predication of modified Eq. (10) with Eq. (18) and the experimental $E(r)$ results for metallic Ag nanoparticles. The best agreement was obtained between the modified (LVB) model (Eq. 10) and the experimental data as the particle volume decreased and approached $r = 2$ nm.

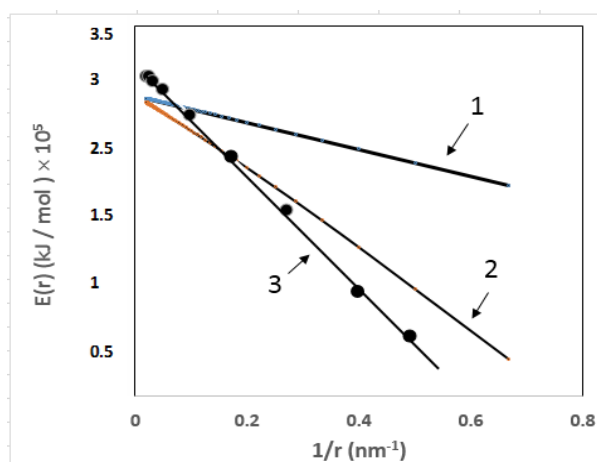


FIG. 2. $E(r)$ function of Ag nanoparticle size, where number (1) represents the SVA model predication of Eq. (18), (2) represents the LVB model predication of Eq. (10), (3) is the modified predication of Eq (10) and the solid spheres (●) represent the experimental data obtained from Ref. [36].

entropy and enthalpy, approach their bulk value when the particle size is above 100 nm [17,35]. Figure 2 also shows that the cohesive energy of a nanoparticle approaches its bulk value when the nanoparticle size (r) is far beyond the atomic size ($r \gg d$).

According to our study, a clear matching can be obtained between both models and the experimental data when the nanoparticle size is larger than 20 nm. The cohesive energy of a nanocrystal is governed by nearest neighbor interactions. This phenomenon leads to a linear dependence of this cohesive energy on the inverse size (reciprocal radius) of nanoparticles [20, 23, 36].

For metals, the assumption of the nearest neighbor is good. However, for nonmetallic and semiconductor nanocrystals, this assumption is no longer valid, because covalency and ionicity play major roles in bonding and determining the cohesive energy [27].

The cohesive energy of nanoparticles may increase or decrease with the crystal size, depending on the surface atom bonds of nanoparticles. If the surface atoms have large dangling bonds, then the cohesive energy of the nanoparticle decreases with decreasing the crystal size. This result implies a decrease in the strength of metallic bond (i.e., easily break). In this case, the strength of the metallic bond for nanoparticles becomes weaker than those of the bulk metals [18, 27].

In Figs. 3–5, we present a comparison between the *LVB* model prediction of Eq. (7) and the modified prediction of Eq. (7), as well as between the *SVA* model prediction of Eq. (17)

and the experimental results of $H_{mb}(r)$ for Ag, In and Sn nanoparticles obtained from References [29, 37]. The results of the modified *LVB* model were in good agreement with the experimental data for In, Sn and Ag nanoparticles. For Sn and In nanoparticles, the results of the *LVB* model approached the experimental data at a size larger than 10 nm.

The results of the *SVA* model of $H_{mb}(r)$ were higher than the experimental results for Ag and In nanoparticles, particularly at a size smaller than ($r < 15$ nm). For In and Sn nanoparticles, the *LVB* and *SVA* models were more consistent with each other at a size of ($r > 20$ nm).

Previously, a physical model was established and predicted that the decrease of size-dependent melting enthalpy, $H(r)$, is induced by the increase in *SVA* ratio and lower coordination number of surface atoms [26].

Melting enthalpy changes when nanoparticle size decreases. This trend is due to two reasons; firstly, the surface fraction of atoms in nanoparticles increases with decreasing size and secondly, surface atoms have a different bonding environment than the interior atoms within the material bulk. Moreover, the elastic properties of atoms at the surface differ from those of the bulk, because the phonon confinement affects elasticity and vibration behavior of nanoparticles [29, 31, 39, 40].

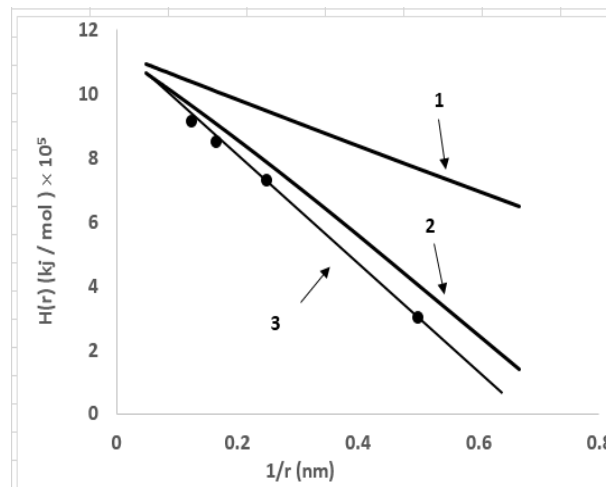


FIG. 3. $H(r)$ function of Ag nanoparticle size, where number (1) represents the *SVA* model prediction of Eq. (17), (2) represents the *LVB* model prediction of Eq. (7), (3) is the modified prediction of Eq. (7) and the solid spheres (\bullet) represent the experimental data obtained from the Ref [21].

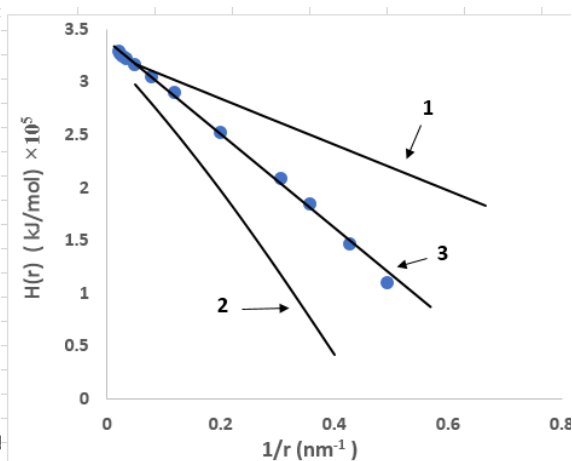


FIG. 4. $H(r)$ function of In nanoparticle size, where number (1) represents the *SVA* model prediction of Eq. (17), (2) represents the *LVB* model prediction of Eq. (7), (3) is the modified prediction of Eq. (7) and the solid spheres (\bullet) represent the experimental data obtained from Ref. [24].

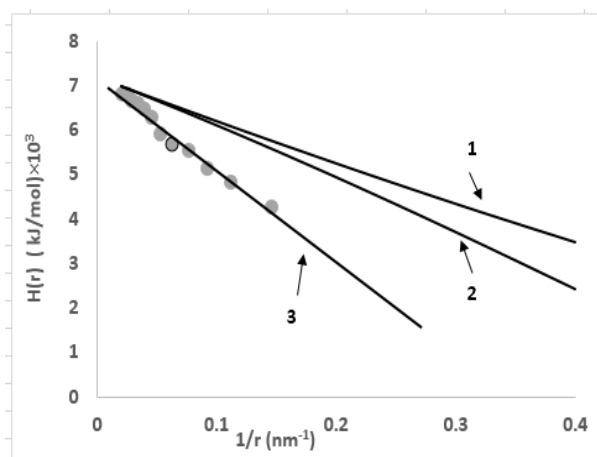


FIG. 5. $H(r)$ function of Sn nanoparticle size, where number (1) represents the *SVA* model predication of Eq. (17), (2) represents the *LVB* model predication of Eq. (7), (3) is the modified predication of Eq. (7) and the solid spheres (●) represent the experimental data obtained from Ref. [30].

The surface energies of Ag and Au nanoparticles as function of size are shown in Figs. (6) and (7). These figures show that the *LVB* model is better than the *SVA* model, because the surface energy of the *LVB* model approaches the experimental data, particularly for Au nanoparticles, where $r > 5\text{nm}$. However, for Ag nanoparticles, matching starts at sizes higher than 10 nm. These results are the reason for the modified *LVB* model. Furthermore, the results of the *SVA* model for Au and Ag nanoparticles were different from the experimental data at the size of ($r > 10\text{ nm}$).

Moreover, good agreement was observed between the modified *LVB* model and the experimental results at low dimensions in Ag and Au nanoparticle sizes near ($r = 3\text{nm}$).

The surface energy of a substance is related to the bonding strength between its atoms. We observed decreased surface energy with decreasing material size. This result was because the atomic radius increased with increasing coordination number [41, 11].

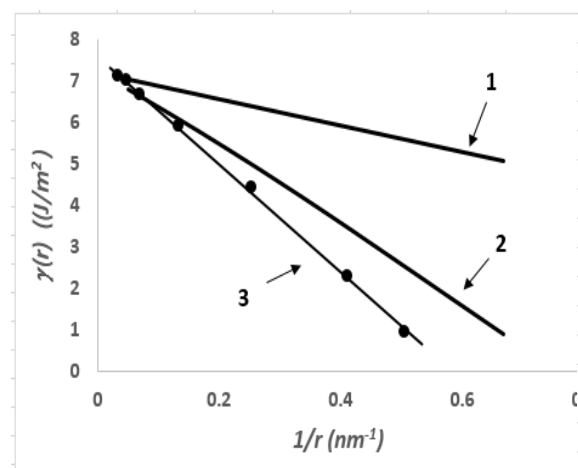


FIG. 6. $\gamma(r)$ function of Ag nanoparticle size, where number (1) represents the *SVA* model predication of Eq. (20), (2) represents the *LVB* model predication of Eq. (12), (3) is the modified predication of Eq. (12) and the solid spheres (●) represent the experimental data obtained from Ref. [15].

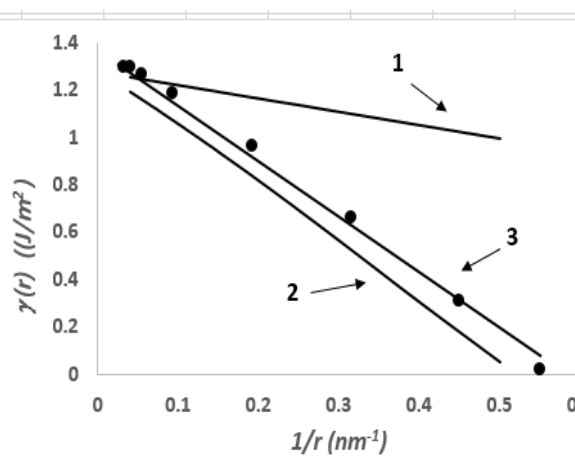


FIG. 7. $\gamma(r)$ function of Au nanoparticle size, where number (1) represents the *SVA* model predication of Eq. (20), (2) represents the *LVB* model predication of Eq. (11), (3) is the modified predication of Eq. (12) and the solid spheres (●) represent the experimental data obtained from Ref. [37].

Surface atoms take random configuration due to losses in crystalline order [43]. Moreover, surface effects can be neglected for most thermodynamic properties of bulk materials [42].

However, surface effects cannot be ignored for nanoscale metallic materials. Surface effects result from the difference between the surface metallic and interior atoms. Hence, surface atoms will be less stable than inner atoms due to the following: 1) lower coordination number of surface atoms than that of inner atoms and 2) atoms near the surface have fewer bonds than those far from the surface [25, 29].

Conclusion

In this work, *LVB* and *SVA* models were introduced to study the size-dependent enthalpy, cohesive energy, melting temperature and surface energy of Ag, Au, In and Sn nanoparticles. The relation to calculate thermodynamic parameters for bulk solids is used for nanoscale size successfully after modification. Results showed that the modification of the *LVB* model predication is superior than that of the *SVA* model when comparing the available experimental data, especially with the decrease in the sizes of free-standing nanoparticles. The *LVB* and *SVA* models approach the experimental data at large nanoparticle sizes.

References

- [1] Wang, M., Xue, Y., Cui, Z. and Zhao, M., *J. Mate. Sci.*, 52(2) (2017) 1039.
- [2] Omar, M.S., *J. Mate. Res. Bull.*, 47(11) (2012) 3518.
- [3] Marks, L.D. and Peng, L., *J. Phy. Cond. Matt.*, 28(5) (2016) 053001.
- [4] Li, Q., Yu, Y., Liu, Y., Liu, C. and Lin, L., *A Molecular Dynamics Study. Materials*, 10 (1) (2017) 38.
- [5] Spinozzi, F., Ceccone, G., Moretti, P., Campanella, G., Ferrero, C., Combet, S., Ojea- Jimenez, I. and Ghigna, P., *A Combined SAXS and SANS Study. Langmuir*, 33(9) (2017) 2248.
- [6] Piloyan, G.O., Bortnikov, N.S. and Boeva, N.M., *J. Mod. Phy.*, 4(07) (2013) 16.
- [7] Jiang, Q. and Yang, C.C., *Current Nanoscience*, 4 (2) (2008) 179.
- [8] Nanda, K.K., *Model. Pramana*, 72(4) (2009) 617.
- [9] Jiang, Q., Li, J.C. and Chi, B.Q., *Chem. Phy. Lett.*, 366 (5) (2002) 551.
- [10] Sun, C.Q., Wang, Y., Tay, B.K., Li, S., Huang, H. and Zhang, Y.B., *J. Phy. Chem.*, 106 (41) (2002) 10701.
- [11] Qi, W.H., Wang, M.P., Zhou, M., Shen, X.Q. and Zhang, X.F., *J. Phy. and Chem. Solids*, 67(4) (2006) 851.
- [12] Qi, W.H., Huang, B.Y., Wang, M.P., Li, Z. and Yu, Z.M., *J. Phy. Lett.*, 370 (5) (2007) 494.
- [13] Galanakis, I., Papanikolaou, N. and Dederichs, P.H., *Surface Science*, 511(1) (2002) 12.
- [14] Van Beurden, P. and Kramer, G.J., *Phy. Rev.*, 63(16) (2001) 165106.
- [15] Ouyang, G., Tan, X. and Yang, G., *J. Phy. Rev. B*, 74 (19) (2006) 195408.
- [16] Qi, W.H., Wang, M.P., Li, Z. and Hu, W.Y., *Sol. Stat. Phenomena*, 121 (2007) 1181.
- [17] Diwan, B.D. and Kumar, S.N., *Int. J. Mod. Phy.: Conference Series*, 22 (2013) 525.
- [18] Farrell, H.H., *J. Vac. Scie. and Tech.*, 26 (4) (2008) 1534.
- [19] Lu, H.M. and Jiang, Q., *J. Phy. Chem. B*, 108 (18) (2004) 5617.
- [20] Qi, W.H., *Physica B: Cond. Matt.*, 368 (1) (2005) 46.
- [21] Kumar, R., Sharma, G. and Kumar, M., *J. Thermodynamics*, 213 (2013) 4.
- [22] Omar, M.S., *Int. J. Thermophys.*, 37(11) (2016) 1.
- [23] Sun, C.Q., Bai, H.L., Li, S., Tay, B.K., Li, C., Chen, T.P. and Jiang, E.Y., *J. Phys. Chem.*, 108 (7) (2004) 2162.

- [24] Liang, L.H., Zhao, M. and Jiang, Q., *J. Mat. Sci. Lett.*, 21(23) (2002) 1843.
- [25] Omar, M.S., *J. Adva. Mate. Res.*, 626 (2013) 976.
- [26] Yang, C.C., Xiao, M.X., Li, W. and Jiang, Q., *J. Sol. Sta. Com.*, 139 (4) (2006) 148.
- [27] Farrell, H.H. and Van Siclen, C.D., *J. Vac. Sci. and Tech.*, 25(4) (2007) 1441.
- [28] Yang, C.C. and Li, S., *J. Phy. Chem.*, 112 (42) (2008) 16400.
- [29] Jiang, Q., Shi, H.X. and Zhao, M., *J. Chem. Phy.*, 111(5) (1999) 2176.
- [30] Zhao, M. and Jiang, Q., *Key Engineering Materials*, 444 (2010) 189.
- [31] Liang, L.H., Yang, G.W. and Li, B., *J. Phy. Chem. B*, 109 (33) (2005) 16081.
- [32] Liang, L.H. and Li, B., *Phy. Rev. B*, 73 (15) (2006) 153303.
- [33] Yanfeng, J. and Yamin, Z., *J. Semiconductors*, 31(1) (2010) 012002.
- [34] Singh, M. and Singh, M., *J. Phys.*, 84 (4) (2015) 609.
- [35] Shi, F.G., *J. Mat. Res.*, 9(5) (1994) 1307.
- [36] Vanithakumari, S.C. and Nanda, K.K., *J. Phys. Chem.*, 110 (2) (2006) 1033.
- [37] Jiang, Q. and Lu, H.M., *Surface Sci. Reports*, 63 (10) (2008) 427.
- [38] Buffat, Ph. and Borel, J.P., *Phys. Rev. A*, 6 (1976) 2287.
- [39] Zhang, Z., Lü, X.X. and Jiang, Q., *Phy. Cond. Mat.*, 270 (3) (1999) 249.
- [40] Karasevskii, A.I. and Lubashenko, V.V., arXiv preprint arXiv, (2009) 0902.
- [41] Holec, D., Dumitraschkewitz, P., Fischer, F.D. and Vollath, D., arXiv preprint arXiv, (2014) 1412.7195.
- [42] Ouyang, G., Zhu, W.G., Sun, C.Q., Zhu, Z.M. and Liao, S.Z., *J. Phy. Chem.*, 12 (7), (2010) 1543.
- [43] Regel, A.R. and Glazov, V.M., *J. Semiconductors*, 29 (1995) 405.

Compton Scattering of Twisted Light

Mazen Nairat^a and David Voelz^b

^a *Physics Department, Al-Balqa` Applied University, Salt, Jordan.*

^b *Electrical and Computer Engineering Department, New Mexico State University, USA.*

Received on: 24/2/2018;

Accepted on: 5/9/2018

Abstract: The variation of photonic orbital angular momentum in Compton scattering is analytically analyzed. We determine the scattering matrix of twisted light based on the fundamental conservation of orbital angular momenta. Numerical values for two different twisted light modes: Laguerre-Gaussian and Bessel-Gaussian, are generated and illustrated. Our analysis indicates that states of photonic orbital angular momentum are highly changeable at wide angle scattering but more consistent at small angle scattering.

Keywords: Compton scattering, Twisted light, Laguerre-Gaussian mode, Bessel-Gaussian mode.

Introduction

Twisted light carries the angular form of an electromagnetic momentum. It is separable and decomposes into an orbital momentum part as well as a spin momentum part. The orbital angular momentum associates with the helical structure of the wave front, while the spin angular part associates with the polarization state [1].

Twisted light carries a well-defined photonic orbital angular momentum (POAM). Its wave front characterizes a specific azimuthal phase according to the POAM state [2]. Both photonic spin angular momentum and POAM are orthonormal components of the total light angular momentum.

Compton scattering describes the change in linear momentum at elastic collisions between a photon and an electron. The well-known shift in a scatter wave number reports a certain change in the linear momentum as well as in the energy of scattering photons [3, 4]. However, a variation in POAM has never been mentioned.

Several studies have recently been conducted to describe changes in POAM in Compton scattering in ultra-relativistic considerations [5, 6]. A non-relativistic framework has been implemented in the density matrix theory to inform about the variation of POAM in Compton scattering [7].

Our study briefly analyzes a change of POAM of twisted light in Compton scattering by evaluating the associated scattering matrix in a semi-classical framework. It illustrates the possibility for POAM to vary through scattering at free electrons and emphasizes the conservation of total angular momentum *via* exchange of POAM between photons and massive electrons.

The next section determines a particular analytical expression of the scattering matrix of Compton scattering for a twisted light. The expression is valid for axi-symmetric light beam that carries a well-defined POAM. In the following section, two different beams are examined. Our numerical calculations are then analyzed and discussed. The conclusion is then presented at the end of this study.

Conservation of OAM in Compton Scattering

The schematic diagram of Compton scattering in Fig. 1 identifies the scattered photonic wave number (k') as well as POAM by primed parameters (l'), while the associated wave number and orbital angular momentum of the recoil electron are indicated by k_e and m_e , respectively. The scattering angle (θ) is defined as the angle between the incident beam and the scattering direction.

Our analysis is based on evaluating, semi-classically, the scattering matrix of Compton scattering to illustrate the fundamentals of an exchange of orbital angular momentum between the twisted light wave and a massive particle.

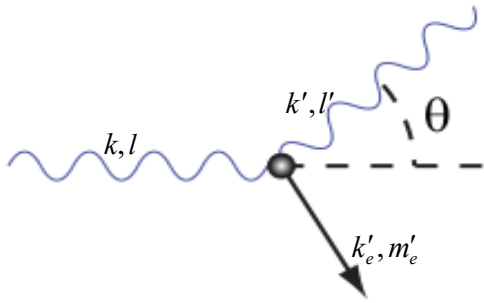


FIG.1. Schematic of Compton scattering with associated parameters.

$$S = \left\langle P_{m'}^*(\rho', z') e^{i(m'+l')\phi} R_{l'}^*(\rho', z') \left| e^{i(\vec{k}'-\vec{k})\cdot\vec{r}} \right| P_m(\rho, z) e^{-i(m+l)\phi} R_l(\rho, z) \right\rangle \quad (2)$$

Due to the azimuthal symmetry of the spatial wave profiles, we can separate the exponential of azimuthal parameters out as follows:

$$S = \left\langle P_{m'}^*(\rho', z') R_{l'}^*(\rho', z') \left| e^{i(\vec{k}'-\vec{k})\cdot\vec{r}} \right| P_m(\rho, z) R_l(\rho, z) \right\rangle \left\langle e^{i(\Delta m + \Delta l)\phi} \right\rangle \quad (3)$$

where $\Delta m = m' - m$ and $\Delta l = l' - l$. The last angle bracket in Eq. (3) is evaluated directly using the Dirac delta function:

$$\left\langle e^{i(\Delta m + \Delta l)\phi} \right\rangle = \delta(\Delta m + \Delta l) \quad (4)$$

Eq. (4) reads that a decrease in POAM must be equivalent to an increase of electronic one: $\Delta m = -\Delta l$. Consequently, the Compton scattering matrix is not terminated as long as the orbital angular momentum exchanges between the photon and the electron. It must be conserved through scattering.

The Compton scattering matrix is defined as [8]: $S = \left\langle f' \left| e^{i(\vec{k}'-\vec{k})\cdot\vec{r}} \right| f \right\rangle$, where f' , f represent the scattered and the initial state of the system, \vec{k} , \vec{k}' are the incident and scattered wave vectors and \vec{r} is a position vector. The cylindrical coordinates are used in such a way the optical path is considered along the z-axis.

Both, spatial electronic and photonic wave functions, Φ and Ψ , respectively, are considered. Their conjugates are indicated by superscript stars. The Compton scattering matrix can be presented as:

$$S = \left\langle \Phi^*(\vec{r}') \Psi^*(\vec{r}') \left| e^{i(\vec{k}'-\vec{k})\cdot\vec{r}} \right| \Phi(\vec{r}) \Psi(\vec{r}) \right\rangle \quad (1)$$

Normalized wave functions in cylindrical coordinates are used due to an azimuthal symmetry of twisted light. Generally, electronic and photonic wave functions could be expressed as $\Phi(\vec{r}) = P_m(\rho, z) e^{-im\phi}$ and $\Psi(\vec{r}) = R_l(\rho, z) e^{-il\phi}$, where m, l are parameters indicating the electronic and POAM state, respectively. Therefore, Eq. (1) is written explicitly as:

Evaluating Compton scattering matrix requires resolving the wave functions as well as the middle exponential term. The electronic radial wave function $P_m(\rho, z)$ is a separable function. It is generally given by:

$$P_m(\rho, z) = J_m(\kappa_e \rho) e^{ik_e z} \quad (5)$$

where J_m is Bessel function and κ_e and k_e are transverse and longitudinal electronic wavenumbers, respectively. On the other hand, the wave vector of collimated twisted light in general is composed of two components: orbital

and longitudinal [9]. It can be basically presented as:

$$\vec{k} = \kappa\hat{\phi} + k\hat{z}. \quad (6)$$

Hence, the middle term in the scattering matrix, the exponential term in Eq. (3), is simplified as follows:

$$\exp[(\vec{k}' - \vec{k}) \cdot \vec{r}] = \exp[(k' - k)z]. \quad (7)$$

Taking Eqs. (4, 5 and 7) together, we evaluate the scattering matrix as follows:

$$S = \langle J_{m'}^*(\kappa'_e \rho') R_{l'}^*(\rho', z') | J_m(\kappa_e \rho) R_l(\rho, z) \rangle \delta(\Delta k_e + \Delta k). \quad (8)$$

The Dirac delta term indicates that the longitudinal components of the wave vector, which represent the linear momentum, are also exchanged between the electron and the photon. An increase in the linear momentum of the electron is equivalent to a decrease in the linear momentum of the photon. It is definitely consistent with the well-known Compton formula [3]. Conservation of both linear and orbital angular momentum emphasizes the

conservation of total momentum for twisted photons in Compton scattering.

Our objective is to focus on the change of photonic orbital angular momentum in Compton scattering. It requires the evaluation of the scattering matrix regardless the initial OAM state. It is computed for a relative OAM exchange in the zero-order state of the “untwisted mode”; i.e.:

$$S = \langle J_{\Delta l}^*(\kappa' \rho) R_{\Delta l}^*(\rho, z') | J_0(\kappa \rho) R_0(\rho, z) \rangle. \quad (9)$$

The conditions of Eqs. (3) and (7) have been used. Indeed, it has been assumed that there is no change in the radial parameter (ρ) through scattering and on the other hand, axial parameter (z) depends only on the scattering angle (θ). Thus, the scattering matrix is evaluated at a certain axial distance.

Results and Discussion

The scattering matrix in Eq. (9) is computed for two particular twisted light beams: *Bessel-Gaussian* and *Laguerre-Gaussian (LG)*. The spatial wave function of LG is given by [10]:

$$R_l^{LG}(\rho, z) = \frac{C_p^l}{w(z)} \left[\frac{\sqrt{2}\rho}{w(z)} \right]^{|l|} \exp\left(-\frac{\rho^2}{w(z)^2}\right) L_p^{|l|}\left(\frac{2\rho^2}{w(z)^2}\right) \exp\left[\frac{-ik\rho^2 z}{2(z^2 + z_R^2)} + iG_q^{|l|}(z)\right] \exp(-il\phi) \quad (10)$$

where C_p^l is a normalization constant, p is a radial index, $w(z)$ is the beam width at distance z and given by $w(z) = w_o \sqrt{1 + (z/z_R)^2}$, z_R is the Rayleigh range defined as: $z_R = \pi w_o^2 / \lambda$, $L_p^{|l|}(\bullet)$ is the associated Legendre polynomial and $G_p^{|l|}(z) = -i(2p + |l| + 1) \tan^{-1}(z/z_R)$ is the Gouy phase [10]. It should be noted that the scattered axial parameter, z' , varies only through the scattering angle (θ). Our computations are based on fixed z values.

Eqs. (9) and (10) are used to evaluate the scattering matrix of an x-ray of 1 nm wavelength and 1 μm waist width through a wide scattering in the range $-\pi/2 < \theta < \pi/2$. It is assumed that there is no change in Gouy phase through scattering.

The computed elements that associate for a certain change (Δl) in photonic OAM are determined and plotted. Fig. 2 illustrates Compton scattering matrix *versus* scattering angle for several changes in POAM. The curves are generated by computing the normalized scattering matrix in a wide angle range for four successive state changes in POAM.

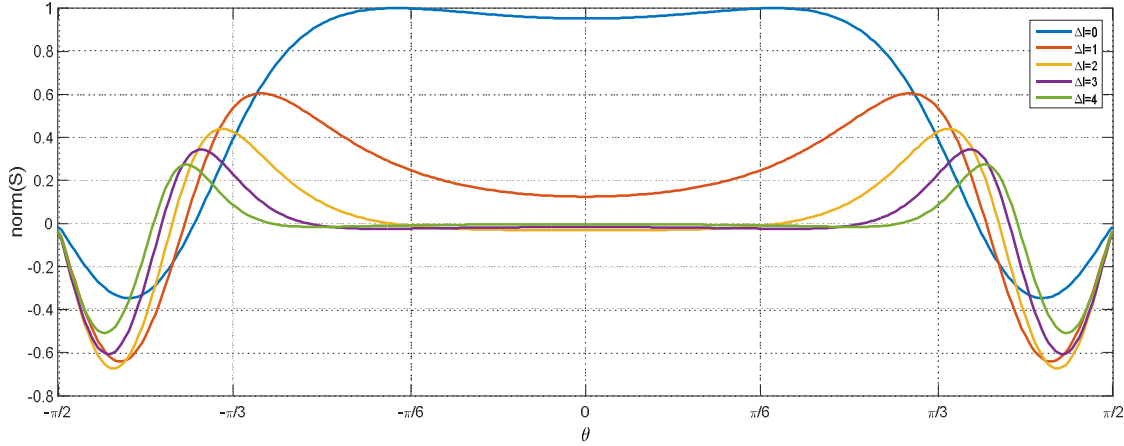


FIG. 2. Normalized Compton matrices *versus* scattering angle for LG beam at certain changes in POAM.

The normalized scattering elements shown in Fig. 2 are very small for narrow range scattering. The normalized scattering provides the probability of exchanging POAM, which is minimum at small scattering angle. However, a change by just one order state could happen with low possibility as the curve of $\Delta l=1$ shows.

High possibilities of changing POAM states through scattering are represented by the peaks shown in Fig. 2. Scattering matrix elements are relatively of small values for higher change in POAM. It could be interpreted as a low

possibility for a big change in POAM at Compton scattering.

Negative-value elements in Fig. 2 indicate flipping up of OAM states. They inform that scattering in wide angles causes flipping up of the azimuthal phase. Consequently, POAM states are twisted “oppositely” at wide angles of Compton-scattering. However, scattering matrices are terminated at right angle scattering due to the minimized differential cross-section of Compton scattering [11].

Scattering matrix is also computed for large changes in photonic OAM states and is plotted in Fig. 3.

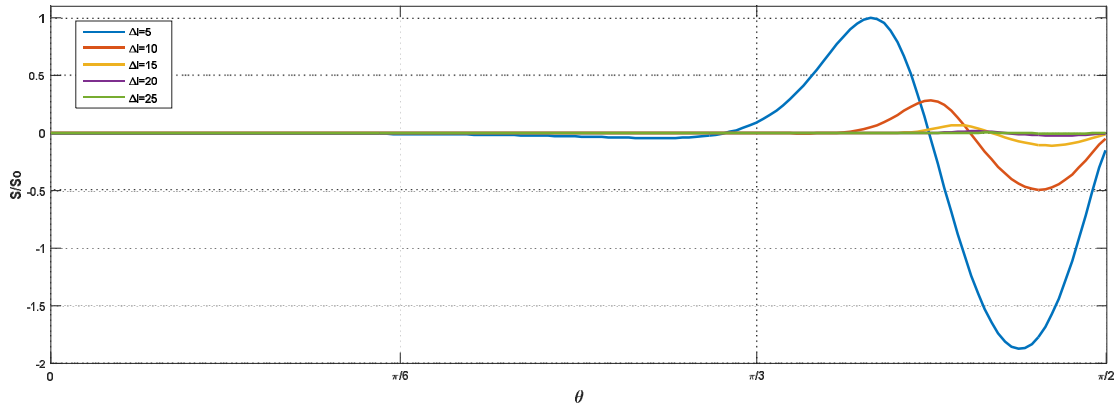


FIG. 3. Normalized Compton matrices *versus* scattering angle for LG beam at big changes in photonic OAM.

Fig. 3 confirms the low possibilities of scattering twisted photons with high changes in their POAM. Indeed, it indicates that Compton scattering at wide angles is more likely to occur with oppositely twisted orientation. Dominant negative peaks at Fig. 3 represent a tendency of

large changes in photonic OAM to be in opposite orientation.

The other twisted light beam that has been investigated is the Bessel-Gaussian beam, which has a spatial wave function given by [12]:

$$R_l^{GB}(\rho, z) = A \frac{w_o}{w(z)} \exp \left[i \left(k - \frac{\kappa^2}{2k} \right) z - i \phi(z) \right] J_l \left[\frac{\kappa \rho}{(1 + iz/z_R)} \right] \exp \left[\left(\frac{-1}{w(z)^2} + \frac{ik}{2R(z)} \right) \left(\rho^2 + \frac{\kappa^2}{k^2} z^2 \right) \right] \quad (11)$$

where A is the normalization constant, $\phi(z) = \tan^{-1}(z/z_R)$ is the associated Gouy phase, and $R(z) = z\sqrt{1 + (z_R/z)^2}$ is the radius of curvature.

Eq. (11) has been implanted in Eq. (9) to compute the corresponding scattering matrix for

the same parameters: a 1nm wavelength of an x-ray source, a 1 μ m beam waist and a non-varying Gouy phase.

The associated scattering matrix is evaluated for first-order changes in orbital angular momentum as shown in Fig. 4.

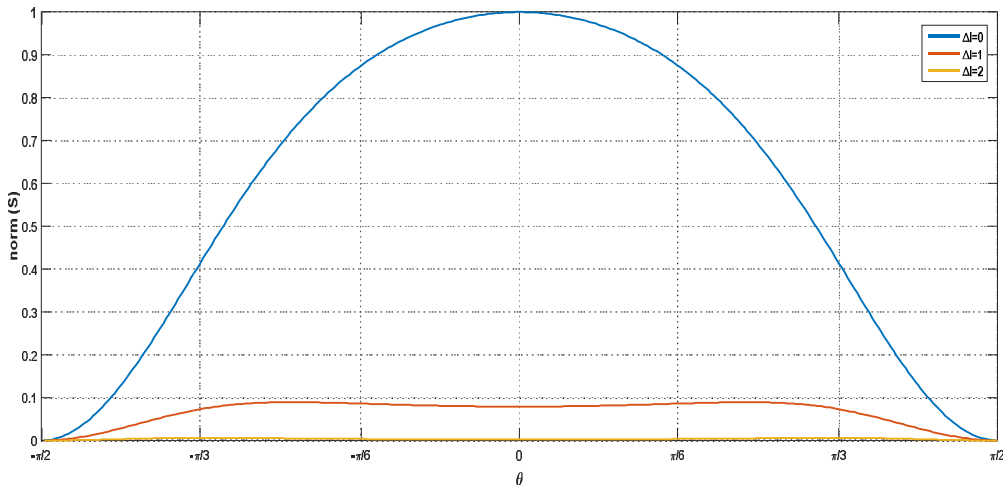


FIG. 4. Normalized Compton matrices *versus* scattering angle for BG beam at few changes in photonic OAM.

Scattering matrices of Bessel-Gauss beam which are illustrated in Fig. 4 change very slowly. Relatively high value peaks around a scattering angle of $\pi/3$ compared with small values at small scattering angles $|\theta| \leq \pi/6$. Similar to Laguerre-Gaussian mode, photonic

OAM of Bessel-Gauss beam is likely to be invariant at small angle scattering. They just tend to vary in wide scattering. However, extreme minimum scattering elements are at right-angle scattering, where the classical cross-section is minimum.

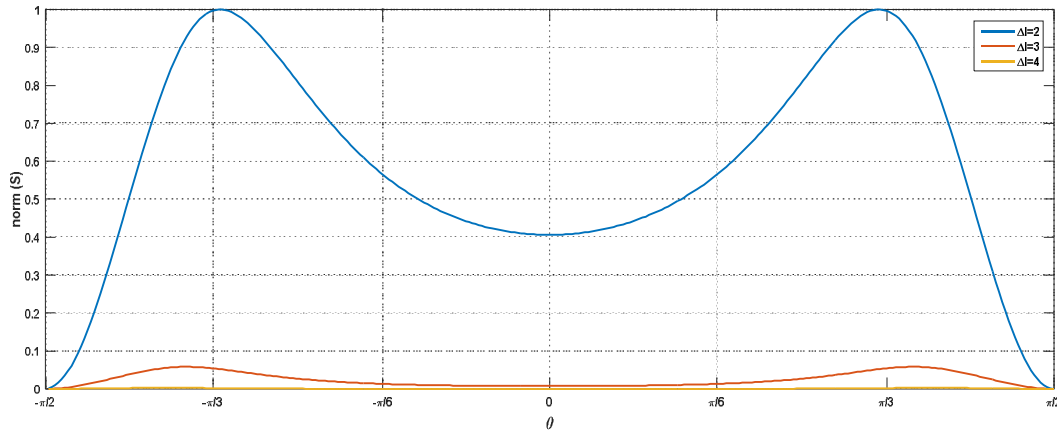


FIG. 5. Normalized Compton matrices *versus* scattering angle for BG beam at certain changes in POAM.

The scattering matrix is also computed for higher-order changes in POAM of Bessel-Gaussian mode as illustrated in Fig. 5. The order is changed by varying the associated azimuthal parameter to 2, 3 and 4, respectively.

Fig. 5 emphasizes the high possibility to exchange OAM at wide scattering compared with small angle scattering. POAM values are more consistent in Compton scattering by small angles, whereas extreme lowest values occur at right-angle scattering.

Conclusion

This study analyzes the conservation of POAM during Compton scattering. We evaluated the scattering matrix for twisted light

that is scattered by free electrons. Our analysis indicates that the POAM of the twisted light can be changed through Compton scattering. Specific numerical values are determined by Compton scattering of Laguerre-Gaussian and Bessel-Gaussian light beams. It has been reported that POAM states are invariant at forward scattering as well as small-angle scattering, but they mainly vary in wide-angle scattering.

Acknowledgments

The authors thank Roman Höllwieser, the affiliate assistant professor at New Mexico State University, for checking their calculations as well as their results.

References

- [1] Andrews, D. and Babiker, M., “The angular momentum of light”, (Cambridge University, 2013).
- [2] Allen, L., Beijersbergen, M.W., Spreeuw, R.J.C. and Woerdman, J.P., *Phys. Rev. A*, 45 (1992) 8185.
- [3] Compton, A.H., *Phys. Rev.*, 21(5) (1923) 483.
- [4] Nairat, M., Goedecke, G. and Voelz, D., *Optics*, 6 (1) (2017) 1.
- [5] Ivanov, I.P. and Serbo, V.G., *Phys. Rev. A*, 84 (2011) 033804.
- [6] Jentschura, U.D. and Serbo, V.G., *Phys. Rev. Lett.*, 106 (2011) 013001.
- [7] Stock, S., Surzhykov, A., Fritzsche, S. and Seipt, D., *Phys. Rev. A*, 92 (2015) 013401.
- [8] Davis, B.S., Kaplan, L. and McGuire, J.H., *J. Opt.*, 15(3) (2013) 109501.
- [9] Padgett, M. and Allen, L., *Cont. Phys.*, 41(5) (2000) 275.
- [10] Allen, L. and Babiker, M., *Phys. Rev. A*, 53 (1996) R2937.
- [11] Klein, O. and Nishina, Y., *Z. Physik*, 52 (1929) 853.
- [12] Gori, F., Guattari, G. and Padovani, C., *Opt. Commun.*, 64 (6) (1987) 491.

Neon Soft X-Ray Yield Optimization from NX2 Dense Plasma Focus Device

Walid Sahyouni^{a,b} and Alaa Nassif^a

^a Department of Physics, Faculty of Science, Al-Baath University, Homs, Syria.

^b Designated Delegate of Al-Baath University to the Asian- African Association for Plasma Training (AAAPT), Homs, Syria .

Received on: 27/2/2018;

Accepted on: 19/4/2018

Abstract: The aim of this research is to study soft x-ray emission from NX2 plasma focus device with neon filling gas using the Lee model code and find the maximum value of soft x-ray yield by using the standard parameters of the device and then find the optimum combination of pressure and anode dimensions that gives the maximum value of soft x-ray yield. Many numerical experiments were carried out and we obtained the maximum value of soft x-ray yield (Y_{sxr}) of (22.6 J) at a pressure of (2.9 Torr) by using the standard parameters of NX2 device. We found the optimum combination of pressure, anode length and anode radius (3 Torr, 2.1 cm and 2 cm), respectively, by reducing the anode length and increasing the anode radius. The soft x-ray yield increases to (26.01 J) with a corresponding efficiency of about 1.53%.

Keywords: Lee model code, NX2 device, Soft x-ray yield.

Introduction

Hot and dense plasma can be generated by compression and imploding cylindrical magnetized plasma, to form a hot, dense plasma pinch. This pinch is considered an important source for x-rays (soft and hard) and energetic beam ions. The plasma focus devices are the simplest in construction and provide the highest x-ray emissions compared to other devices of equivalent energy [1, 2]. These x-ray sources are used for various applications, such as lithography [3] and imaging [4].

The importance of this research lies in computing soft x-ray yield Y_{sxr} as a function of filling gas pressure (neon) and searching for the possibility of increasing the soft x-ray yield through modification of the anode's dimensions without the need to change the energy of capacitor bank by carrying out numerical experiments using the Lee model code, version (RADPFV5.15de.c1).

The Radiative Lee Model

The Lee model couples the electrical circuit with plasma focus dynamics, thermodynamics and radiation, enabling a realistic simulation of all gross focus properties. The basic model is described in [6]. The code has been used extensively in several machines, including UNU/ICTP PFF, NX2 and NX1. The 5 phases of Lee model are as follows:

- 1) Axial phase.
- 2) Radial inward shock phase.
- 3) Radial reflected shock (RS) phase.
- 4) Slow compression (quiescent) or pinch phase.
- 5) Expanded column phase.

A detailed description of these phases is found in [7].

In the code, neon line radiation Q_L is calculated as follows [8]:

$$\left. \begin{aligned} \frac{dQ_L}{dt} = \\ - 4.6 \times 10^{-31} n_i^2 Z Z_n^4 (\pi r_p^2) z_f / T \end{aligned} \right\}$$

where for the temperatures of interest in our experiments, we take $Y_{\text{sxr}} = Q_L$.

Hence, the SXR energy generated within the plasma pinch depends on the following properties: number density n_i , effective charge number Z , pinch radius r_p , pinch length z_f , temperature T and pinch duration. In our code, Q_L is obtained by integrating over the pinch duration. This generated energy is then reduced by the plasma self-absorption which depends primarily on density and temperature. The reduced quantity of energy is then emitted as the SXR yield.

Method

Numerical Experiments on Standard NX2 Device with Neon Filling Gas

The following bank, tube, operation and model parameters are used [9]:

- 1) Bank: static inductance $L_0 = 15$ nH, $C_0 = 28$ μ F and stray resistance $r_0 = 2.2$ m Ω .
- 2) Tube: cathode radius $b = 4.1$ cm, anode radius $a = 1.9$ cm and anode length $z_0 = 5$ cm.
- 3) Operation: voltage $V_0 = 11$ kV, pressure $P_0 = 3$ torr Neon, MW=20, A=10, At-Mol=1.
- 4) Model: $f_m=0.1$, $f_c=0.7$, $f_{mr}=0.12$, $f_{cr}=0.68$.

Optimizing Soft X-ray Yield (Y_{sxr}) by Changing Anode Geometry

Numerical experiments using the Lee model code were carried out to determine the optimum configuration of anode that gives the highest value of soft x-ray yield (Y_{sxr}). The bank capacitor parameters were retained at ($L_0=15$ nH, $C_0= 28$ μ F, RESF = 0.1) and the voltage was retained at ($V_0 = 11$ kV). The model parameters were also retained at ($f_m = 0.1$, $f_c = 0.7$, $f_{mr} = 0.12$, $f_{cr} = 0.68$). The value of the ratio of the outer to inner electrode constant ($c=b/a$) is kept constant at (2.2). The anode dimensions (length z_0 and radius a) and the pressure (P_0) were parametrically varied and results were tabulated in Table 2.

The following procedure was used [10]:

At each P_0 , the anode length z_0 was fixed at a certain value.

Then, the anode radius (a) was smoothly varied, till the maximum soft x-ray yield (Y_{sxr}) was obtained for this certain value of z_0 .

After that, we chose another value of z_0 , by varying the value of (a) looking for the maximum of Y_{sxr} , until we found the optimum combination of z_0 and (a) for the best soft x-ray yield at the fixed P_0 .

Then, we changed P_0 and repeated the above procedure to find the optimum combination of z_0 and (a) corresponding to this new value of P_0 . We continued until we obtained the optimum combination of P_0 , z_0 and (a) for the maximum soft x-ray yield (Y_{sxr}). There is an optimum temperature for optimum neon soft x-ray yield (2.3×10^6 K) [11].

Results and Discussion

From Table 1, we note that:

The pressure varies from 5 to 0.5 Torr. The soft x-ray yield (Y_{sxr}) increases with decreasing pressure until it reaches the maximum value (22.6 J) at ($P_0=2.9$ Torr) at a corresponding efficiency of about 1.329%, after which it decreases with lower pressure (see Fig. 1). This is due to the fact that as pressure increases, the speed (end axial speed v_a , inward shock speed v_s , radial piston speed v_p) decreases. The decrease in speed leads to lowering the plasma temperatures below the level needed for soft x-ray production (see Fig. 2). The pinch current (I_{pinch}) increases with decreasing pressure. This is due to the shifting of pinch time towards the time of peak current. On the contrary, the total discharge current (I_{peak}) decreases with decreasing pressure because of increasing the dynamic resistance due to increasing current sheath speed as the pressure decreases (see Fig. 3). The ion density in the middle of the pinch (n_{pinch}) increases as pressure decreases, peaking around 3 Torr and then dropping at lower pressures (see Fig. 4).

TABLE 1. Computed soft x-ray yield (Y_{srx}) and pinch properties *versus* P_0 for standard parameters of NX2 at: $L_0 = 15$ nH, $C_0 = 28$ μ F, $r_0 = 2.2$ m Ω , $V_0 = 11$ kV, ratio of stray resistance/bank surge impedance RESF = 0.1, $c = b/a = 2.2$, $f_m = 0.1$, $f_c = 0.7$, $f_{mr} = 0.12$, $f_{cr} = 0.68$, neon gas.

P (Torr)	I_{peak} (kA)	I_{pinch} (kA)	$T_{pinch} \times 10^6$ (K ⁰)	V_a (cm/ μ s)	V_s (cm/ μ s)	V_p (cm/ μ s)
5	The code unable to run					
4.5	The code unable to run					
4	378	118	0.88	4.9	14.9	11.6
3.5	374	132	1.24	5.3	17.3	12.9
3	370	143	1.72	5.7	19.9	14.2
2.9	369	145	1.83	5.8	20.5	14.5
2.8	368	147	1.95	5.9	21.1	14.8
2.7	367	149	2.07	6	21.8	15
2.5	365	154	2.37	6.2	23.4	15.6
2	359	163	2.78	6.8	25.3	16.8
1.5	350	168	4.6	7.6	27.6	18.9
1	337	169	6.71	8.8	32	22.8
0.5	310	160	11.21	11.1	40.8	29

Table 1 (Continued)

P (Torr)	SF	a_{min} (cm)	z_{max} (cm)	Pinch duration (ns)	$n_i (\times 10^{23})$ (m ⁻³)	Y_{srx} (J)	Efficiency %
5	The code unable to run						
4.5	The code unable to run						
4	99	0.21	2.7	42.5	4.9	3.66	0.215
3.5	105	0.20	2.7	35.7	4.6	10.5	0.617
3	113	0.16	2.8	30.9	5.8	21.9	1.288
2.9	114	0.16	2.8	30.2	5.7	22.6	1.329
2.8	116	0.16	2.8	29.9	5.4	22.1	1.3
2.7	118	0.17	2.8	29	4.7	19.4	1.141
2.5	122	0.19	2.8	26.8	3.4	12.3	0.723
2	134	0.24	2.7	23	1.8	3.89	0.228
1.5	151	0.25	2.8	21.7	1.2	1.48	0.087
1	178	0.25	2.8	18.7	0.8	0.42	0.024
0.5	231	0.25	2.8	15.1	0.4	0.05	0.003

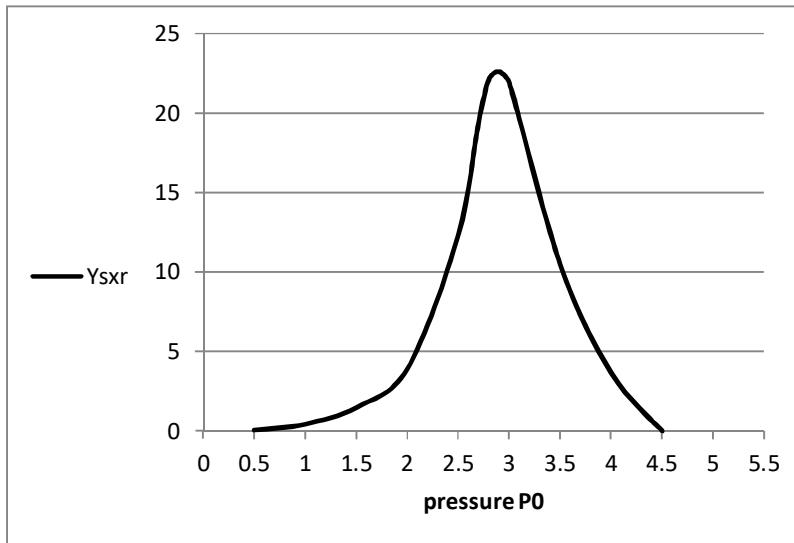


FIG. 1. Soft x-ray yield as a function of pressure.

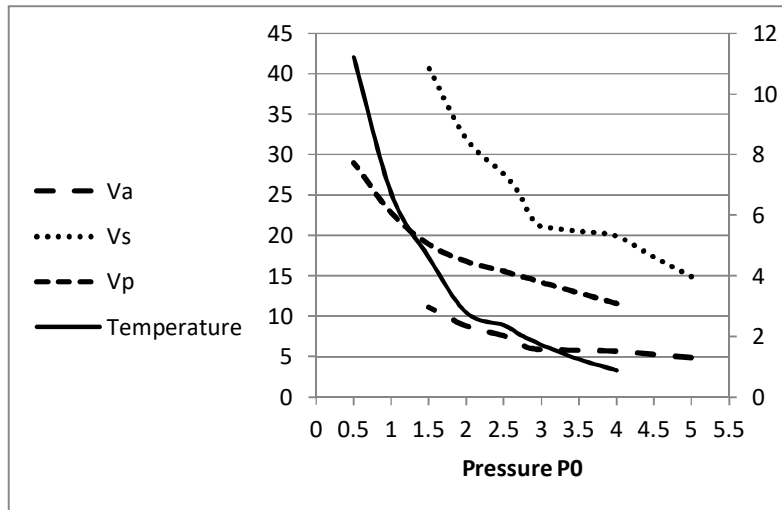


FIG. 2. Speeds and plasma temperature as functions of pressure.

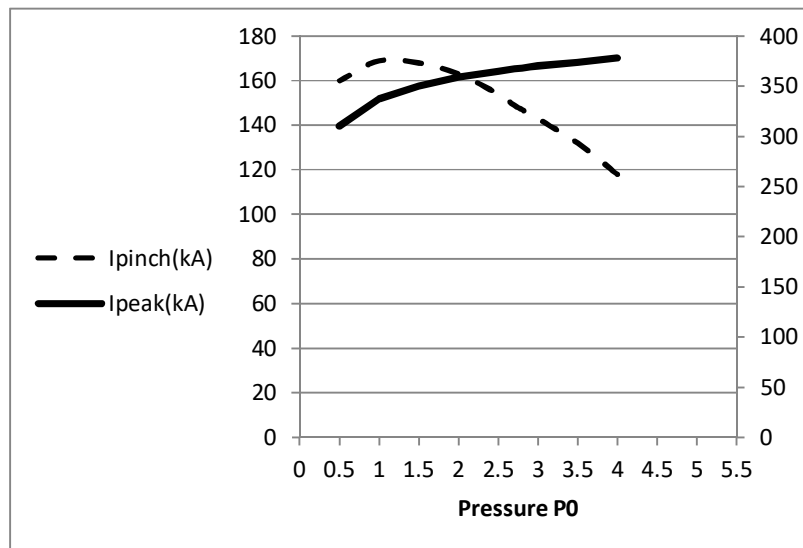


FIG. 3. Variation of I_{pinch} and I_{peak} versus pressure.

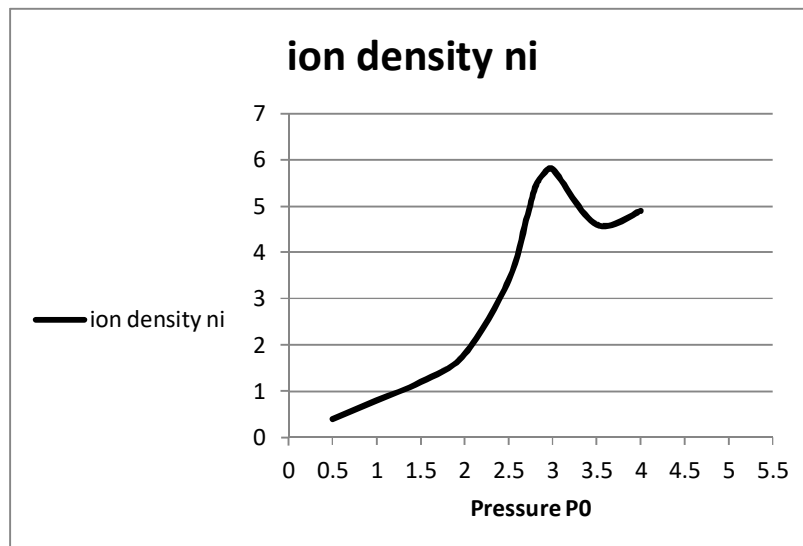


FIG. 4. Variation of ion density versus pressure.

Table 2 shows that as P_0 increases, anode length z_0 increases and inner radius 'a' decreases with each increase in P_0 , while the soft x-ray yield slightly increases with increasing P_0 until it reaches a maximum value of 26.01 J at $P_0 = 3$ Torr and the corresponding efficiency is about 1.53%, then Y_{srx} decreases with further pressure increase.

Fig. 5 shows x-ray yield as a function of P_0 , with the plasma focus operated at the optimum combination of z_0 and (a) corresponding to each P_0 .

Fig. 6 shows that both total current (I_{peak}) and pinch current (I_{pinch}) slightly increase with increasing pressure (P_0).

From our numerical experiments for, NX2 with $L_0=15$ nH, $C_0=28$ μF , $r_0 = 2.2$ m Ω , $V_0 = 11$ kV, we find the optimum combination of P_0 , z_0 and a for neon Y_{srx} as 3 Torr, 2.1 cm and 2 cm, respectively, with the outer radius $b = 4.4$ cm. This combination gives $Y_{\text{srx}} = 26.01$ J. We notice that the optimum soft x-ray yield from NX2 becomes higher (about 3.4 J).

TABLE 2. X-ray yield optimization from NX2 for each value of P_0 varying z_0 and (a) for filling neon gas at: $L_0 = 15$ nH, $C_0 = 28$ μF , $r_0 = 2.2$ m Ω , $V_0 = 11$ kV, ratio of stray resistance/bank surge impedance $\text{RESF} = 0.1$, $c = b/a = 2.2$, $f_m = 0.1$, $f_c = 0.7$, $f_{\text{mr}} = 0.12$, $f_{\text{cr}} = 0.68$.

P (Torr)	z_0 (cm)	a (cm)	b (cm)	I_{peak} (kA)	I_{pinch} (kA)	v_a (cm/ μs)	v_s (cm/ μs)	v_p (cm/ μs)	Y_{srx} (J)	Efficiency %
0.5	1.1	3.78	8.32	300	135	4.5	22.2	15.2	9.11	0.535
1	1.2	2.92	6.42	311	147	4.5	22.2	15.1	13.4	0.788
1.5	1.4	2.54	5.59	327	157	4.6	22.2	15.1	17.4	1.023
2	1.5	2.29	5.04	335	163	4.6	22.3	15.1	21.3	1.252
2.5	1.7	2.13	4.68	347	169	4.6	22.3	15.1	24.2	1.423
3	2.1	2	4.40	362	175	4.9	22.5	15.2	26.01	1.530
3.5	3	1.85	4.10	372	176	5.2	22.9	15.3	23.6	1.388
4	3.1	1.74	3.83	373	178	5.2	23.2	15.4	22.2	1.305

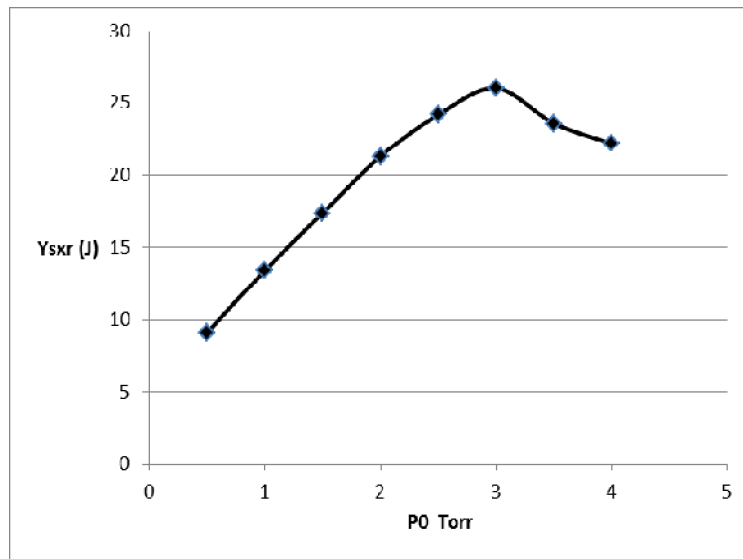


FIG. 5. Soft x-ray yield as a function of pressure, anode length and inner radius.

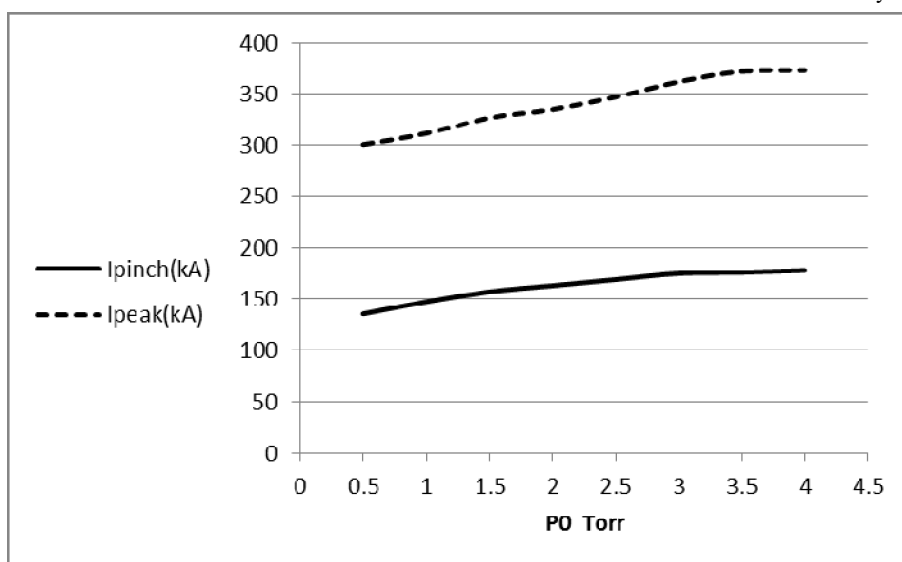


FIG. 6. Effect on total current (I_{peak}) and pinch current (I_{pinch}) as P_0 is increased from 0.5 to 4 Torr.

Conclusion

The Lee model code was applied to calculate the soft x-ray yield from NX2 plasma focus device by using standard parameters. We obtained the maximum value of Y_{srx} as 22.6 J at a pressure of 2.9 Torr. We also used the Lee model code to run numerical experiments on NX2 device with neon gas for optimizing soft

x-ray yield by reducing the anode length and increasing the radius of the anode. The neon soft x-ray yield optimum combination of NX2 was found to be at (pressure $P_0=3$ Torr, anode length $z_0=2.1$ cm and anode radius $a=2$ cm). The optimum soft x-ray yield was ($Y_{srx}=26.01$ J).

References

- [1] Zakaulah, M. et al., Appl. Phys. Lett., 78 (2001) 877.
- [2] Lee, S. et al., IEEE Trans. Plasma Sci., 26 (1998) 1119.
- [3] Lee, S. et al., ICPP & 25th EPS Conference (1998).
- [4] Rawat, R. et al., Journal of Fusion Energy, 23 (1) (2004) 49.
- [5] Lee, S., Radiative Dense Plasma Focus Computation Package: RADPF. <http://www.intimal.edu.my/school/fas/UFLF/File1RADPF.htm>. <http://www.plasmafocus.net/IPFS/modelpackage/File1RADPF.htm>.
- [6] Lee, S., "Plasma Focus Model Yielding Trajectory and Structure". In: Radiations in Plasmas, V. II, Ed. McNamara, B., (World Scientific, Singapore, 1984), pp. 978–987.
- [7] Lee, S. and Saw, S.H., Plasma Focus Numerical Experiments (NEWPF2016), Module 4, p. 24.
- [8] Lee, S. et al., Plasma Phys. Control. Fusion, 51 (2009) 105013.
- [9] Lee, S. and Saw, S.H., Plasma Focus Numerical Experiments (NEWPF2016), Module 9, p. 72.
- [10] Akel, M. et al., J. Fusion Energy, 29 (2010) 223.
- [11] Akel, M. et al., IEEE Transactions on Plasma Science, (2012).

Natural Radioactivity and Associated Radiation Hazards in Local Portland and Pozzolanic Cements Used in Jordan

Mefleh S. Hamideen

Department of Physics and Basic Sciences, Faculty of Engineering Technology, Al-Balqa Applied University, Amman, Jordan.

Received on: 8/5/2018;

Accepted on: 9/9/2018

Abstract: Activity concentration of the natural gamma-emitting radionuclides (^{40}K , ^{226}Ra and ^{232}Th) in at least forty samples of local Portland and Pozzolanic cement types is measured. The measurements were performed using gamma spectrometric techniques. The range of the mean specific activity (minimum and maximum values) due to all the three radionuclides is found. Radiological hazards of the different samples are estimated using five approaches; the representative level index, the external hazard index, the internal hazard index, the radium equivalent index and the absorbed dose rate. Some of the measured radiological hazard parameters are compared to similar parameters in different countries. The activity concentration of ^{226}Ra for all types of cements varies from 29.1 ± 2.01 to 79.2 ± 3.90 Bq.kg^{-1} . The activity concentration of ^{232}Th for all types of cements varies from 5.8 ± 1.1 to 26.4 ± 1.9 Bq.kg^{-1} . The activity concentration of ^{40}K for all types of cements varies from 231.9 ± 9.8 to 298.0 ± 10.7 Bq.kg^{-1} . The radium equivalent activity concentration, Ra_{eq} , of the total activity of each cement type is obtained. The highest value of Ra_{eq} was seen in white cement (125.49 Bq.kg^{-1}) and the lowest in Portland Pozzolanic cement (5%) with an average value of (78.08 Bq.kg^{-1}). Based on the assessment of potential radiological hazards as inferred from the calculations of Ra_{eq} , representative level index and the dose rate, the investigated cement samples fall within the category of accepted building materials and are safe to use for the construction of inhabited buildings.

Keywords: Radiological hazards, Portland cement, Pozzolanic cement.

Introduction and Objectives

The global demand for cement as a building material is considerable. Cement is an important construction material of houses and buildings built in urban areas in Jordan. Portland cement is the most common type of cement used in construction applications, but it is an expensive binder due to the high cost of production associated with the high energy requirements of the manufacturing process itself [1]. Other cheap inorganic materials with cementitious properties, such as natural pozzolans, e.g. volcanic tuff [2, 3] and clay [4], as well as waste products from industrial plants, e.g. slag [5], fly ash [6, 7] and silica fume [8], can be used as partial replacements for Portland cement; i.e., blended

cements [9]. In addition, to reduce the cost of binder, there are potential technological benefits from the use of pozzolanic materials as those blended with Portland cement in concrete applications. These include increased workability, decreased permeability [10], increased resistance to sulphate attack [11], improved resistance to thermal cracking and increased ultimate strength and durability of concrete [12-14].

The first objective of the present work is to measure the naturally occurring radioactive elements in the cement used as a building material in Jordan, since workers are exposed to radiation for a long time, especially in mines and

at manufacturing sites, in addition the exposure of people, who spend about 80% of their time inside offices and homes [13-15], resulting in exposure to cement or its raw materials as a necessary reality.

The content, of ^{226}Ra , ^{232}Th and ^{40}K in all types of cement can vary considerably, depending on their geological source and geochemical characteristics. The knowledge of radioactivity in these materials is important to estimate the radiological health impact on humans [16]. The radiological effect from natural radioactivity is due to radiation exposure of humans to gamma radiation and irradiation of lungs from inhalation of radon and its progenies. Thus, it is necessary to evaluate the dose limit of public exposure [17]. The external radiation exposure is caused by gamma radiation originating from members of the uranium and thorium decay chains and from potassium ^{40}K . However, the internal radiation exposure, mainly affecting the respiratory tract, is due to the short-lived radon and its daughters' products, which are emitted from construction materials into room air. The second objective of the present work is to calculate the radiological parameters, such as: the representative level index, the external hazard index, the internal hazard index, the radium equivalent concentration, Ra_{eq} and the absorbed dose rate, which are related to the external gamma-dose rate, and their effects on human health. The results of concentration levels and radiation equivalent activities are compared with similar studies carried out in other countries.

Materials and Methods

Preparation of Samples

Twenty five samples of all cement types produced by Cement Jordanian Factory (Portland cement, Portland Pozzolanic cement (5%), Portland Pozzolanic cement (25%), White cement and Sulphate Resistant Cement (S.R.C.)) were collected for this study [18, 19]. The percentage values in parentheses above indicate the percent of Pozzolana in cement. For comparison with products from other factories, 8 samples were taken from the ordinary Portland cement from (Arabia Company, Ashamaliya Company and Al-rajhi Company), 4 samples were taken of Portland Pozzolanic cement (25%) from (Arabia Company and Al-rajhi Company) and 4 samples were taken of (S.R.C.) from

(Arabia Company, Ashamaliya Company and Al-rajhi Company).

Each sample, 1kg in weight, was dried in an oven at about 110 °C to ensure that moisture is completely removed. The samples were crushed, homogenized and sieved through a 200 mesh, which is the optimum size to be enriched in heavy minerals. Weighed samples were placed in a polyethylene beaker of 350-cm³ volume. The beakers were completely sealed for 4 weeks to reach secular equilibrium, where the rate of decay of the radon daughters becomes equal to that of the parent. This step is necessary to ensure that radon gas is confined within the volume and that the daughters will also remain in the sample.

Instrumentation and Calibration

Measurements were performed using a High Purity Germanium (HPGe) detector supplied by EG&G Ortec. The detector is an n-type gamma-X-ray (GMX) detector, operated at 3500 V, with a useful energy range from 3 keV to 10 MeV, a standard energy resolution of 2.02 keV and a relative efficiency of 56.9% at 1.33 MeV of ^{60}Co . The absolute efficiency calibration of the detector was performed using the IAEA standard "soil-6" source within a Petri-dish, 90 mm in diameter and 10 mm thick. Its spectrum was collected for 12 h. Areas under the energy peaks of interest were used for drawing the peak efficiency curve between log of efficiency *versus* log of peak energy. A polynomial was fitted to the curve and the result was stored for further use. Under the assumption that secular equilibrium was reached between ^{226}Ra and its short-lived daughters, gamma ray transitions to measure concentrations of the assigned nuclides in the series are as follows: ^{238}U activities in the samples under investigation were derived from weighted means of the photopeaks of ^{234}Th (63.3, 92.4 and 92.8 keV). ^{226}Ra activity was determined by taking the mean activity of the three separate photopeaks of its daughter nuclides: ^{214}Pb at (295.2 and 352.0 keV) and ^{214}Bi at (609.3 keV). For ^{232}Th determination, the photopeak of ^{228}Ac (at 911.1 keV) and the photopeaks of ^{212}Pb (at 583.1 keV) and ^{208}Tl (at 238.6 keV) were used. ^{40}K was directly determined using the 1460.8 keV photopeak.

The activity concentration (A) in $\text{Bq}\cdot\text{kg}^{-1}$ in the environmental samples was obtained by the following equation:

$$A = \frac{N_p}{e \times E \times m} \quad (1)$$

where N_p is the difference between counts per second of the sample and counts per second of the background, e is the abundance of the γ -peak in a radionuclide, E is the measured efficiency for each gamma-ray peak observed for the same number of channels either for the sample or the calibration source and m is the sample mass in kilograms.

The counting system must have a background as low as attainable with a minimum number of spectral lines originating from natural radionuclides which may be present in the system components and in the surrounding environment of the counting facility. In the present study, measurements of the background count rates for natural radionuclides were carried out at least twice a week, each for a counting time of 80,000 s, and its spectrum was stored in a PC-based multichannel analyzer (MCA). After counting for the specified time, the gamma-ray spectra were automatically calculated and loaded in the PC-based MCA.

Absorbed Gamma Dose Rate, D (nGy/h)

The absorbed dose rates due to gamma radiations in air at 1 m above the ground surface for the uniform distribution of the naturally occurring radionuclides (^{226}Ra , ^{232}Th and ^{40}K) were calculated based on guidelines provided by *UNSCEAR* (2000). The conversion factors used to compute absorbed gamma dose rate (D) in air per unit activity concentration in Bq.kg^{-1} (dry weight) correspond to 0.462 nGy/h for ^{226}Ra , 0.604 nGy/h for ^{232}Th and 0.042 nGy/h for ^{40}K . Therefore, D can be calculated as follows [2]:

$$D \text{ (nGy/h)} = 0.462C_{\text{Ra}} + 0.604C_{\text{Th}} + 0.0417C_{\text{K}} \quad (2)$$

where C_{Ra} , C_{Th} and C_{K} are the activity concentrations of ^{226}Ra , ^{232}Th and ^{40}K in Bq.kg^{-1} , respectively.

Radium Equivalent Index, Ra_{eq}

In comparing the radioactivity of materials that contain ^{226}Ra , ^{232}Th and ^{40}K , a common radium equivalent activity is required to obtain the total activity and is also used to assess the gamma radiation health impact on the public. Since 98% of the radiological effects of the uranium series are produced by radium and its daughter products, the contribution from the ^{238}U and the other ^{226}Ra precursors is usually ignored,

so that the Ra_{eq} of a sample can be expressed as [4]:

$$\text{Ra}_{\text{eq}} \text{ (Bq.kg}^{-1}\text{)} = C_{\text{Ra}} + 1.43C_{\text{Th}} + 0.077C_{\text{K}} \quad (3)$$

where C_{Ra} , C_{Th} and C_{K} are the specific activity values in Bq.kg^{-1} . This equation is based on the assumption that 10 Bq.kg^{-1} of ^{226}Ra , 7 Bq.kg^{-1} of ^{232}Th and 130 Bq.kg^{-1} of ^{40}K produce the same γ -radiation dose rate. The radium equivalent activity of the mean activity of the samples calculated on the basis of the aforementioned relation.

Representative Level Index (I_{yr})

Another radiation hazard index was primarily used to estimate the level of γ radiation associated with different concentrations of some specified radionuclides. It is defined as shown in the following formula [16, 20]:

$$\text{RLI}(I_{\text{yr}}) \text{ (Bq.Kg}^{-1}\text{)} = (1/150) A_{\text{Ra}} + (1/100) A_{\text{Th}} + (1/1500) A_{\text{K}} \quad (4)$$

where A_{Ra} , A_{Th} and A_{K} are the respective activity concentration values of ^{226}Ra , ^{232}Th and ^{40}K in Bq.kg^{-1} .

External Hazard Index, H_{ex}

In the literature, a number of criterion formulae have been derived over the years to assess the radiation dose rate due to exposure to gamma radiation from the natural radionuclides contained in building materials. The merits of these have been reviewed by the OECD's Nuclear Energy Agency (1979).

Karpov and Krisiuk (1980) have proposed a relation for the activity concentrations that limits the annual gamma dose rate inside a room owing to the building material to about 1 mSv. Also, Krieger (1981) proposed the following conservative model based on infinitely thick walls without windows and doors to serve as a criterion for the calculation of external hazard index, H_{ex} , defined as:

$$H_{\text{ex}} = (C_{\text{Ra}}/370) + (C_{\text{Th}}/260) + (C_{\text{K}}/4810) \leq 1 \quad (5)$$

where C_{Ra} , C_{Th} and C_{K} are the activity concentrations of ^{226}Ra , ^{232}Th and ^{40}K in Bq.kg^{-1} , respectively.

Internal Hazard Index, H_{in}

In addition to the external irradiation, radon and its short-lived products are also hazardous to the respiratory organs. The internal hazard index H_{in} is used to control the internal exposure to

^{222}Rn and its radioactive progeny. The internal exposure to radon and its daughter products is quantified by the internal hazard index H_{in} , which is given by the following equation (Krieger, 1981):

$$H_{in} = (C_{Ra}/185) + (C_{Th}/260) + (C_K/4810) \leq 1 \quad (6)$$

where C_{Ra} , C_{Th} and C_K are the activity concentrations of ^{226}Ra , ^{232}Th and ^{40}K in Bq.kg^{-1} , respectively.

Results and discussion

The distribution of natural radionuclides in different brands of cements is presented in Table 1. It can be seen from Table 1 that the activity concentration of ^{226}Ra varies from 29.1 ± 2.01 to $79.2 \pm 3.90 \text{ Bq.kg}^{-1}$. The activity concentration of ^{232}Th varies from 5.8 ± 1.1 to $26.4 \pm 1.9 \text{ Bq.kg}^{-1}$. The activity concentration of ^{40}K varies from

231.9 ± 9.8 to 298.0 ± 10.7 . The mean ^{226}Ra and ^{232}Th values are slightly higher than the corresponding worldwide average values which are 35 and 30 Bq.kg^{-1} , whereas ^{40}K values are lower than the corresponding worldwide average (400 Bq.kg^{-1}) as Table 3 shows. Fig. 1 shows the activity concentrations of natural radionuclides for the cement types. Since the distribution of the natural radionuclides in each cement type is not uniform, a common index termed radium equivalent activity (Ra_{eq}) is required to obtain the total activity and is also used to assess the gamma radiation hazards. The radium equivalent of the total activity of each cement type is shown in Table 2. The highest value of Ra_{eq} is seen with white cement ($125.49 \pm 6.12 \text{ Bq.kg}^{-1}$) and the lowest with Portland Pozzolanic cement (5%) with an average value of ($78.08 \pm 4.03 \text{ Bq.kg}^{-1}$).

TABLE 1. The minimum, maximum and mean activity concentrations of ^{226}Ra , ^{232}Th and ^{40}K for Cement Jordanian Factory products.

Types of Cement	Specific γ - ray activity concentrations (Bq.kg^{-1})								
	^{226}Ra			^{232}Th			^{40}K		
	Min.	Max.	Mean	Min.	Max.	Mean	Min.	Max.	Mean
Portland Cement	40.3	75.6	66.5	9.7	23.9	18.2	150.5	233.8	227.2
Portland Pozzolanic Cement (5%)	31.2	60.1	43.9	9.1	17.1	11.4	200.7	287.0	232.3
Portland Pozzolanic Cement (25%)	39.9	56.3	49.1	7.9	17.0	12.0	193.3	291.9	221.5
Sulphate Resistant Cement (S.R.C.)	29.1	42.0	42.9	5.8	11.3	10.9	231.9	298.0	265.6
White Cement	56.2	79.2	77.2	17.9	26.4	22.9	178.6	219.0	201.9

TABLE 2. Radium equivalent activity (Ra_{eq}), representative level index ($I_{\gamma r}$), gamma dose rate (D), external hazard index (H_{ex}) and internal hazard index (H_{in}), for different brands of cement.

Types of Cement	D (nGy.h^{-1})	Ra_{eq} (Bq.kg^{-1})	$I_{\gamma r}$ (Bq.kg^{-1})	H_{ex}	H_{in}
Portland Cement	51.19	110.02	0.776	0.296	0.476
Portland Pozzolanic Cement(5%)	36.69	78.08	0.559	0.211	0.329
Portland Pozzolanic Cement (25%)	39.01	83.32	0.595	0.225	0.357
Sulphate Resistance Cement (S.R.C.)	37.29	78.93	0.572	0.213	0.329
White Cement	57.91	125.49	0.878	0.339	0.547

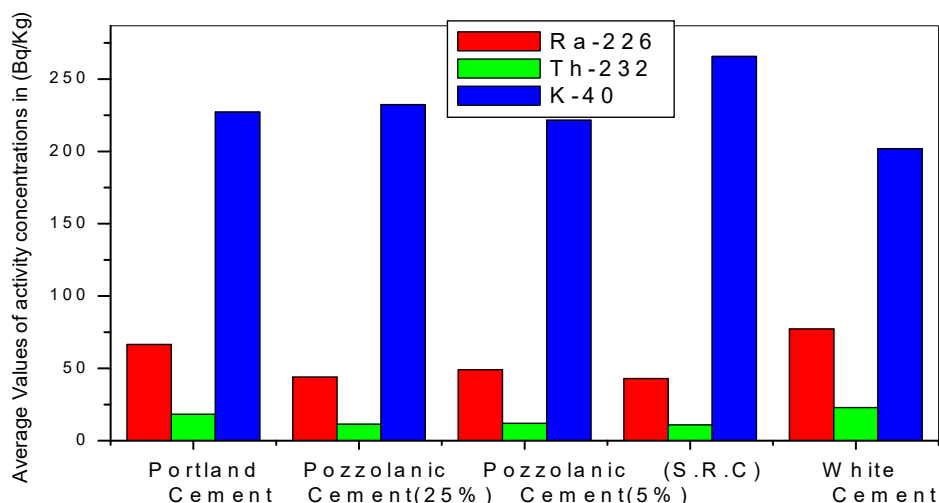


FIG. 1. Different kinds of cements vs. activity concentrations (Bq.kg⁻¹).

However, all the values obtained in this study for Ra_{eq} fall far below the criterion limit, as the use of materials whose Ra_{eq} concentration exceeds (370 Bq.kg⁻¹) is prohibited. It is apparent that the Ra_{eq} of cement samples originating from different types shows considerable variations, which are likely related to the type of raw materials used in cement manufacture. This is important in selecting the suitable cement type for use in building and construction, especially from among those which have large variations in their activities. Fig. 2 shows the variations of radium equivalent activities with the cement types in Jordan.

The radiation hazard indices are primarily used to estimate the level of γ -radiation associated with different concentrations of some specified radionuclides. The representative level index values, the external hazard index values, the internal hazard index values, as estimated using equations (4, 5 and 6) for all types of cements are listed in Table 2. All values are relatively similar compared to each other with the highest value in the representative level index (0.878 Bq.kg⁻¹) for white cement as can be seen from Fig. 3. This would tend to confirm that the samples under investigation exhibit a very low gamma radiation level. The obtained results for the products show that the averages of radiation hazard parameters for all products under investigation are lower than the acceptable

level, 370 Bq.kg⁻¹ for Ra_{eq} , 1 for level index $I_{\gamma r}$ and 59 nGy.h⁻¹ for absorbed dose rate, as shown in Table 2.

Table 3 lists the comparison of activity concentrations in Portland cements in different areas of the world. The activity concentrations of ²²⁶Ra, ²³²Th and ⁴⁰K for all measured samples of Portland cement are comparable with the corresponding values and sometimes less than those of other countries. The radioactivity in Portland cement varies from one country to another because of different materials used in cement manufacture.

Fig. 2 shows a comparison between different kinds of cements used in Jordan in terms of the average values of Ra_{eq} and dose rate. It can be seen that white cement has the greatest values of Ra_{eq} and dose rate among all types of cements, while Pozzolanic cement with higher Pozzolan substitutions has the smallest values.

Another comparison can be noticed from Fig. 3 between different hazard indices among all kinds of cement. The highest values of representative level index $I_{\gamma r}$ and internal hazard index H_{in} are associated with Portland and white cement. The obtained results show that the averages of radiation hazard parameters for all kinds of cements are lower than the acceptable levels.

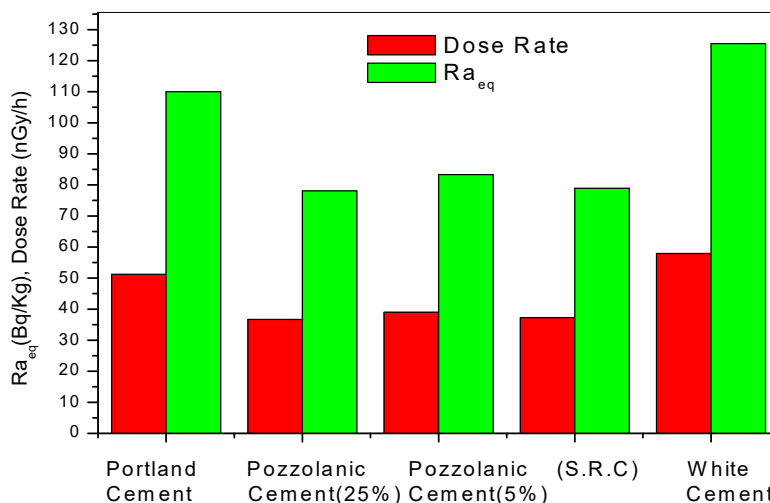


FIG. 2. Comparison between the average values of radium equivalent, Ra_{eq} , and dose rate in different kinds of cement in Jordan.

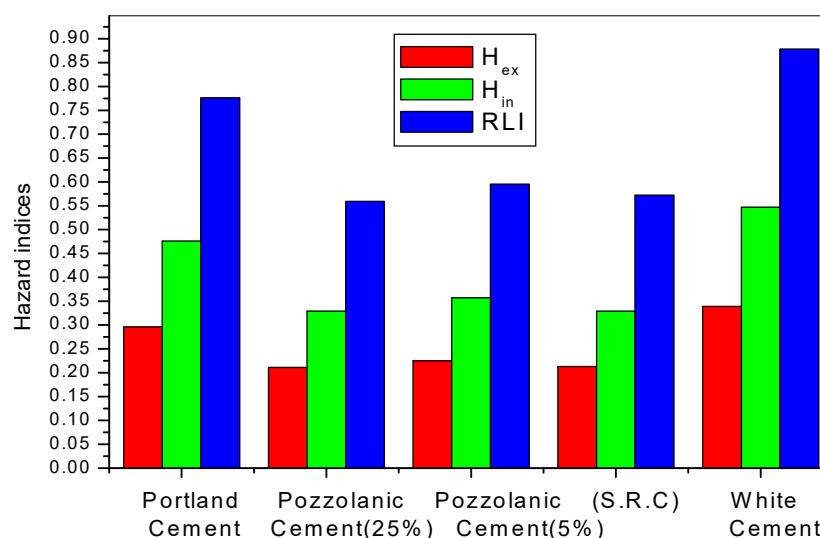


FIG. 3. Comparison between different hazard indices in different kinds of cement in Jordan.

TABLE 3. Comparison between the activity concentrations of Portland cement samples from Cement Jordanian Factory with those of other countries.

Country	Activity Concentration ($Bq.kg^{-1}$)			Reference
	^{226}Ra	^{232}Th	^{40}K	
Finland	44.0	26.0	241.0	NEA-OECD (1979)
Brazil	61.7	58.5	564.0	Malanca et al. (1993)
Pakistan	31.3	26.8	212.0	Tufail et al. (2007)
Cuba	23.0	11.0	467.0	Brigido Flores et al. (2008)
Sweden	96.0	127	962.0	NEA-OECD (1979)
Australia	51.8	48.1	115.0	Beretka and Matthew (1985)
Austria	26.1	14.2	210.0	Sorantin and Steger (1984)
China	69.3	62.0	169.0	Ziqiang et al. (1988)
Germany	26.0	18.0	241.0	NEA-OECD (1979)
United Kingdom	22.0	7.00	141.0	NEA-OECD (1979)
Egypt	31.3	11.1	40.60	Sharaf et al. (1999)
Present work	66.5	18.2	27.20	---
World	35.0	30.0	400.0	UNSCEAR (2000)

Conclusion

Based on the assessment of potential radiological hazards as inferred from the calculations of radium equivalent activity, representative level index and dose rate, the investigated cement samples fall within the category of accepted building materials and are safe to use for the construction of inhabited buildings.

The results may be important from the point of view of selecting suitable materials for use in

cement manufacture. Cement products do not pose a significant radiological hazard when used for building construction.

Acknowledgment

This work has been carried out during a sabbatical leave granted to the author from Al-Balqa Applied University-Jordan during the academic year (2015/2016).

References

- [1] Pakou, A., Assimakopoulos, P. and Prapidis, M., *Sci. Total Environ.*, 144 (1994) 255.
- [2] UNSCEAR, Sources and effects of ionizing radiation. Report to General Assembly with Scientific Annexes, United Nations Scientific Committee on the Effects of Atomic Radiation, United Nations, New York (2000).
- [3] Ackers, J., Den-Boer, J., de-Jong, P. and Wolschrijn, R., *Sci. Total Environ.*, 45 (1985) 151.
- [4] Beretka, J. and Mathew P., *Health Phys.*, 48 (1) (1985) 87.
- [5] Khan, K., Khan, H., Tufail, M. and Ahmad, N., *J. Environ. Radioac.*, 38 (1998) 77.
- [6] Tufail, M., Ahmad, N., Mirza, S., Mirza, N. and Khan, H., *Sci. Total Environ.*, 121 (1992) 283.
- [7] Tzortzis, M., Tsertos, H., Christofides, S. and Christodoulides, G., *Radiat. Meas.*, 37 (2003) 221.
- [8] Ziqiang, P., Yin, Y. and Mingqiang, G., *Radiat. Prot. Dosim.*, 24 (1988) 29.
- [9] Projin, A., Bourgoignie, R., Marjins, R., Janssens, A. and Jacobs, R., *Radiat. Protect. Dosim.*, 7 (1984) 77.
- [10] Sciocchetti, G., Scacco, F. and Baldassini, P., *Radiat. Protect. Dosim.*, 7 (1984) 347.
- [11] Malanca, A., Pessina, V. and Dallara, G., *Radiat. Protect. Dosim.*, 24 (1993) 27.
- [12] Mollah, A., Ahmed, G., Hussain, S. and Rahman, M., *Health Phys.*, 50 (1986) 849.
- [13] Mustonen, R., *Sci. Total Environ.*, 45 (1986) 127.
- [14] Paredes, C., Kessler, W., Landolt, R., Ziemer, P. and Panstenbach, D., *Health Phys.*, 53 (1987) 23.
- [15] Alam, M., Chowdhury, M., Kamal, M., Ghose, S., and Ismail, M., *J. Environ. Radioact.*, 46 (1999) 243.
- [16] Stranden, E. and Berteiz, L., *Health Phys.*, 39 (1980) 275.
- [17] Sideris, K., Savva, A. and Papayianni, J., *Cem. and Conc. Comp.*, 28 (2006) 47.
- [18] Massazza, F., *J. Turkish Cement Manufacturers' Association. Cem. and Conc. World*, 3 (1999) 19.
- [19] NEA-OECD, Nuclear Energy Agency. Exposure to Radiation from Natural Radioactivity in Building Materials. Report by NEA Group of Experts, OECD, Paris (1979).
- [20] Karpov, V. and Krišiuik E., *Health Phys.*, 39 (1980) 819.
- [21] Krieger, R., *Betonwerk Fertigteil Technol.*, 47 (1981) 468.

Optical Constants Determination of Thermally-Evaporated Undoped Lead Iodide Films from Transmission Spectra Using the PUMA Method

Mahmoud H. Saleh

Department of Physics, Faculty of Science, Al-Balqa Applied University, Al-Salt 19117, Jordan.

Received on: 9/5/2018;

Accepted on: 24/6/2018

Abstract: 0.7- μm thick lead iodide (PbI_2) films thermally-evaporated on glass substrates held at different temperatures T_s (35 – 195 °C) are studied. Typical observed X-ray diffraction (XRD) patterns and scanning electron microscope (SEM) micrographs of such PbI_2 films prepared at high substrate temperatures T_s (> 100 °C) were found to be crystalline with hexagonal 2H-polytypic structure with the c -axis perpendicular to the surface. The room-temperature normal-incidence transmittance $T_{\text{exp}}(\lambda)$ of the PbI_2 films has been measured as a function of spectral wavelength λ in the range 300 – 1100 nm and was used to retrieve the spectral dependence of their optical constants $n(\lambda)$ and $\kappa(\lambda)$ using the Pointwise Unconstrained Minimization Approach (PUMA) method. The energy variation of the absorption coefficient $\alpha(\lambda) (= 4\pi\kappa(\lambda)/\lambda)$ of the PbI_2 films in the region of strong optical absorption was analyzed using various interband transition models and was found to be reasonably described by an approximate power-law relation $ahv \propto (hv - E)^m$, with $m = 2$ and $E_g^{\text{opt}} \cong 2.2$ eV ($\pm 2\%$) (Tauc interband dielectric model, where E_g^{opt} is the optical bandgap energy). But, it is more remarkable for $m = 1/2$ and $E_g \cong 2.45$ eV ($\pm 2\%$) (direct interband transition model) over a broader spectral range. For $T_s > 100$ °C and in the transparent and weak absorption regions, the PUMA-retrieved $n(\lambda) - \lambda$ data of the PbI_2 films was found to fit the Wemple-DiDomenico (WDD) dispersion formula, with bandgap energy parameter $E_o \cong 3.9$ eV $\cong 2 E_g^{\text{opt}}$, single-oscillator energy strength $E_d \cong 19$ eV and static index of refraction $n_o \cong 2.5$. Analysis of the data in the absorption tail to Urbach formula yielded an Urbach-tail parameter Γ_U that decreased with increasing substrate temperature to a value around 75 meV at the high substrate temperature side. These results indicate that using film growth temperatures beyond 100 °C leads to an enhancement in the crystallinity of the PbI_2 films and reduces band tailing.

Keywords: PbI_2 films, Optical constants, PUMA method, Wemple-DiDomenico model, Interband transition models.

Introduction

Lead iodide (PbI_2) is considered an attractive material in the fabrication of many technological devices, such as photocells and room-temperature (RT) crystalline radiation detectors and X-ray diagnostic imaging systems for detecting low and intermediate energy X- and γ -rays (1 keV – 1 MeV), as PbI_2 can efficiently

operate over a wide temperature range ($-200^\circ\text{C} - 130^\circ\text{C}$) [1, 6]. This is because purely crystalline PbI_2 is a direct band-gap p-type compound semiconductor with large band gap energy E_g of (~ 2.5 eV) and high dark dc resistivity ($\rho \sim 10^{13} \Omega \cdot \text{m}$ at 300K) [2-8]; thus giving rise to low-noise and low leakage current in devices incorporating it [2-4]. Moreover, lead

iodide requires rather small energy for the creation of an electron-hole pair ($E_{e-h} \sim 5 - 6.6$ eV); thus producing many charge carriers with high signal-to-noise electrical response [2, 5, 6]. Lead iodide possesses several other advantageous physical properties; for example, PbI_2 has a high melting point (~ 405 °C), high quantum efficiency [4-8], high mass density (6.2 g/cm³) and is composed of elements of large atomic numbers ($Z_{\text{Pb}} = 82$ and $Z_{\text{I}} = 53$); hence exhibiting high photon stopping power (due to its high atomic absorption coefficient $\sim 10^5$ cm⁻¹) [5-12]. These features are supposed to render lead iodide to be structurally stable and efficient in a variety of room-temperature electronic devices incorporating crystals and polycrystalline layers (films) designed from this material.

However, despite the rich literature work spent on lead iodide crystals and films, some important physical properties demand more attention and detailed investigation of their optical constants and bandgap structure. In fact, determination of optical parameters of semiconducting samples, such as polycrystalline PbI_2 films from data of optical spectroscopic measurements made on film-substrate structure, is not a simple task and requires rigorous and sophisticated analytical and computational tools [13-19]. Several methods have been used for analyzing optical transmittance spectra of four-layered optical film substrate of the (air/film/substrate/air) configuration, such as conventional-iterative curve fitting programs [13], algebraic Swanepoel envelope method [14-16] and Pointwise Unconstrained Minimization Approach (PUMA) method [17-19]. Regarding lead iodide films, no literature studies have been carried out of their optical transmittance (or reflectance) spectra by the numeric PUMA method [17-19], which does not require, as the Swanepoel envelope method, the use of dielectric dispersion relations for the optical constant of studied films, but retrieves them as an output of its numeric analysis [14, 15].

In the present work, the numeric PUMA method will be adopted to analyze measured normal-incidence transmittance $T_{\text{exp}}(\lambda) - \lambda$ data of {air/ PbI_2 film/thick glass slide/air}-samples. One of the usual algebraic methods is the Swanepoel envelope method, which is usable if the measured transmittance spectrum displays many maxima and minima fringes in the optically transparent and weakly-absorbing

regions of its film and substrate [14, 15]. The numeric PUMA method does not need any dispersion relations a priori or the number of interference maxima and minima fringes on the $T_{\text{exp}}(\lambda)$ spectra to exploit the effectiveness of this method for analyzing optical spectra of multi-layered structures and use its output results to acquire more insight into spectral dispersion of the dielectric and optical functions of PbI_2 films. [17-19]. Further, most of publications on thin PbI_2 films are concerned with the analysis of experimental transmission spectra based on basic traditional calculations [20-29].

Experimental Details

Conventional vacuum thermal evaporation was used to prepare lead iodide thin films on glass slides from commercial lead iodide powder (BDH, England) that was ground into fine powder, which was purified to get crystal chunks. The purified lead iodide powder was then placed in a molybdenum crucible situated below the substrates inside the vacuum chamber of a Leybold deposition system (LEYBOLD-HERAEUS UNIVEX 300) which was pumped down to pressure around 10^{-5} mbar. The glass substrates located 15 cm above the crucible were maintained at a constant temperature T_s in the range (35 – 195 °C). In each deposition run, a batch of lead iodide films of geometric thickness d around 0.7 μm , as recorded by an INFICON-XTC quartz crystal monitor unit, were produced at low evaporation rates (10 – 20 Å/s). Table 1 shows labelling of the studied thermally-evaporated lead iodide films prepared at different substrate temperatures T_s . The structure and surface morphology of these lead iodide films were then characterized by room-temperature X-ray diffraction (XRD) (SHIMADZU XRD-7000 diffractometer), scanning electron microscopy (SEM) (Inspect F50 model Eindhoven) and energy dispersive X-ray analysis (EDAX) detector (Bruker Microanalysis GmbH).

TABLE 1. Preparation conditions of lead iodide films prepared by the thermal-evaporation technique.

Sample label	Substrate temperature T_s (°C)
S35	35
S95	95
S125	125
S160	160
S195	195

The specular transmittance values of a typical 1.1-mm thick glass slide standing freely in air and of the (PbI₂-film/glass substrate) samples were measured at room temperature as a function of wavelength λ of collimated light incident normally at the air-film interface using a conventional double-beam UV-VIS-NIR spectrophotometer (SHIMADZU UV-1800). All normal-incidence transmittance measurements were taken relative to air-baseline transmission normalized to 100%, with the sample being placed in the path of a spectrophotometer light beam and the reference-beam path always left open. The wavelength was scanned in the range 300 – 1100 nm at a rate of 120 nm/min and 0.5 nm-interval, with 0.5 nm spectral bandwidth (SBW) of the incident light beam to minimize the SBW effect on the shape and features of transmittance spectra of the studied PbI₂/glass-substrate samples.

Results and Discussion

Structure of Evaporated Lead Iodide Films

Lead iodide films produced from purified lead iodide crystalline chunks by thermal evaporation on glass slides held at high substrate temperatures were found to be preferentially crystalline in the 2H-polytype hexagonal structure along the *c*-axis, alongside the (00*l*) lattice orientation directions. These findings are clearly revealed from their measured X-ray diffraction (XRD) patterns and scanning electron microscope (SEM) micrographs as shown in Fig. 1 a and b for a typical 0.7- μ m thick lead iodide film prepared at substrate temperatures T_s (35 and 160 °C). The lead iodide films were polycrystalline at low substrate temperatures ($T_s < 100$ °C). However, increasing T_s above 100 °C, the 2H-polytype hexagonal structure of lead iodide films has been largely enhanced, where the polycrystallinity features diminished and the films became preferably crystalline along the *c*-axis of hexagonal structure. These features are noted from their measured XRD patterns and SEM micrographs and agree with previous studies prepared PbI₂ films by thermal-evaporation [30], but different from PbI₂ films prepared by flash-evaporation method [21, 31]. Microscopic visualization showed that the deposited PbI₂ films were free from pin holes and cracks; their SEM micrographs manifested smooth and homogeneous surfaces.

The XRD patterns and SEM micrographs of the lead iodide films that were prepared at $T_s > 100$ °C are similar to those reported in the literature for PbI₂ films prepared by conventional thermal evaporation at high substrate temperatures [12, 25, 30] and with those found for PbI₂ films prepared by flash evaporation [21, 31], by physical vapor deposition similar to those used in the present work (PVD) [23, 32, 33] and to some extent with those XRD results reported for lead iodide films prepared by the chemical dipping method [24]. However, the obtained XRD patterns and SEM micrographs of thermally prepared lead iodide films in the present work are inconsistent with the good results for polycrystalline PbI₂ films prepared by spray pyrolysis [20], spin coating [26] and conventional thermal evaporation at low substrate temperatures [22, 28, 30].

The energy dispersive spectroscopy (EDS) measurements on evaporated PbI₂ films showed that these films were nearly stoichiometric with PbI_(0.7-1.45)-composition-depending T_s . The EDS results of evaporated lead iodide films in the present work are better than the EDS compositions reported for lead iodide films prepared by the spray pyrolysis method [20] and by the chemical dipping method [24].

Normal-Incidence Optical Transmittance Spectra of {Lead Iodide/Glass-Substrate} Samples

In measuring normal-incidence transmission of {air/PbI₂ film/glass slide/air}-samples, monochromatic light beams with reasonably small SBWs (≤ 2 nm) were used, so the effect of slit width on their $T_{\text{exp}}(\lambda) - \lambda$ spectra is not significant [14]. Typical room-temperature $T_{\text{exp}}(\lambda) - \lambda$ spectra of these samples at different substrate temperatures (35-195 °C) are shown in Fig. 2, which shows some prominent features that can be useful in their forthcoming optical analysis.

For PbI₂ films prepared at low T_s , the decrease of transmittance in the absorption-edge is not steep, but exhibits a monotonic gradual decrease with wavelength, suggesting that the crystallinity of these films is not as good as that of films prepared at high T_s ; a feature that can be due to lattice disorder and non-stoichiometric defects present in them. It is noticed from Fig. 2 that the $T_{\text{exp}}(\lambda)$ curve of the 0.7- μ m thick PbI₂ films prepared at high substrate temperatures T_s

(>100 °C) clearly illustrates a sharp fundamental absorption-edge near the spectral wavelength $\lambda \approx 520$ nm [21, 30-32]. This indicates that this

film is crystalline and is in good agreement with the XRD and SEM results observed for our films at high T_s (see Fig. 1).

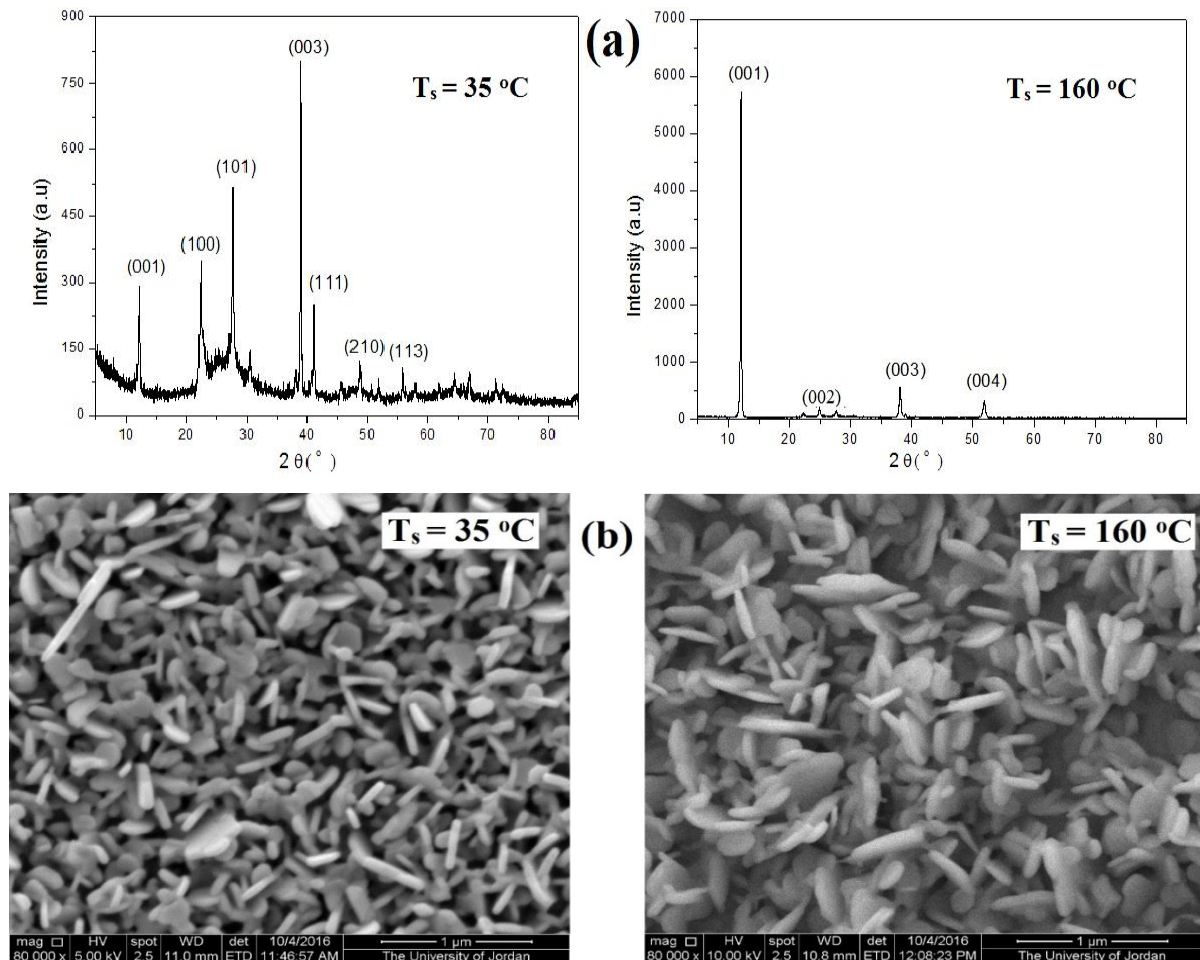


FIG. 1. (a) XRD pattern and (b) SEM micrograph for the 0.7- μm thick evaporated lead iodide film prepared at T_s (35 and 160 °C). (After permission from the author of Ref. [30]).

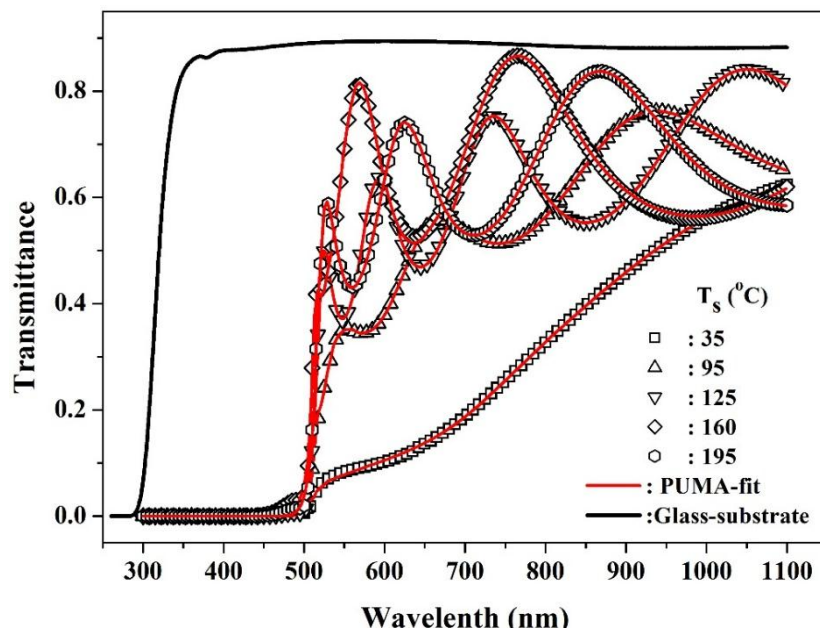


FIG. 2. As-measured normal-incidence $T_{\text{exp}}(\lambda) - \lambda$ spectra and their calculated PUMA-fit $T(\lambda) - \lambda$ curves for the thermally-evaporated PbI_2 films prepared at different substrate temperatures T_s (35-195 °C).

First, in the wavelength range 550-1100 nm, the $T_{\text{exp}}(\lambda) - \lambda$ curves of studied PbI₂ film/glass substrate samples exhibit high optical transmission that is characteristic of the weak/medium and transparent absorption regions of lead iodide. Their $T_{\text{exp}}(\lambda) - \lambda$ spectra at low substrate temperature < 100 °C were noted to be monotonic with variation of wavelength and no significant interference-fringe features have been observed; However, well resolved interference-fringes have been exhibited at higher T_s , suggesting that the lead iodide films deposited at high substrate temperatures become highly crystalline and relatively uniform in thickness. In the weak absorption and transparent regions of lead iodide films laid on glass substrates with extinction coefficients $\kappa(\lambda)$ and $\kappa_s(\lambda)$, the associated absorption coefficients $\alpha(\lambda) = 4\pi\kappa/\lambda$ and $\alpha_s(\lambda) = 4\pi\kappa_s/\lambda$ almost vanish and their $T_{\text{exp}}(\lambda) - \lambda$ spectra are just determined by their indices of refraction $n(\lambda)$ and $n_s(\lambda)$, where (s) designates the substrate material [14, 15].

Second, at a specific cut-off wavelength λ_c (≈ 520) nm and spectral wavelengths below, the measured $T_{\text{exp}}(\lambda) - \lambda$ curves of studied PbI₂-films/glass substrate samples are seen to decline steadily towards zero transmittance, where λ_c represents the border of the absorption edge of the film material, which is for PbI₂ larger than that of soda-lime glass substrates ($\lambda_c \sim 350$ nm). In the strong absorption region ($\lambda < \lambda_c$) of lead iodide films, the transmission curves disappear of the (film/substrate) samples from the observed normal-incidence $T_{\text{exp}}(\lambda) - \lambda$ spectra and their transmission is exclusively determined by the absorption coefficient $\alpha(\lambda)$ of lead iodide films. This model approximation is helpful when discussing features of transmittance spectra of semiconducting films in the strong absorption region, where a drop in their transmission curves with decreasing wavelength occurs [16-19]. At $\lambda < \lambda_c$, absence of abrupt transmission of PbI₂ films prepared at low T_s can be accounted for by assuming that native and disorder structural imperfections (defects) and thickness non-uniformity are present in their thermally-evaporated PbI₂ films, which means lower crystallinity in comparison to the prepared films at high T_s that show clear interference-fringes and somewhat sharp dealing in $T_{\text{exp}}(\lambda)$.

Since $T(\lambda)$ is not an intrinsic property of the material, further analysis of the $T_{\text{exp}}(\lambda)$ data of air-supported PbI₂-film/ glass-substrate samples by the PUMA method is needed to determine the dependency of their optical constants on the spectral wavelength λ or photon energy ($E = h\nu$) of the light incident onto them, where ν is its frequency and h is Planck's constant. The obtained results will then be used to elucidate the spectral dispersion of $n(\lambda)$ and $\kappa(\lambda)$ of PbI₂ films, besides exploiting the variation of their calculated absorption coefficient $\alpha(h\nu)$ with $h\nu$ to have further insight into the interband transitions responsible for optical absorption processes in these PbI₂ films. The PUMA method is an optical analysis that yields simulation curves that fit the measured spectra and retrieves optical constants $n(\lambda)$ and $\kappa(\lambda)$ of studied films as a function of wavelength λ [17]. This is in contrast to conventional curves fitting of experimental transmittance spectra of a multi-layered structure to a theoretical model that usually requires several suitable constant dispersion functions and must yield global solution of the problem to get true physically meaningful results. These problems are overcome by making use of the PUMA program to analyze normal-incidence transmittance of multi-layered structures, without prior need for dispersion relations [18, 19]. The PUMA software is free to download from the PUMA home page (<http://www.ime.usp.br/~egbirgin/puma>). The present optical analysis uses the PUMA program that characterizes the transmittance $T(\lambda)$ spectrum of single-film four-layered structures, with the numeric $n_s(\lambda)$ -formula of the film's substrate (assumed transparent $\kappa_s(\lambda) = 0$) given without any film dispersion relations being given. The PUMA program is pertinent, whether the measured transmittance spectra of such stacks exhibit interference fringes or not [17-19].

The PUMA program iteratively minimizes, *via specific ad hoc* procedure, the difference between $T_{\text{exp}}(\lambda)$ and calculated $T\{\lambda; n(\lambda), \kappa(\lambda)\}$ to get a solution, under a diversity of physical restrictions on the unknowns $n(\lambda)$ and $\kappa(\lambda)$ between the chosen minimum and maximum wavelengths λ that would lead to the equality $T_{\text{exp}}(\lambda) \cong T\{\lambda; n(\lambda), \kappa(\lambda)\}$ [18, 19].

Fig. 2 displays the correspondence between the measured normal-incidence $T_{\text{exp}}(\lambda) - \lambda$ spectra of the thermally-evaporated PbI_2 films studied in the present work and the simulated $T(\lambda) - \lambda$ curves that were recovered from the analysis of these $T_{\text{exp}}(\lambda) - \lambda$ spectra using the successive version of the PUMA program [17-19]. The transmittance curves retrieved from PUMA program profoundly simulate the measured transmittance spectra of such PbI_2 films over the entire spectral range studied.

Fig. 3 displays the variance of extinction coefficient $\kappa(\lambda)$ with λ of the PbI_2 films,

calculated using the results obtained from the analysis of $T_{\text{exp}}(\lambda)$ -spectra of their (film/substrate)-samples by the numeric PUMA method that employs the normal-incidence transmittance formulation [14-16, 18]. It can be noted from Fig. 3 that for $\lambda > 550$ nm, the values of $\kappa(\lambda)$ of studied PbI_2 films are (~ 0.02) almost negligible, but $\kappa(\lambda)$ starts to increase steadily with decreasing wavelength. The inset to Fig. 3 shows the $\alpha(h\nu) - h\nu$ plots for the PbI_2 films, where the absorption coefficient $\alpha(\lambda)$ was calculated from $\kappa(\lambda)$ using the relation

$$\alpha(\lambda) = 4\pi\kappa(\lambda)/\lambda. \quad (1)$$

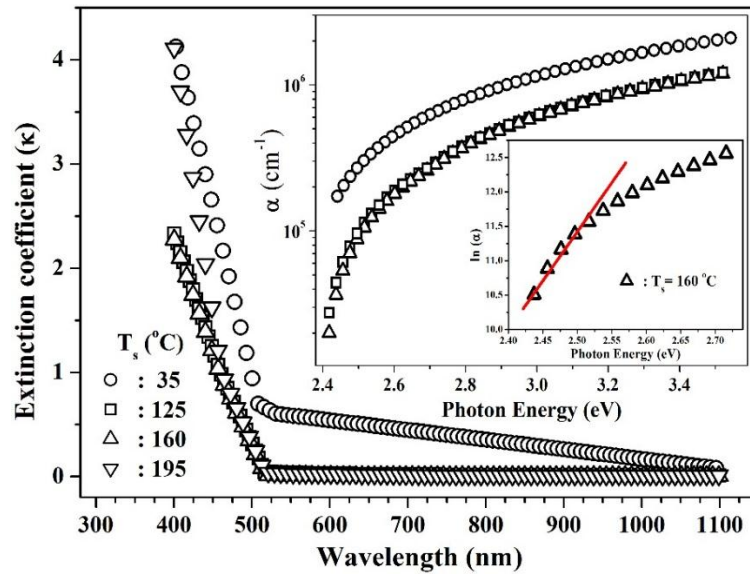


FIG. 3. Dispersion of extinction coefficient $\kappa(\lambda)$ of PbI_2 films retrieved from PUMA-analysis of their measured transmittance spectra. The inset shows the variation of absorption coefficient $\alpha(E)$ with photon energy E , depicting fits of low-energy $\alpha(E) - E$ data of the PbI_2 film prepared at ($T_s = 160$ °C) to Urbach exponential formula of Eq. (2).

The PUMA-retrieved dependency of $\alpha(h\nu)$ on $h\nu$ is nearly similar at high photon energies (> 2.5 eV). This can be related to band-gap absorption being affected by localized energy states in the band gap (Urbach-tails) due to some disorder and native defects in PbI_2 films [13]. Analysis of low energy part of $\alpha(h\nu) - h\nu$ data close to the absorption edge of a semiconductor, in view of the Urbach formula given below in Eq. (2), is assumed to give small but physically significant values for the range of bandgap tails (Urbach-tail breadth Γ_U) [13, 17, 34, 35].

$$\alpha(h\nu) = \alpha_o \exp[(h\nu - E_{0U})/\Gamma_U] \quad (2)$$

where Γ_U is the Urbach energy equal to the energy width of the absorption-edge tail which can be calculated from the relation $\Gamma_U^{-1} = \Delta(\ln \alpha)/\Delta(h\nu)$ and α_o and E_{0U} are the

coordinates of the convergence point of the Urbach “bundle” [34]. For the ($\text{PbI}_2/\text{glass}$)-samples of this work, the analysis result of PUMA-calculated $\alpha(h\nu)$ data in the (Urbach-tail) part is plotted in the inset of Fig. 3 as a $\ln[\alpha(h\nu)]$ plot for the PbI_2 film prepared at $T_s = 160$ °C. The slopes, derived from fits of low-energy linear parts of $\ln[\alpha(h\nu)] - h\nu$ plots, give the Urbach-tail breadths Γ_U for studied PbI_2 films and are listed in Table 2. The values of Urbach-tail parameter Γ_U for the films prepared at 35 °C were relatively high, but at high substrate temperatures, these values were around (70 – 80 meV) and are in agreement with those reported by Ghosh [23]. It is noted from Table 2, that the values of Γ_U decreased with increasing T_s , indicating that with increasing T_s at which the PbI_2 films were prepared, their crystallinity was

enhanced as the disorder lattice become less effective.

To investigate the properties of band-to-band optical absorption in a semiconducting film, the change of its absorption coefficient at the edge of optical absorption region of the material is usually exploited as a function of the incident photon energy $h\nu$. Several theoretical and experimental approaches have tackled the phenomenon of optical absorption in semiconductors [36]. The approximate formulations generally adopted to describe the behavior of the absorption coefficient $\alpha(h\nu)$ in semiconductors in their interband transition regions have been employed in this work using the $\alpha(h\nu) - h\nu$ data calculated from the PUMA-analysis of $T_{\text{exp}}(\lambda)$ spectra of (PbI₂/glass) samples. Various optical absorption models, both the direct and indirect interband transition models, are often described by Eq. (3) and have been commonly adopted to clarify the mechanism of optical absorption in the absorption-edge region [13, 17, 36-38], viz.

$$\alpha h\nu = A (h\nu - E_g)^m \quad (3)$$

where A is a constant of the sample material that is almost independent of the photon energy. For allowed indirect and direct band-to-band transitions, $m = 2$ and $m = 1/2$, respectively. As lead iodide is usually considered to be a

direct-band p -type semiconductor compound, the $\alpha(h\nu) - h\nu$ formula being used in this work is that which allows direct band-to-band electronic transitions; namely, $(\alpha h\nu)^2 = A(h\nu - E_g)$ [12, 21-29]. The direct and indirect interband transition models were these treated in detail and employed to analyze PUMA-retrieved $\alpha(h\nu) - h\nu$ data of PbI₂ films studied in this work by presenting this data on $[\alpha h\nu]^{1/2} - h\nu$ and $[\alpha h\nu]^2 - h\nu$ plots as seen in Fig. 4 for typical (PbI₂/glass) samples. It was found that intersections (bandgap energy) of linear portions of these plots with $h\nu$ -axis, deduced from curve-fits of the $\alpha(h\nu) - h\nu$ data to Tauc (indirect) law $\{\alpha h\nu \propto (h\nu - E_g^{\text{opt}})^2\}$ and to the direct interband-transition relation $\{\alpha h\nu \propto (\sqrt{h\nu - E_g})\}$, do not match with each other. Figure 4 depicts curve-fits of PUMA-retrieved $\alpha(h\nu) - h\nu$ data of PbI₂ films to the Tauc formulae and direct interband transition models, with the Tauc optical bandgap energy E_g^{opt} and the direct bandgap energy E_g around 2.2 eV and 2.45 eV, respectively (see Table 2). The values of E_g (~ 2.5 eV) for the PbI₂ films studied in this work agree with the results of the direct energy gap calculated from other studies on PbI₂ films [12, 21-29]. Some studies [12, 22, 26-29] found that the direct E_g decreases as the film thickness increases.

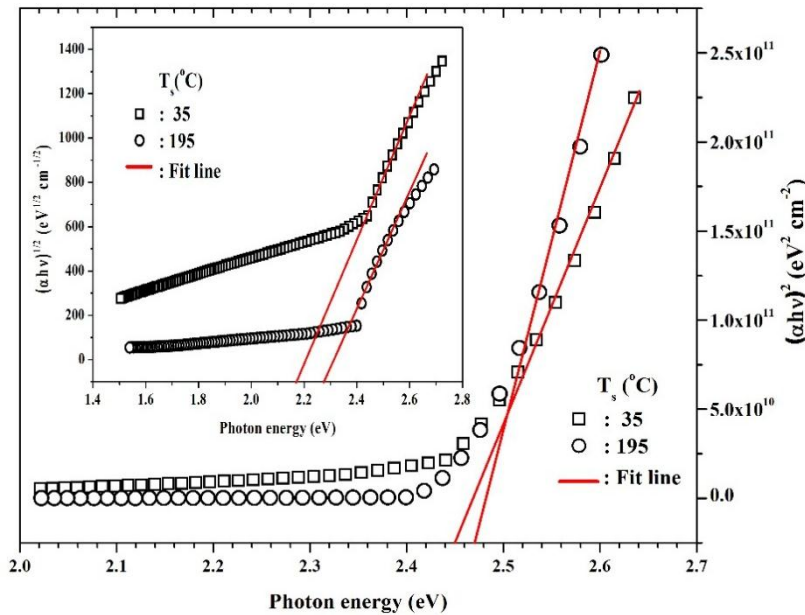


FIG. 4. PUMA-retrieved $\alpha(h\nu) - h\nu$ data of PbI₂ films on $(\alpha h\nu)^2 - h\nu$ and least-square fits (lines) of linear portions on such plots for the PbI₂ films prepared at T_s (35 and 195 °C). Inset depicts $\sqrt{\alpha h\nu} - h\nu$ (Tauc-law) plots.

There is some controversy over the origin and properties of interband optical absorption in lead iodide and hence on the real value of bandgap energy, which has been obtained from the direct interband transition model [12, 21-29]. Analysis of $\alpha(h\nu) - h\nu$ data of PbI_2 films showed that optical absorption in PbI_2 films can be described by the indirect interband transition model over a narrow range of photon energies, but can be represented by the direct interband transition model on the basis of the $(\alpha h\nu)^2 \propto (h\nu - E_g)$ formula over a broader spectral range in the strong absorption-edge region, over which this direct formulation has been discussed by other researchers to give the best fit of the $\alpha(h\nu) - h\nu$ data of their PbI_2 films [12, 21-29]. The quality and crystallinity of the prepared PbI_2 films seem to be the reason behind the diversity of the determined values of bandgap energy of PbI_2 , in addition to the use of different interband and sub-bandgap transition models to exploit its optical absorption phenomenon. Nonetheless, such diversity in the values of the bandgap

energy of PbI_2 that were deduced based on different absorption models critically depends on which data points are selected to be curve-fitted to a linear portion on the $(\alpha h\nu)^{1/m} - (h\nu - E_g)$ plots.

The quality of PbI_2 films and their performance were integrated in optical/electronic devices and this can be exploited from studying their index of refraction $n(\lambda)$ and optical dispersion. Fig. 5 shows the wavelength dispersion of the index of refraction $n(\lambda)$ of the PbI_2 films of the present work. The $n(\lambda) - \lambda$ data has been obtained from the analysis of the ($\text{PbI}_2/\text{glass-substrate}$) samples using the numeric PUMA program [14, 18]. For $\lambda > 550$ nm, the values of $n(\lambda)$ are nearly the same for studied films, pointing that PUMA method works acceptably well for comparatively thick films and PbI_2 films had no major divergence in their properties, implying that their fabrication procedures were alike.

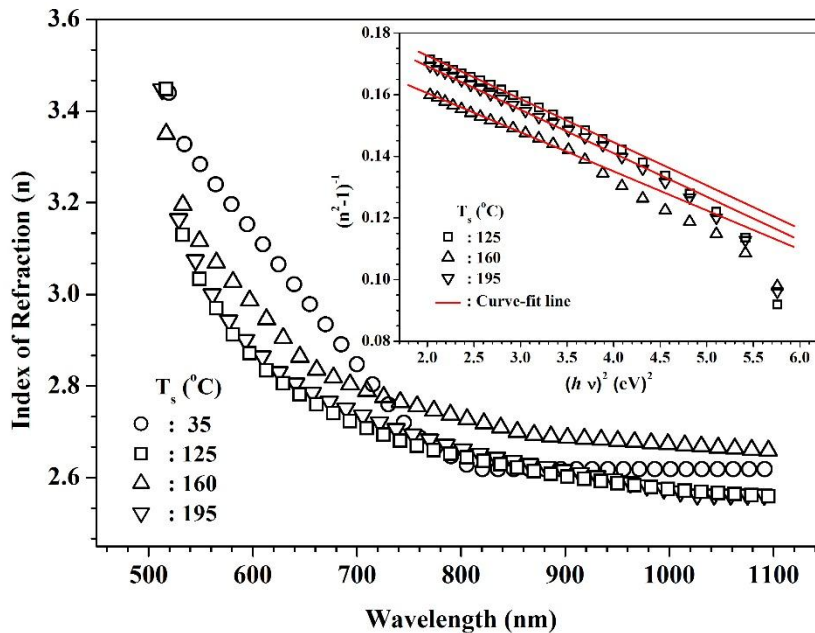


FIG. 5 Spectral dispersion of index of refraction $n(\lambda)$ of PbI_2 films determined from PUMA analysis of $T_{\text{exp}}(\lambda)$ spectra of their samples. The inset depicts curve-fits of low photon-energy PUMA-retrieved $\{[n(E)]^2 - 1\}^{-1} - E^2$ data of PbI_2 films to the Wemple-DiDomenico dispersion formula: Eq. (4).

The change of $n(\lambda)$ of a film in its optical transparency and absorption ranges with λ can be analyzed using the Wemple-DiDomenico (WDD) $n(E) - E$ dispersion formula, which is expressed in terms of photon energy $E_{\text{ph}} (= h\nu)$ of the light beam striking the film in the relation [40]:

$$[n(h\nu)]^2 = 1 + \frac{E_0 E_d}{E_0^2 - (h\nu)^2} \quad (4)$$

The WDD formula includes two constant parameters, which are related to the physical properties of the material: the single-oscillator energy parameter E_0 , related to the Tauc optical bandgap energy as $E_0 \cong 2E_g^{\text{opt}}$ [36, 40] and the

Using the PUMA Method

single-oscillator energy strength E_d . Using the PUMA-retrieved $n(\lambda)$ data, the variation of $n(\lambda)$ with $h\nu$ was achieved by plotting $\{[n(h\nu)]^2 - 1\}^{-1} - V_s - (h\nu)^2$ as seen in the inset to Fig. 5, where the intercept ($= E_o/E_d$) of a linear part at $h\nu = 0$ and slope ($= -1/E_d E_o$) can be used to calculate the static index of refraction $n_o = \sqrt{1 + E_d/E_o}$ [40]. The obtained values of E_o , E_d

and n_o for thermally-evaporated PbI_2 films in this work are listed in Table 2. This shows that the optical analysis founded on the PUMA method is successful in our spectral range and shows that for $T_s > 100$ °C, the bandgap energy parameter $E_o \cong 3.9$ eV, single-oscillator energy strength $E_d \cong 19$ eV and static index of refraction $n_o \cong 2.5$.

TABLE 2. The PUMA-retrieved data of PbI_2 films and fit parameters found from curve-fits of their PUMA-retrieved $n(\lambda) - \lambda$ data to Wemple-DiDomenico (WDD) dispersion formula, $\alpha(h\nu) - h\nu$ data to Tauc and direct interband transition models and to Urbach-tail formula.

Method of analyzing optical constants		Sample	S35	S95	S125	S160	S195
fit parameter							
WDD $n(E)$ -formula, Eq. (4)		E_d (eV)	24.9	15.4	19.9	18.3	19.1
		E_o (eV)	3.87	3.98	3.93	3.53	3.77
		n_o	2.72	2.2	2.46	2.48	2.46
Urbach-tail rule, Eq. (2)		Γ_U (meV)	150	89.6	71.5	75.9	79.6
Interband transition model, Eq. (3)	Direct ($m = 1/2$)	E_g (eV)	2.45	2.44	2.45	2.47	2.47
	Tauc ($m = 2$)	E_g^{opt} (eV)	2.18	2.16	2.23	2.25	2.26

Conclusions

The normal-incidence transmittance $T_{\text{exp}}(\lambda)$ of $0.7 - \mu\text{m}$ thick PbI_2 films deposited on 1.1-mm thick glass slides maintained at different substrate temperatures ($35 - 195$ °C) has been measured at room temperature as a function of the spectral wavelength λ in the UV-VIS-NIR region ($\lambda = 300 - 1100$ nm).

The values of E_g^{opt} and E_g of the studied PbI_2 films, determined from the analysis of the calculated $\alpha(h\nu) - h\nu$ data using the indirect (Tauc) and direct interband transition models, were found to be around 2.2 eV and 2.45 eV, respectively, for all samples regardless of substrate temperatures, while the values of the Urbach-tail parameter Γ_U , deduced from the analysis of the PUMA-retrieved $\alpha(h\nu) - h\nu$ data belonging to the sub-bandgap transition region based on the Urbach exponential law, were found to be around ($70 - 80$ meV) at substrate temperatures $T_s > 100$ °C, below which the values of Γ_U were lower, indicating some band-tailing in the bandgap that has been reduced upon crystallinity improvement. The refractive index $n(\lambda)$ of studied PbI_2 films was found to vary with λ markedly with spectral wavelength nearby the absorption edge of PbI_2 and was well described by the Wemple-DiDomenico formula, the least-square fit curves of which gave comparable static index of refraction $n_o \cong 2.5$ for films prepared at $T_s > 100$ °C. The single-

oscillator energy parameter $E_o \cong 3.9$ eV $\cong 2 E_g^{\text{opt}}$. The Tauc optical bandgap energy results are in good agreement with theoretical predictions. The analysis of the WDD formulation gave nearly the same single-oscillator energy strength E_d (~ 19 eV) for highly crystalline films as for those PbI_2 films prepared at substrate temperatures above 100 °C.

As the stoichiometry of prepared thermally-evaporated lead iodide films was not good, further understanding of the optical response of PbI_2 films and associated energy band structure may be achieved if accurate transmittance/reflectance measurements are made on crystalline PbI_2 films deposited on transparent substrates by other fabrication methods, such as flash-evaporation technique, over a broader spectral range ($300 - 700$ nm). Simulation of the measured transmittance spectra using modified versions of the PUMA program that can handle optical data of thick/thin films and that consider dispersion and optical absorption in their substrates is also appealing. Furthermore, the application of normal-incidence transmission envelope theories to both uniform and non-uniform PbI_2 films prepared by different methods whose optical spectra exhibit many interference-fringe maxima and minima, armed with reliable transmission envelopes, will be complementary.

Acknowledgements

My deepest appreciation goes to Prof. Mousa M. Abdul-Gader Jafar, for his profound insight, continuous support and wise guidance. His

priceless suggestions enhanced the standard of the work considerably.

References

- [1] Moy, J.P., Nucl. Instr. and Meth. A, 442 (2000) 26.
- [2] Hassan, M.A. and Jafar, M.M.A., Nucl. Instr. and Meth. A, 566 (2006) 526.
- [3] Hensch, H.K. and Srinivasagopalan, C., Solid State Communication, 4 (1966) 415.
- [4] Deich, V. and Roth, M., Nucl. Instr. and Meth. A, 380 (1996) 169.
- [5] Lund, J.C., Shah, K.S., Squillante, M.R., Moy, L.P., Sinclair, F. and Entine, G., Nucl. Instr. and Meth. A, 283 (1989) 299.
- [6] Minder, R., Ottaviani, G. and Canali, C., J. Phys. Chem. Solids, 37 (1976) 417.
- [7] Shah, K.S., Street, R.A., Dmitriyev, Y., Bennett, P., Cirignano, L., Klugerman, M., Squillante, M. R. and Entine, G., Nucl. Instr. and Meth. A, 458 (2001) 140.
- [8] Schieber, M., Lund, J.C., Olsen, R.W., McGregor, D.C., Van Scyoc, J.M., James, R.B., Soria, E. and Bauser, E., Nucl. Instr. and Meth. A, 377 (1996) 492.
- [9] Lund, J.C., Olschner, F. and Burger, A., Semiconductors and Semimetals, 43 (1995) 443.
- [10] Ahuja, R., Arwin, H., Ferreira da Silva, A., Persson, C., Osorio-Guillen, J.M., Souza de Almeida, J., Moyses Araujo, C., Veje, E., Veissid, N., An, C.Y., Pepe, I. and Johansson, B., Journal of Applied Physics, 92 (2002) 7219.
- [11] Matuchova, M., Zdansky, K., Zavadil, J., Tonn, J., Jafar, M.M.A-G., Danilewsky, A.N., Cröll, A. and Maixner, J., Journal of Crystal Growth, 312 (2010) 1233.
- [12] Bhavsar, D.S. and Saraf, K.B., J. Mater. Sci.: Mater. Electron., 14 (2003) 195.
- [13] Saleh, M.H., Jafar, M.M.A-G., Bulos, B.N. and Al-Daraghme, T.M.F., Appl. Phys. Res., 6 (2014) 10.
- [14] Swanepoel, R., J. Phys. E: Sci. Instrum., 16 (1983) 1214.
- [15] Saleh, M.H., Ershaidat, N.M., Ahmad, M.J.A., Bulos, B.N. and Jafar, M.M.A-G., Opt. Rev., 24 (2017) 260.
- [16] Jafar, M.M.A-G., European Int. J. Sci. Technol., 2 (2013) 274.
- [17] Jafar M.M.A-G., Saleh, M.H., Ahmed, M.J.A., Bulos, B.N. and Al-Daraghme, T.M., J. Mater. Sci.: Mater. Electron., 27 (2016) 3281.
- [18] Birgin, E.G., Chambouleyron, I. and Martinez, J. Comp. Phys., 151 (1999) 862.
- [19] Mulato, M., Chambouleyron, E.G., Birgin, J.M. and Martínez, Appl. Phys. Lett., 77 (2000) 2133.
- [20] Condeles, J.F., Lofrano, R.C.Z., Rosolen, J.M. and Mulato, M., Brazilian Journal of Physics, 36 (2006) 320.
- [21] Saleh, M.H., Ph.D. Thesis, University of Jordan, (2011), Jordan.
- [22] Shkir, M., Abbas H. and Khan, Z.R., Journal of Physics and Chemistry of Solids, 73 (2012) 1309.
- [23] Ghosh, T., Bandyopadhyay, S., Roy, K.K., Kar, S., Lahiri, A.K., Maiti, A.K. and Goswami, K., Cryst. Res. Technol., 43 (2008) 959.
- [24] Kariper, I.A., Opt. Rev., 23 (2016) 401.
- [25] Jamil, S.S., Mousa, A.M., Mohammad, M.A. and Thajeel, K.M., Eng. & Tech. Journal, 29 (2011) 531.
- [26] Acuna, D., Krishnan, B., Shaji, S., Sepulveda, S. and Menchaca, J.L., Bull. Mater. Sci., 39 (2016) 1453.
- [27] Kumar, S. and Sharma, S., International Journal of Engineering Research & Technology, 2 (2013) 3593.

- [28] Agrawal, H., Vedeshwar, A.G. and Saraswat, V.K., *Journal of Nano Research*, 24 (2013) 1.
- [29] Bhavsar, D.S., *Advances in Applied Science Research*, 2 (2011) 92.
- [30] Shehadeh, K.M., M.Sc. Thesis, The University of Jordan, (2017), Jordan.
- [31] Al-Daraghme, T.M., Saleh, M.H., Ahmad, M.J.A., Bulos, B.N., Shehadeh, K.M. and Jafar, M.M.A-G., *Journal of Electronic Materials*, 47 (2018) 1806.
- [32] Schieber, M., Zamoshchik, N., Khakhan, O. and Zuck, A., *Journal of Crystal Growth*, 310 (2008) 3168.
- [33] Dmitriev, Y., Bennett, R.B., Cirignano, L.J., Klugerman, M. and Shah, K.S., *Nucl. Instr. and Meth. A*, 592 (2008) 334.
- [34] Studenyak, I., Kranjčec, M. and Kurik, M., *International Journal of Optics and Applications*, 4 (3) (2014) 76.
- [35] O'Leary, S.K., Johnson, S.R. and Lim, P.K., *J. Appl. Phys.*, 82 (1997) 3334.
- [36] Tan, W.C., Koughia, K., Singh, J. and Kasap, S.O., "Optical Properties of Condensed Matter and Applications", Ed. J. Singh, (John Wiley, London, 2006), Chapter 1.
- [37] Tauc, J., "Optical Properties of Solids", Ed. F. Abelés (North-Holland, Amsterdam, 1972), pp. 277-310.
- [38] Dragoman, D. and Dragoman, M., "Optical Characterization of Solids", (Springer-Verlag, Berlin, 2002).
- [39] Mott, N.F. and Davis, E.A., "Electronic Processes in Non-Crystalline Materials", 2nd Ed. (Clarendon Press, Oxford, 1979).
- [40] Wemple, S.H. and DiDomenico, M., *Phys. Rev. B*, 3 (1971) 1338.

Radiological Risk Measurements Due to Natural Radioactivity of Building Stones Used in Jordanian Houses

H. Saleh^a, M. Hamideen^b, M. Al-Hwaiti^c and S. Al-Kharoof^d

^a Department of Radiography, Al-Hussein Bin Talal University, Ma'an, Jordan.

^b Department of Physics, Faculty of Engineering Technology, Al-Balqa Applied University, Amman, Jordan.

^c Department of Environmental Engineering, Al-Hussein Bin Talal University, Ma'an, Jordan.

^d Supreme Council of the Environment's Radiation Affairs, Bahrain.

Received on: 17/5/2018;

Accepted on: 18/9/2018

Abstract: The radiological risk from building stone interfaces in Jordanian houses was determined depending on gamma ray spectrometric techniques. Building stone samples collected from seven types mostly used in Jordanian houses have been analyzed for the naturally occurring radioactive radionuclides. The mean specific activities of ²³⁸U, ²³²Th and ⁴⁰K were lower than 7.63±0.08, 2.77±0.12, 32.7±2.96 Bq/kg, respectively. The estimated radium equivalent activity (Ra_{eq}) in the stones was lower than 24.84±0.470 Bq/kg and the external and indoor hazard indices were also lower than unity. Moreover, different radiological hazardous parameters (the absorbed dose, the annual effective dose equivalent, the annual gonadal dose equivalent (AGDE), Excess Lifetime Cancer Risk ELCR and activity utilization index (AUI)) were calculated. The results were lower than those of published world average values. Also, the obtained values were comparable with the reported data of other building materials used in Jordan.

Keywords: Natural radioactivity, Gamma-ray spectrometry, Building stones, Hazard indices, Activity utilization index, Radiological risk.

Introduction

The effects of radiation sources on the world's population can be divided into natural and man-made effects, with dominant natural contribution from terrestrial and cosmic origins [1]. Natural radioactivity in building materials can be a main source of indoor radiation, either external or internal [2]. The former is caused by direct exposure to gamma radiation, while the latter is caused by inhalation of radon present in building materials. According to the World Health Organization, WHO, there is an association between indoor radon exposure and lung cancer, even at the relatively low concentration levels found in residential

buildings [3]. For this reason, there is a growing need of controlling the use of materials derived from soils, such as phosphogypsum, cement, ceramic, granite or stones, in dwelling decoration, which cause an additional source of radiation exposure to people.

Many researchers found that natural radioactive nuclides, such as uranium (²³⁸U), thorium (²³²Th) and the radioactive isotope of potassium (⁴⁰K) in building materials originating from rocks and soils, have low-concentration amounts. A huge number of studies interested in the natural radioactivity of construction materials and those produced from industrial waste in

different countries around the world are presented in literature, such as [4, 5, 6, 7, 8, 9], but none of them was concerned with building stones.

In Jordan, as in all other countries, there is a great interest in using various materials of rock origin as building materials. Most dwellings are being decorated from outside and inside with building materials. Recently, most buildings in all Jordanian governorates use building stones due to their rigidity and proper appearance despite of their type and source of origin in different locations in Jordan.

In view of this, there is a great need to measure the radionuclide concentrations in building materials to limit the health hazards and protect humans from environmental pollution.

Several studies have been made on the measurement of radon and natural radioactivity of the most common materials used in building construction in Jordan. Sharaf and Hamideen (2013) [10] measured the specific radioactivity of different materials used in Jordanian buildings. Also, Matiullah and Hussein (1998) [11] were engaged in the measurement of natural radioactivity of a large number of building materials of natural source and that of industrial sources used in the populated sites of Jordan. Meanwhile, Al-Jundi et al. (2009) [12] presented the indoor dose rates for a typical Jordanian concrete room, using Monte Carlo method. But, there is still a lack of regulations on the radioactivity of building materials for their safe usage.

This study was carried out to measure the ^{226}Ra , ^{238}U , ^{232}Th and ^{40}K specific activities in seven main stones used in Jordanian houses, to compare them to the world average values for soil and to check that using these stones with other building materials does not surpass the limits of the allowed population exposure to radiation. For this purpose, collected samples from different types have been analyzed for natural radionuclides using gamma spectrometry. Also, the average radium equivalent activity, the external and indoor hazard indices, the total absorbed dose rate, the annual dose equivalent, the annual gonadal dose equivalent, Excess Lifetime Cancer Risk ELCR and activity utilization index (AUI) have been calculated in order to provide background database on the natural radioactivity levels and environmental pollution.

Materials and Methods

The stone samples were collected from seven types; namely, Ajlun, Ma'an, Basalt, Desert, Travenia, Hayan and Samic stones that are mostly used in Jordanian house interfaces. Ten samples from each type were collected, crushed, dried up in an oven at 130°C for 10 hours to avoid any moisture, pulverized to a fine powder and mixed to prepare homogenized representative samples for measurement. The powder samples were compressed in plastic taps 1.6 cm high and 7.8 cm in diameter, sealed to avoid any radon volatilization and weighed, then put away to reach radioactive equilibrium. After that, gamma analysis was performed. Sample preparation and radioactivity measurements were made in the Jordanian Atomic Energy Commission (JAEC) laboratories.

Gamma Spectrometry measurements to obtain the ^{226}Ra , ^{238}U , ^{232}Th and ^{40}K specific activities were made using a high purity germanium (HPGe) detector (co-axial type) that was described in detail in a previous study [13]. The energy calibration and relative efficiency determination were carried out using a mixed source. The counting time for each sample and background was 60,000 s.

Activity Concentration Calculations

The natural radioactivity of the samples was determined using the count rate of each photopeak of the radionuclides ^{226}Ra , ^{238}U , ^{232}Th and ^{40}K in the spectra detected by gamma spectroscopy. ^{226}Ra specific activity was calculated in the samples using the peak of energy 186.3keV, ^{238}U series by 351.9 keV peak of ^{214}Pb and 609.3 keV peak of ^{214}Bi , ^{232}Th series by 911.0 keV peak of ^{228}Ac and 583.3 keV peak of ^{208}Tl and the 1460 keV gamma-ray transition was used to determine the concentration of ^{40}K .

An accurate specific activity A_{Ei} (in Bq/kg), of a nuclide i for a peak at energy E , is given by the relation [14]:

$$A_{Ei} = \frac{N_{Ei}}{\epsilon_E \times t \times f \times m_s} \quad (1)$$

where N_{Ei} is the net peak count inside a peak at energy E , ϵ_E is the detection efficiency at energy E , t is the counting live-time, f is the gamma ray yield per disintegration of the specific nuclide for a transition at energy E and m_s is the mass in kg of the measured sample. The peak activity

was averaged if there were more than one peak in the energy range of analysis and the result was the weighted average nuclide activity.

In order to prevent unnecessary exposure, radium equivalent activity (Ra_{eq}) and external hazard index (H_{ex}) were used to estimate radiation hazards. Radium equivalent activity (Ra_{eq}) was calculated using relation (2) assuming that 370 Bq/kg of ^{226}Ra , 259 Bq/kg of ^{232}Th and 4810 Bq/kg of ^{40}K produce the same gamma ray dose rate [1].

$$Ra_{eq} (Bq / kg) = \left. \begin{aligned} &A_{226Ra} + 1.43A_{232Th} + 0.077A_{40K} \end{aligned} \right\} \quad (2)$$

A_{226Ra} , A_{232Th} , A_{40K} are the specific activities of ^{226}Ra , ^{232}Th and ^{40}K , respectively.

Based on the above assumption of activity world average values, the accepted radium equivalent activity (Ra_{eq}) world average value is better to be lower than 370 Bq/kg [15].

Radiological Risk Estimations

Krieger (1981) proposed a model for calculating the external hazard index, H_{ex} , assuming thick wall without any windows or doors, the external hazard index is given by the following relation [1]:

$$H_{ex} = \left. \begin{aligned} &(A_{226Ra} / 370) \\ &+ (A_{232Th} / 259) + (A_{40K} / 4810) \end{aligned} \right\} \quad (3)$$

where A_{226Ra} , A_{232Th} , A_{40K} are the specific activities of ^{226}Ra , ^{232}Th and ^{40}K , respectively.

The risk from ^{222}Ra and its decay daughters to the internal respiratory systems is described by indoor hazard index, H_{in} , which must be less than 1.0 for safety requirements. In literature, a number of indices were suggested by researchers for indoor exposures as given in relations (4-7) [15, 16]:

$$H_1 = \left. \begin{aligned} &(A_{226Ra} / 185) \\ &+ (A_{232Th} / 259) + (A_{40K} / 4810) \end{aligned} \right\} \quad (4)$$

$$H_2 = \left. \begin{aligned} &(A_{226Ra} / 150) \\ &+ (A_{232Th} / 259) + (A_{40K} / 4810) \end{aligned} \right\} \quad (5)$$

$$H_3 = \left. \begin{aligned} &(A_{226Ra} / 1000) \\ &+ (A_{232Th} / 700) + (A_{40K} / 10000) \end{aligned} \right\} \quad (6)$$

$$H_4 = \left. \begin{aligned} &(A_{226Ra} / 300) \\ &+ (A_{232Th} / 200) + (A_{40K} / 3000) \end{aligned} \right\} \quad (7)$$

Also, A_{226Ra} , A_{232Th} , A_{40K} are the specific activities of ^{226}Ra , ^{232}Th and ^{40}K , respectively.

In order to calculate the radiological effects of any building material containing radionuclides, the absorbed dose rate D (nGy/h) in outdoor air at 1m above the ground surface in terms of ^{238}U , ^{232}Th and ^{40}K specific activities was calculated using the relation [17]:

$$D (nGy / h) = \left. \begin{aligned} &0.427A_{238U} + 0.662A_{232Th} + 0.0432A_{40K} \end{aligned} \right\} \quad (8)$$

A_{238U} , A_{232Th} , A_{40K} are the specific activities of ^{238}U , ^{232}Th and ^{40}K , respectively.

The annual absorbed dose equivalent received by people can be estimated using the value of 0.7Sv/Gy as a conversion factor and 0.2 of the day for the occupancy factor [1]. The annual effective dose was calculated using the relation:

$$E (\mu\text{Sv} / y) = D (n\text{Gy} / h) \times 24h \times \left. \begin{aligned} &365.25d \times 0.2 \times 0.7\text{Sv} / \text{Gy} \times 10^{-3} \end{aligned} \right\} \quad (9)$$

UNSCEAR (1988) considered the active bone marrow, the bone surface cells and the gonads, in addition to lung, breast and thyroid, as the organs of interest when humans work with radiation. One of the dosimetry models found in literature to evaluate the annual gonadal dose equivalent (AGDE) for a residential house considered as a cavity with infinitely thick walls built with a material of specific activities of radium, thorium and potassium is described by the relation [18,19]:

$$AGDE (\mu\text{Sv} / y) = \left. \begin{aligned} &3.09A_{226Ra} + 4.18A_{232Th} + 0.314A_{40K} \end{aligned} \right\} \quad (10)$$

where A_{226Ra} , A_{232Th} , A_{40K} are the specific activities of ^{226}Ra , ^{232}Th and ^{40}K , respectively. For a house containing the world average activity values of ^{226}Ra , ^{232}Th and ^{40}K in soil (35,

30 and 400 Bq/kg, respectively), it will produce an AGDE of 359.15 $\mu\text{Sv/y}$.

The excess lifetime cancer risk (ELCR) is another important radiological factor that is estimated as a consequence upon the evaluation of AEDE using the equation [20, 21]:

$$ELCR = E \times DL \times RF \quad (11)$$

where E , DL and RF are the annual effective dose equivalent, duration of life (70 years) and risk factor (0.05 Sv^{-1}), respectively. ICRP (2007) [20] defined the risk factor as fatal cancer risk per Sievert, which is assigned to a value of 0.05 for the public for stochastic effects [21].

The dose rates in indoor air according to the concentrations of different combinations of the three primordial radionuclides in soil samples used in construction materials are expressed by the activity utilization index (AUI). AUI is calculated from the following equation [22]:

$$AUI = \left[\begin{aligned} & \left(A_{226\text{Ra}} / 50 \right) f_u + \left(A_{232\text{Th}} / 50 \right) f_{Th} \\ & + \left(A_{40\text{K}} / 500 \right) f_K \end{aligned} \right] w_m \quad (12)$$

where A_{Ra} , A_{Th} and A_{K} are the activity concentrations of ^{226}Ra , ^{232}Th and ^{40}K , respectively and f_K (0.041), f_{Th} (0.604) and f_U (0.462) are the respective fractional contributions from the actual activities of these radionuclides to the total gamma radiation dose rate in air. w_m is a weighted factor for mass proportion of the building materials in the dwelling with the characteristic activity. Applying the appropriate conversion factor ($w_m=1$) along with the activity concentrations of the respective radionuclides implies that all building materials used in a house are composed of this specific material. Typical activities per unit mass of ^{40}K , ^{232}Th and ^{226}Ra in soils A_{K} , A_{Th}

and A_{Ra} are reported to be 500, 50 and 50 Bq/kg, respectively [23], which gives a full utilization (AUI) of 0.5634.

Results and Discussion

The specific activities of ^{226}Ra , ^{238}U , ^{232}Th and ^{40}K in the collected stone samples are listed in Table.1. The results show very low values and most of them were under the minimum detection limits of the detector. Ajlun stones were characterized by the highest activity concentrations for all measured ^{226}Ra , ^{232}Th and ^{40}K radionuclides. ^{226}Ra specific activities were under 17.5 Bq/kg in almost all of the sample types, except in Ajlun stones, where the specific activity was 23.5 ± 2.9 Bq/kg. ^{238}U specific activity ranged from 7.0 Bq/kg in five types to 10.6 ± 1.9 Bq/kg in Ma'an stones. Meanwhile, the specific activity of ^{232}Th ranged from 1.4 Bq/kg in four types to 6.3 ± 0.4 Bq/kg in Basalt stones and ^{40}K specific activity ranged from 12.5 Bq/kg in five types to 147.5 ± 6.2 Bq/kg in Ajlun stones. The geological locations and the geochemical characteristics of the parent rocks from which the stones were collected explain the small variation in these natural radioactivity levels [24].

The average activities of ^{226}Ra , ^{238}U , ^{232}Th and ^{40}K were found to be lower than 18.36, 7.63, 2.77 and 32.7Bq/kg, respectively. And the world average specific activities of the radionuclides ^{226}Ra , ^{238}U , ^{232}Th and ^{40}K in all soil samples have averages of 35, 35, 30 and 400 Bq/kg, respectively [1]. Fig.1 shows the variation of ^{226}Ra , ^{238}U , ^{232}Th and ^{40}K specific activities in different stone types. The radionuclides ^{226}Ra , ^{238}U and ^{232}Th show a uniform distribution that is lower than the accepted world average values. Meanwhile, ^{40}K shows an abnormal distribution in Ajlun stones depending on the geological structure of the original rocks.

TABLE 1. Natural radioactivity in Ajlun, Ma'an, Basalt, Desert, Travenia, Hayan and Samic stone types (in Bq/kg) using gamma spectrometry.

Stone Type	^{226}Ra	^{238}U	^{232}Th	^{40}K
Ajlun	23.5 ± 2.9	7.8 ± 2.4	5.0 ± 0.4	147.5 ± 6.2
Ma'an	< 17.5	10.6 ± 1.9	< 1.4	< 12.5
Basalt	< 17.5	< 7.0	6.3 ± 0.4	18.9 ± 6.8
Desert	< 17.5	< 7.0	2.5 ± 0.5	< 12.5
Travenia	< 17.5	< 7.0	< 1.4	< 12.5
Hayan	< 17.5	< 7.0	< 1.4	< 12.5
Samic	< 17.5	< 7.0	< 1.4	< 12.5
Mean	< 18.36 ± 0.13	< 7.63 ± 0.08	< 2.77 ± 0.12	< 32.7 ± 2.96

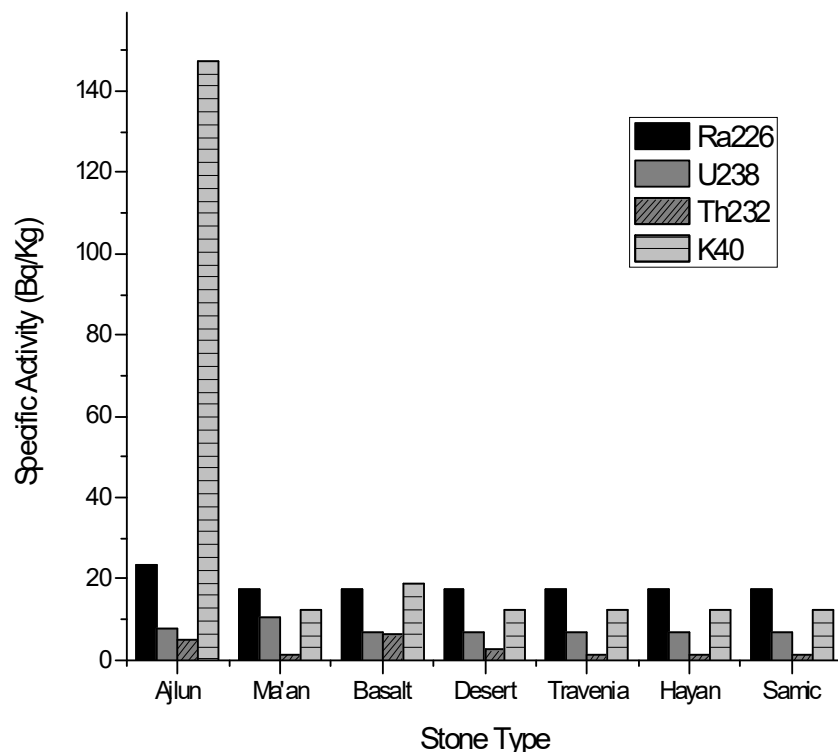


FIG. 1. Variation of ^{226}Ra , ^{238}U , ^{232}Th and ^{40}K specific activities in Ajlun, Ma'an, Basalt, Desert, Travenia, Hayan and Samic stone types.

All calculated values of radium equivalent Ra_{eq} (Bq/kg), external hazard index (H_{ex}) and indoor hazard indices (H_1 , H_2 , H_3 , H_4) of Ajlun, Ma'an, Basalt, Desert, Travenia, Hayan and Samic stone types were tabulated in Table.2. The calculated Ra_{eq} results ranged from 20.46 Bq/kg in three types to 42.01 Bq/kg in Ajlun stones and the average value was less than (24.84 ± 0.470) Bq/kg which is lower than the recommended maximum value of 370 Bq/kg [15]. The estimated external hazard indices in the samples were 0.06 in four of the seven types and the maximum value was 0.11 with an average value for all types of 0.07 ± 0.001 , which is much lower than the safety recommended limit of unity. Also, the internal hazard indices show the same behavior, since their entire calculated values were very low relative to unity [1].

Table 3 presents all calculated values of absorbed dose rate D in air, annual effective dose equivalent E , annual gonadal dose equivalent AGDE, Excess Lifetime Cancer Risk ELCR and activity utilization index (AUI) in Ajlun, Ma'an, Basalt, Desert, Travenia, Hayan and Samic stone

types. The mean values of the calculated absorbed dose rate D in air, annual effective dose equivalent E and annual gonadal dose equivalent AGDE were (6.50 ± 0.18) nGy/h, (7.98 ± 0.22) $\mu\text{Sv/y}$ and (78.57 ± 1.65) $\mu\text{Sv/y}$, respectively. A general overview of the previous results indicates that all of the calculated parameters have average values below the safety limits recommended of 57 nGy/h, 70 $\mu\text{Sv/y}$ and 359.15 $\mu\text{Sv/y}$ for the previous parameters, respectively [1]. Also, the estimated value of Excess Lifetime Cancer Risk ELCR ranged from 19.14×10^{-6} to 55.89×10^{-6} with a mean value of 27.94×10^{-6} , which is below the world average value of 290×10^{-6} for soils [1]. This means that the excess risk of cancer among the population living inside these decorated houses due to using the building stones is insignificant. Finally, the activity utilization index (AUI) values ranged from 0.16 to 0.24 with a mean value of 0.18. This means that even for full utilization of the stones in building; i.e., $w_m = 1$, the associated AUI was much lower than the recommended limit of 0.5634.

TABLE 2. Radium equivalent Ra_{eq} , external hazard index (H_{ex}) and indoor hazard indices (H_1 , H_2 , H_3 , H_4) in Ajlun, Ma'an, Basalt, Desert, Travenia, Hayan and Samic stone types.

Stone Type	$Ra_{eq}(Bq/kg)$	H_{ex}	H_1	H_2	H_3	H_4
Ajlun	42.01	0.11	0.177	0.207	< 0.045	< 0.153
Ma'an	< 20.46	< 0.06	< 0.103	< 0.125	< 0.021	< 0.069
Basalt	< 27.96	< 0.08	< 0.123	< 0.145	< 0.028	< 0.096
Desert	< 22.04	< 0.06	< 0.107	< 0.129	< 0.022	< 0.075
Travenia	< 20.46	< 0.06	< 0.103	< 0.125	< 0.021	< 0.069
Hayan	< 20.46	< 0.06	< 0.103	< 0.125	< 0.021	< 0.069
Samic	< 20.46	< 0.06	< 0.103	< 0.125	< 0.021	< 0.069
Mean	<24.84±0.470	<0.07±0.001	<0.12±0.002	<0.14±0.002	<0.026±0.001	<0.086±0.001

TABLE 3. Absorbed dose rate D in air, annual effective dose equivalent E , annual gonadal dose equivalent AGDE, Excess Lifetime Cancer Risk ELCR and activity utilization index (AUI) in Ajlun, Ma'an, Basalt, Desert, Travenia, Hayan and Samic stone types.

Stone Type	$D(nGy/h)$	$E(\mu Sv/y)$	AGDE($\mu Sv/y$)	ELCR ($\times 10^{-6}$)	AUI
Ajlun	13.01	15.97	139.83	55.89	0.24
Ma'an	< 5.99	< 7.35	< 63.85	< 25.74	< 0.16
Basalt	< 7.98	< 9.79	< 86.34	< 34.26	< 0.17
Desert	< 5.18	< 6.36	< 68.45	< 22.27	< 0.17
Travenia	< 4.46	< 5.47	< 63.85	< 19.14	< 0.16
Hayan	< 4.46	< 5.47	< 63.85	< 19.14	< 0.16
Samic	< 4.46	< 5.47	< 63.85	< 19.14	< 0.16
Mean	< 6.50±0.18	< 7.98±0.22	< 78.57±1.65	< 27.94±5.09	< 0.18±0.01

In literature, Matiullah et al. [11] found that the radium equivalent activity of Ajloun stones was 109.4 Bq/kg and of Ma'an stones was 88.1Bq/kg. Meanwhile, Al-Jundi et al. [25] estimated the radium equivalent activity of Desert stone to be 70.7Bq/kg, Halabat stones 53.2 Bq/kg and Ajloun stones 64.7 Bq/kg. A comparison between the calculated radium equivalents with other building constructions

used in Jordanian buildings is given in Fig.2. It is shown that Ra_{eq} due to the building stones was lower than the measured values of 123.20, 117.90, 86.22 and 54.96 Bq/kg for fine aggregates, coarse aggregates, sand and marble, respectively [25]. Also, it is lower than the average value of 79.9 Bq/kg measured for the general Jordanian building materials [11].

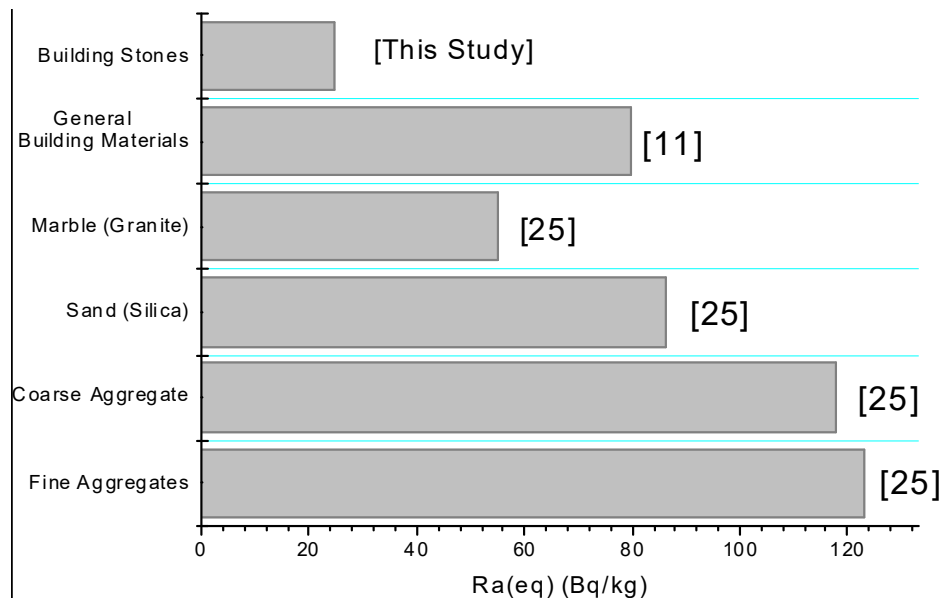


FIG. 2. Comparison of radium equivalent Ra_{eq} in the stone types with other materials used in Jordanian buildings.

Conclusion

Seven kinds of building stones used in Jordanian building constructions, considered as the most popular ones used, were measured for their natural radioactivity in order to determine their radiological impact when they are used as building materials. The specific activities of ^{226}Ra , ^{238}U , ^{232}Th and ^{40}K activity levels in the stone samples were lower than the world average values and the corresponding values in other construction materials used in Jordanian buildings. The corresponding external hazard index, indoor hazard indices, absorbed dose rate in air, annual effective dose equivalent, gonadal dose equivalent, Excess Lifetime Cancer Risk ELCR and activity utilization index (AUI) don't

exceed significantly the average dose limit for all stone types. The results obtained indicate no significant radiological hazards arising from using such stones in decoration of building interfaces, since the health effects due to natural radiation are very low.

Acknowledgement

The authors gratefully acknowledge the general administration of Jordan Atomic Energy Commission for their permission to use their laboratories, the (JAEC) staff for their assistance and the technical support given in physical sample preparation and spectral analysis.

References

- [1] UNSCEAR. United Nations Scientific Committee on the Effect of Atomic Radiation Sources ; Effects and Risk of Ionizing Radiation, United Nations, New York (2000).
- [2] Gandolfo, G., Lepore, L., Peperosa, A., Remetti, R. and Franci, D., Energy Procedia, 140 (2017) 13.
- [3] World Health Organization, WHO Handbook on Indoor Radon: A Public Health Perspective, Geneva (2009).
- [4] Popovic, D. and Todorovic, D., Phys. Chem. and Tech., 4 (2006) 11.
- [5] Kam, E. and Bozkurt, A., Appl. Radiat. and Iso., 65 (2007) 440.
- [6] Papaefthymiou, H. and Gouseti, O., Radiation Measurements, 43(8) (2008) 1453.
- [7] Ravisankar, R., Vanasundari, K., Chandrasekaran, A., Rajalakshmi, A. and Meenakshisundaram, V., Appl. Radiat. and Iso. 70(4) (2012) 699.
- [8] Zaidi, J.H., Arif, M., Ahmad, S., Fatima, I. and Qureshi, I.H., Appl. Radiat. and Iso., 51 (1999) 559.
- [9] Dabayneh, K.M., H.U.R.J., 3 (2008) 49.
- [10] Sharaf, J.M. and Hamideen, M.S., Appl. Radiat. and Iso., 80 (2013) 61.
- [11] Matiullah, N.A. and Hussein, A., J. Environ. Radioact., 39 (1998) 9.
- [12] Al-Jundi, J., Ulanovsky, A. and Pröhl, G., J. Environ. Radioact., 100 (10) (2009) 841.
- [13] Saleh, H. and Abu Shayeb, M., Ann. of Nucl. Energy, 65 (2014) 184.
- [14] GammaVision-32: Gamma-Ray Spectrum Analysis and MCA Emulator. Software User's Manual. Vol. 5.1, EG&G ORTEC (1999).
- [15] Beretka, J. and Mathew, P.J., Health Phys., 48 (1985) 87.
- [16] Quindos, L.S., Fernandez, P.L. and Soto, J., "Building materials as source of exposure in houses". In: Seifert, B. and Esdorn, H. (Eds.), Indoor Air 1987, Vol. 2. Institute for Water, (Soil and Air Hygiene, Berlin, 1987), 365.
- [17] UNSCEAR, Report to the General Assembly, with Scientific Annexes. New York. United Nations Publication E.94.IX.2, (1993).
- [18] UNSCEAR, Sources, effects and risk of ionization radiation. (1988).
- [19] Kurnaz, A., Kucukomeroglu, B., Keser, R., Okumusoglu, N.T., Korkmaz, F., Karahan, G. and Cevik, U., Appl. Rad. And Isot., 65 (2007) 1281.
- [20] ICRP, ICRP Publication 103, 37(2-4) (2007).
- [21] Taskin, H., Karavus, M., Ay, P., Topuzoglu, A., Hidiroglu, S. and Karahan, G., J. Environ. Radioact., 100 (1) (2009) 49.
- [22] Ramasamy, V., Suresh, G., Meenakshisundaram, V. and Ponnusamy, V., Appl. Radiat. and Isot., 69(1) (2011) 184.

- [23] NEA-OECD. Exposure to radiation from natural radioactivity in building materials. Report by NEA Group of Experts. OECD, Paris (1979).
- [24] Xinwei, L., Shigang, C. and Fang, Y. Radiat. Phys. and Chem., 99 (2014) 62.
- [25] Al-Jundi, J., Salah, W., Bawa'aneh, M. and Afaneh, F., Radiat. Protect. Dosim., 118 (1) (2006) 93.

Optical Properties of Chemically Synthesized Cadmium Sulphide for Solar Cell Applications

M. A. SALAWU^a, A. B. ALABI^b, S. B. SHARAF^c and T. AKOMOLAFE^b

^a *Physics/Electronics Unit, P.M.B. 1371, Kwara State Polytechnic, Ilorin, Nigeria.*

^b *Department of Physics, University of Ilorin, Ilorin, Nigeria.*

^c *Department of Physics, Usmanu Danfodiyo University Sokoto, Nigeria.*

Received on: 21/9/2017;

Accepted on: 27/12/2017

Abstract: This paper presents the optical properties of chemically synthesized cadmium sulphide for solar cell applications. CdS nano-particles were synthesized with chemical route method using cadmium sulphate as cadmium ion source and thiourea as sulphide ion source. The prepared CdS nano-particles were characterized with XRD and SEM. Then, the prepared CdS was deposited on well cleaned glass substrate by thermal evaporation technique to obtain a film of 100 nm thickness. The film was optically characterized with UV-Visible spectrophotometer and FTIR Spectrometer. The peaks at 43° and 52° indicate that the nano-particles contain a mixture of hexagonal (wurtzite) and cubic (zincblende) structures which confirmed the greenockite and the Hawleyite phases of CdS. The optical analyses showed high optical transmittance of 90 % at 658 nm, reflectance of 47.76 % at 488 nm and the absorbance of 0.165 A.U. at 400 nm wavelength. The optical energy band gap of 2.42 eV was also deduced for the film from Tauc's plot. The Fourier Transform Infrared Radiation (FTIR) showed different peaks that indicate the stretching and vibrations of O-H, CH₃, C-O and C-H of CdS against their respective wave numbers. The prepared CdS can be employed as a window layer for the fabrication of CdS/CdTe thin film solar cells.

Keywords: SEM, XRD, CdS, UV-visible spectrophotometer.

PACS: 42, 81.

Introduction

Among various nano-particles, a great interest has been shown towards cadmium sulphide (CdS) nano-particles because of availability of discrete energy levels, size-dependent optical properties, tunable bandgap, a well-developed synthetic protocol and easy preparation technique with good chemical stability [1]. CdS nano-particles are categorized under the group chalcogenides and are a II-VI group of semiconductor nano-particles which shows size-dependent optical and electrical properties due to its high surface area to volume ratio and quantum confinement [2]. Due to its very high photosensitivity, CdS has usage in detection of visible radiations, in light emitting diodes, solar cells, photochemical catalysis, gas

sensors, various luminescence devices, optoelectronic devices and a range of biological application [3-6]. Cadmium sulphide (CdS) semiconductor is an excellent visible light detector among other semiconductors [7]. It is an *n*-type direct band gap semiconductor ($E_g = 2.42$ eV) which has been studied extensively because of its band gap, high absorption coefficient, reasonable conversion efficiency, good stability and low cost [8].

Cadmium sulphide (CdS) nano-particles have been synthesized by several researchers using chemical precipitation methods [9-14] and cubic hexagonal phase was identified with different grain sizes ranging from 7 to 16 nm [10-11] for the nano-particles and the films. Deposition of

CdS nano-particles has been carried out by Chemical Bath Deposition technique [15-17] and Spray Pyrolysis technique [6], among others, to obtain thin film nanostructures with different morphologies, such as acicular-like, mesoporous, spherical shapes, and crystallite sizes varying from 11 to 16 nm had also been reported [11].

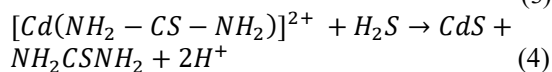
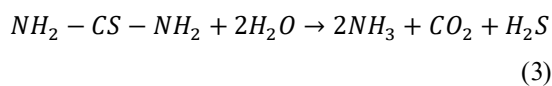
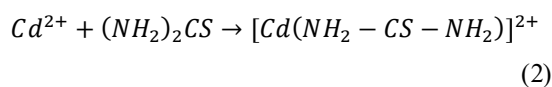
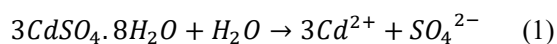
The synthesis and characterization of cadmium sulphide *via* different techniques have attracted considerable attention due to its potential applications. Nanometer-sized semiconductors exhibit structural, electronic, optical, luminescence and photo conducting properties very different from their bulk properties [13].

This paper investigates the optical properties of 100 nm CdS thin film from chemically synthesized CdS nano-particles deposited by thermal evaporation technique. This technique has the possibility of obtaining uniform and quality films with good adherence without inclusion of impurities. The percentage transmittance, reflectance and absorbance characteristics of this film shall be investigated for window layer in the fabrication of efficient CdS/CdTe thin film solar cells.

Materials and Methods

A. Synthesis of Cadmium Sulphide

- i. 0.05 M of cadmium sulphate (CdSO_4) was used as a Cd^{2+} ion source and 0.10 M of thiourea as the S^{2-} ion source at a working solution of temperature $70 \pm 5^\circ\text{C}$.
- ii. Ammonia solution was used to adjust the pH of the reaction mixture as a complexing agent. The variation of pH during the growth is important in the structural film quality.
- iii. The reaction mechanism involved in the formation process of CdS nano-particles can be formulated as follows:



B. Deposition and Characterization of CdS Film

The prepared CdS nano-particles were characterized with X-Ray Diffractometer (XRD) and Scanning Electron Microscope (SEM). The prepared CdS nano-particles were evaporated from molybdenum boat and deposited on clean glass substrate as thin films form. The glass substrate was cleaned with detergent, acetone and methanol and washed in an ultrasonic bath with de-ionized water and then dried in a dust-free atmosphere. CdS thin film of 100 nm was ensured on the glass substrate with thermal evaporation technique, in a residual pressure of 10^{-5} torr. The substrate temperature was kept fixed at room temperature. Thermal evaporation uses an electric resistance heater to melt the material and raise its vapour pressure to a useful range. This is done in a high vacuum to allow the vapour to reach the substrate without reacting with or scattering against other gas-phase atoms in the chamber, as well as to reduce the incorporation of impurities from the residual gas in the vacuum chamber. The vacuum is required to allow the molecules to evaporate freely in the chamber and subsequently condense on the surface of the glass substrate. The film was optically characterized with UV-visible spectrophotometer and Fourier Transform Infrared (FTIR) spectrometer. The photometric measurements were carried out using UV-visible spectrophotometer to measure percentage reflectance and transmittance. Beer's Lambert law was also employed to obtain the absorbance of the CdS film. The FTIR spectrometer was employed to determine the functional group of the material under study.

Results and Discussion

The XRD pattern of the synthesized CdS nano-particles is shown in Fig. 1. The identification and assignment of the observed diffraction patterns were carried out using the JCPDS 41-1049 Hexagonal (H) and JCPDS 10-0454 Cubic (C) reference patterns (Pantoja, 2013). The peak (101) appears at approximately 29° , indicating that the phase is hexagonal or at least a mixture of hexagonal and cubic phases. The peaks at 43° and 52° indicate that the films contain a mixture of hexagonal (wurtzite) and cubic (zincblende) structures, which confirmed the greenockite and the Hawleyite phases, respectively.

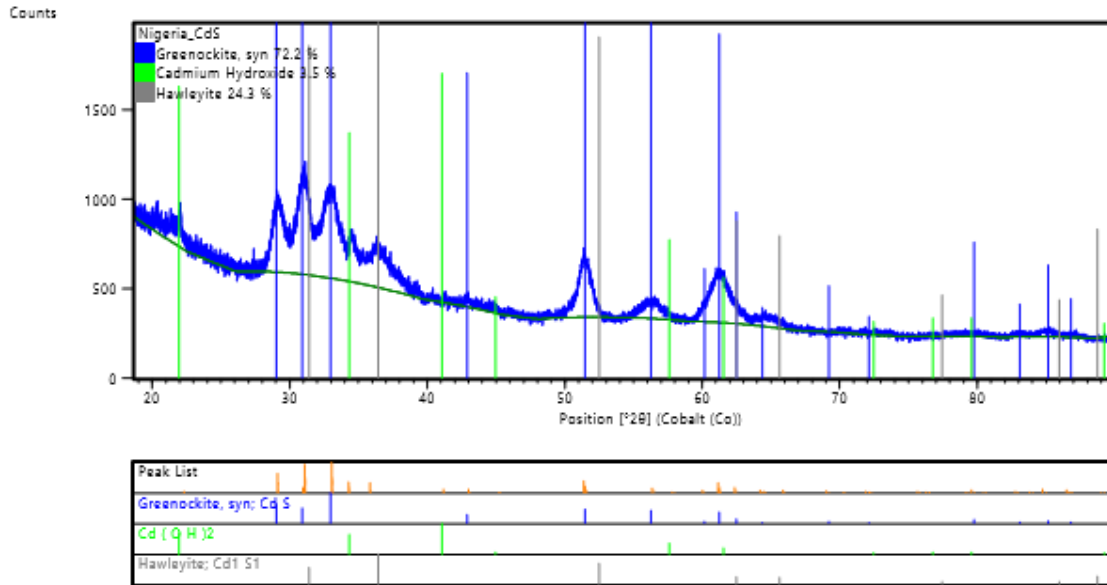


FIG. 1. XRD analysis of the synthesized CdS nano-particles.

The Scanning Electron Microscope (SEM) photograph of the synthesized CdS nano-particles is shown in Fig. 2. The result display, some percentages of oxygen content in the

particles which may be due to the presence of cracks or rather the cracks are a result of the oxidation occurring within the sample.

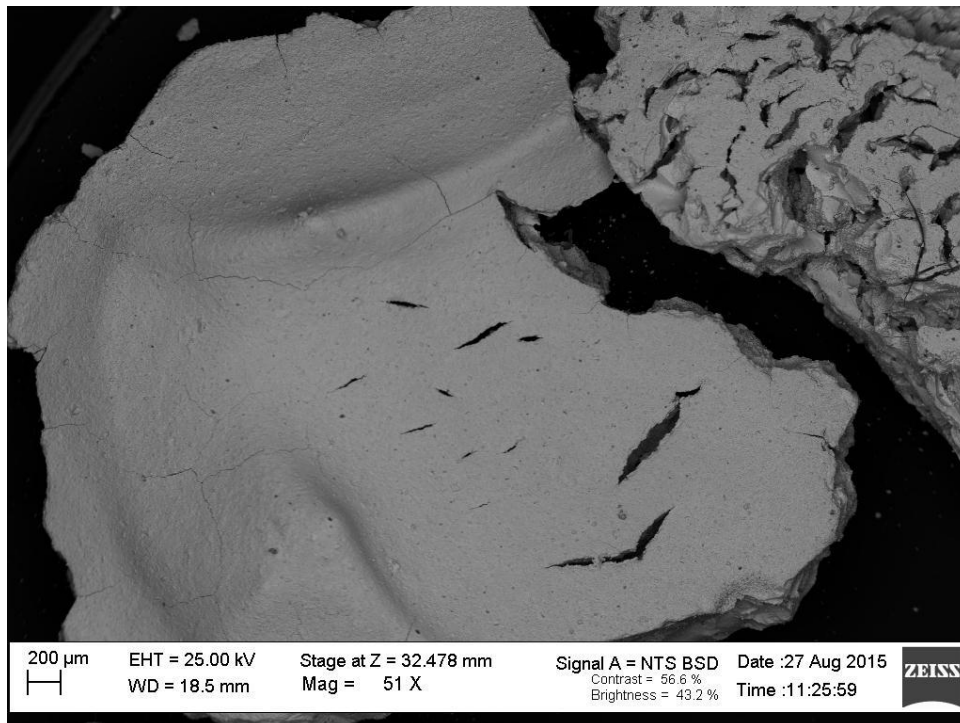


FIG. 2. SEM photographs of the synthesized CdS nano-particles.

Energy Dispersive (EDX) analysis of the chemically synthesized CdS nano-particles is shown in Table 1. The analytical errors of the

chemically synthesized CdS were reasonably low.

TABLE 1. The elements' normalized weight percents of the prepared CdS nano-particles.

Element	Normalized [wt. %]
Oxygen	10.58
Silicon	0.9
Cadmium	74.66
Sulfur	13.65
Aluminum	0.16
Total	100

The percentage reflectance characteristics of the CdS film are visualized in Fig. 3 as a function of wavelength. It is found that the magnitude of reflectance of the CdS film varies periodically with wavelength. Multiple oscillations occur on the reflectance curves due to interferences among multiple reflected waves. As the wavelength increases, the oscillation period of the film also changes. Thus, the reflectance characteristics of the CdS film are strongly dependent on the wavelength of

electromagnetic spectra. Highest peak value of 47.76 % occurred at 488 nm wavelength.

The percentage optical transmittance spectrum of 100 nm CdS film in the wavelength range from 400 to 800 nm is depicted in Fig. 4. The optical transmittance of CdS film increases from 69.35 % at 400 nm to 90 % at 658 nm wavelength. The result obtained is in agreement with the work of [18-19].

It is observed from the absorbance spectrum that the absorbance decreased with the increase in wavelength and found to be 0.165 at 400 nm wavelength (Fig. 5).

The optical band gap energies were evaluated by extrapolating the straight line of the Tauc plot for zero absorption coefficient ($\alpha = 0$). The optical energy band gap of 2.42 eV was obtained for the 100 nm CdS film (Fig. 6).

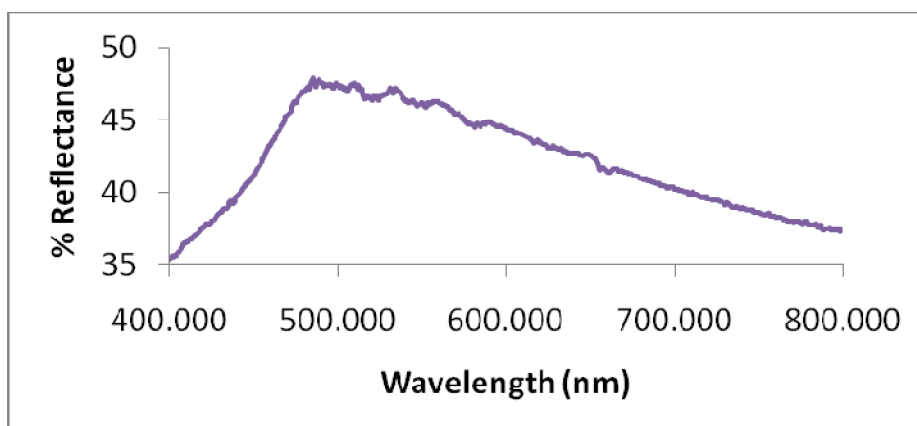


FIG. 3. % reflectance characteristics of 100 nm CdS film.

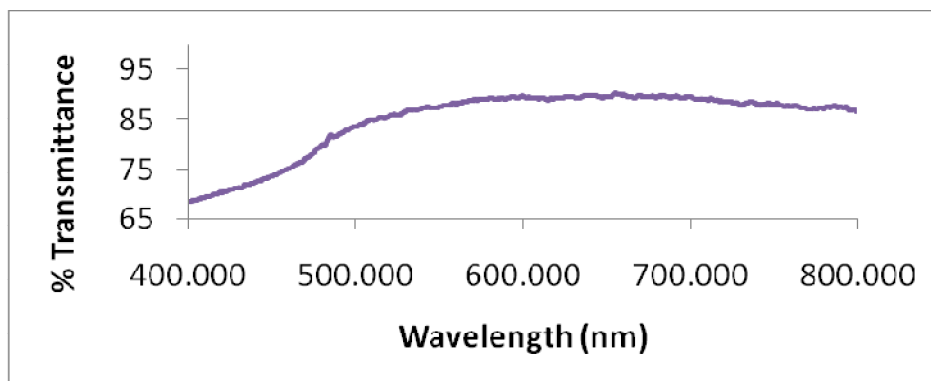


FIG. 4. % transmittance characteristics of 100 nm CdS film.

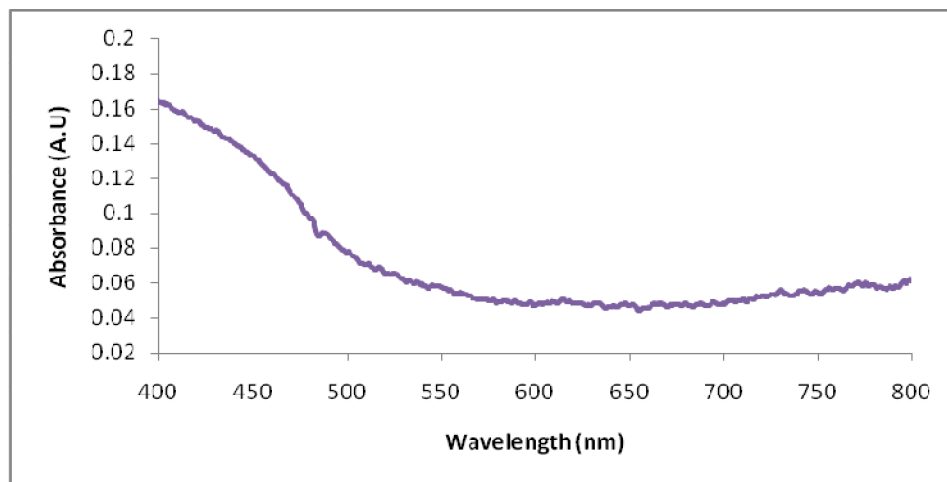


FIG. 5. % absorbance characteristics of 100 nm CdS film.

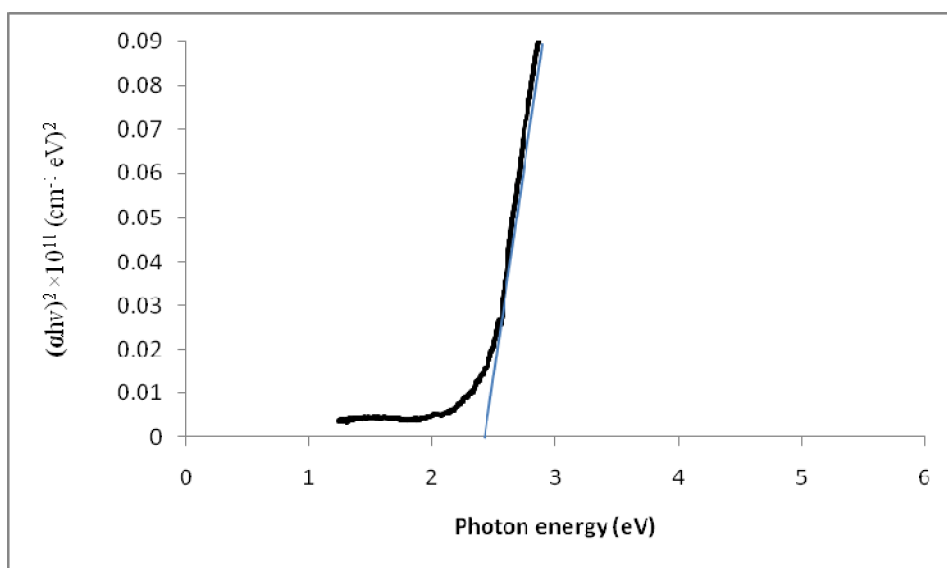


FIG. 6. Band gap of 100 nm CdS film.

FTIR spectrum of 100 nm CdS film is shown in Fig. 7. In the higher energy region, the absorption band at 3724 per cm is assigned to O-H stretching of absorbed water on the surface of CdS. The absorption band at 1446 per cm is assigned to bending vibration of methanol used in the process. It is also verified by its CH₃-stretching vibrations occurring as very weak just below 3000 per cm. The C-O stretching vibration of absorbed methanol gives its intense

absorption band at 1373 per cm. Its ring C-H vibration occurs at about 3000 per cm, though, it is very weak. Similar such weak absorption band due to C-H bending vibrations was also observed at about 617 per cm. Hence, in addition to absorbed methanol on the surface of CdS, the presence of thiophenol in its dissociation form is also evident. These observations convincingly support the template role of thiophenol in the control of the size of CdS particles.

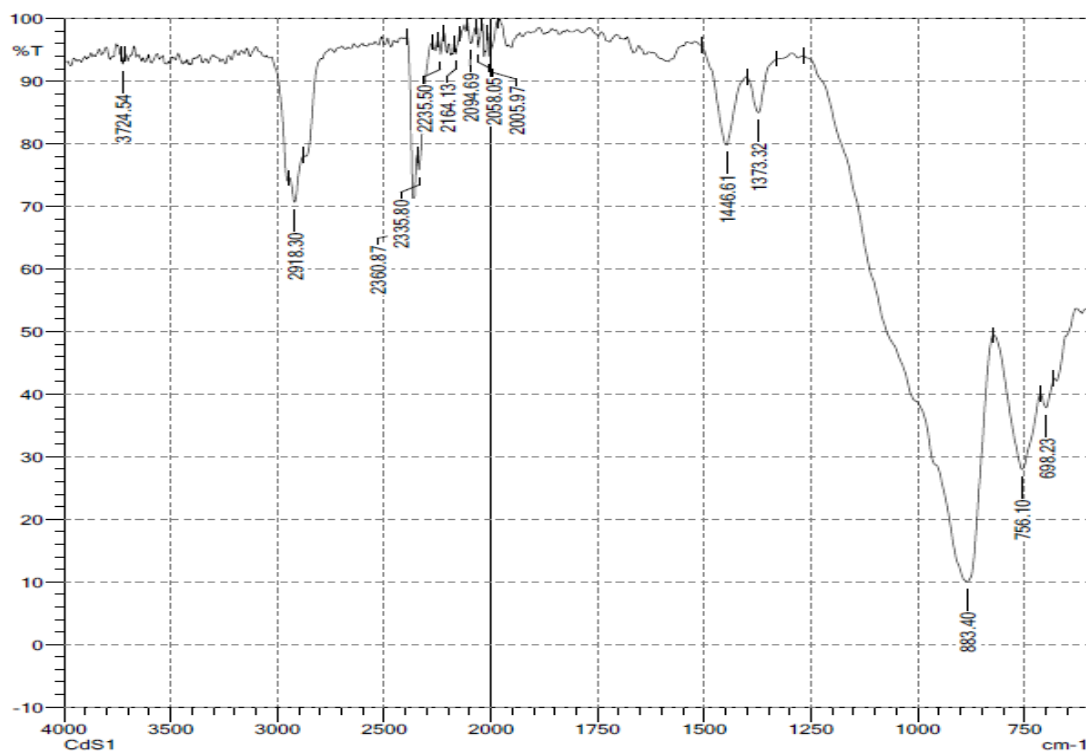


FIG. 7. FTIR for the 100 nm CdS film.

Conclusion

CdS nano-particles have been successfully prepared by chemical route method and identified by X-Ray Diffractometer (XRD). The peaks at 43° and 52° indicate that the nano-particles contain a mixture of hexagonal (wurtzite) and cubic (zincblende) structures which confirmed the greenockite and the Hawleyite phases of CdS. 100 nm CdS film deposited *via* thermal evaporation technique showed a high optical transmittance of 90 % at 658 nm wavelength and a reflectance of 47.76 %

at 488 nm wavelength. The absorbance of 0.165 A.U. was obtained at 400 nm wavelength and the optical energy band gap of 2.42 eV was deduced for the 100 nm CdS film from the Tauc plot. The Fourier Transform Infrared Radiation (FTIR) showed different peaks that indicate the stretching and vibrations of O-H, CH₃, C-O and C-H of CdS against their respective wave numbers. The prepared CdS can be employed as a window layer for the fabrication of CdS/CdTe thin film solar cells.

References

- [1] Antolini, F., Pentimalli, M., Di Luccio, T., Terzi, R., Schioppa, M., Re, M. and Tapfer, L., *Materials Letters*, 59 (24) (2005) 3181.
- [2] Bansal, P., Jaggi, N. and Rohilla, S.K., *Res. J. Chem. Sci.*, 2 (8) (2012) 69.
- [3] Huimin, C., Fuqiang, G. and Baohua, Z., *J. Semicond.*, 30 (5) (2009) 053001.
- [4] Shah, N.M., Shri, J.S.B. and Shri, K.M.B., *International Journal of Chem. Tech. Research CODEN (USA)*, 6 (3) (2014) 1959.
- [5] Djelloul, A., Adnane, M., Larbah, Y., Zerdali, M., Zegadi, C. and Messaoud, A., *Journal of Nano- and Electronic Physics*, 8 (2) (2016) 1.
- [6] Hasnat, A. and Podder, J., *Advances in Materials Physics and Chemistry*, 2 (2012) 226.
- [7] Ghasemi, Y., Peymani, P. and Afifi, S., *Acta Biomed.*, 80 (2009) 156.

- [8] Elmas, S., Ozcan, S., Ozder, S. and Bilgin, V., Proceedings of the International Congress on Advances in Applied Physics and Materials Science, Antalya 2011, 121 (2012) 1.
- [9] Obasuyi, A.R., Alabi, A.B., Babalola, O.A., Kajewole, E., Falana, F.H. and Robert, O., Ilorin Journal of Science, 1(1) (2014) 121.
- [10] Raj, F.M. and Rajendran, A.J., International Journal of Innovative Research in Science, Engineering and Technology, 4 (1) (2015) 56.
- [11] Sabah, A., Siddiqi, A.S. and Ali, S., World Academy of Science, Engineering and Technology, 69 (2010) 82.
- [12] Hepzi Pramila Devamani, R., Kiruthika, R., Mahadevi, P. and Sagithapriya, S., International Journal of Innovative Science, Engineering and Technology, 4 (1) (2017) 181.
- [13] Patra, S., Mitra, P. and Kumar, P.S., Materials Research, 14 (1) (2011) 17.
- [14] Manickathai, K., Kasi Viswanatham, S. and Alagar, M., Indian Journal of Pure and Applied Physics, 46 (2008) 561.
- [15] Alexander, N.J., Higashiya, S., Caskey, D., Efstathiadis, H. and Haldar, P., Solar Energy Materials and Solar Cells, 125 (2014) 47.
- [16] Patil, S.M. and Pawar, P.H., International Letters of Chemistry, Physics and Astronomy, 36 (2014) 153.
- [17] Mohammad, J.F., Al-jumaili, H.S. and Abed, S.M., International Journal of Application or Innovation in Engineering and Management (IJAIEM), 3 (5) (2014) 200.
- [18] Awodugba, A.O., Adedokun, O. and Sanusi, Y.K., IOSR Journal of Applied Physics, 6 (2) (2014) 34.
- [19] Naji, I.S., Khdayer, I.H. and Mohammed, H.I., International Journal of Application or Innovation in Engineering and Management (IJAIEM), 2 (6) (2013) 556.

Authors Index

A. B. ALABI	201
A.Kh. Suliman	153
Alaa Nassif	167
H. Saleh	193
L. D. Voelz	161
L. Özdemir	141
M. A. SALAWU	201
M. Al-Hwaiti	193
M. H. Saleh	181
M. Nairat	161
M. S. H. Aljuboori.	147
M. S. Hamideen	173, 193
M. S. Şadođlu	141
S. Al-Kharoof	193
S. B. SHARAF	201
T. AKOMOLAFE	201
W. Sahyouni	167

Subject Index

Activity utilization index	193
Bessel-Gaussian mode.....	161
Building stones	193
CdS.....	201
Cohesive energy.....	153
Compton scattering, , ,	161
Configuration interaction.....	141
CSP	147
Energies	141
Enthalpy.....	153
Forbidden transitions.....	141
Gamma-ray spectrometry.....	193
Hazard indices	193
Interband transition models.....	181
Laguerre-Gaussian mode	161
Lee model code.....	167
Melting point	153
Nanoparticles.....	153
Natural radioactivity	193
NiO	147
NX2 device	167
Optical constants	181
Optical properties	147
PbI ₂ films	181
Portland cement	173
Pozzolanic cement.....	173
PUMA method.....	181
Radiological hazards.....	173
Radiological risk	193
Relativistic effects	141
SEM	201
Size effects.....	153
Soft x-ray yield	167
Surface energy	153
Thin film.....	147
Twisted light.....	161
UV-visible spectrophotometer	201
Wemple-DiDomenico model.....	181
XRD.....	147,201

المراجع: يجب طباعة المراجع بأسطر مزدوجة ومرقمة حسب تسلسلها في النص. وتكتب المراجع في النص بين قوسين مربعين. ويتم اعتماد اختصارات الدوريات حسب نظام Wordlist of Scientific Reviewers.

الجدول: تعطى الجداول أرقاماً متسلسلة يشار إليها في النص. ويجب طباعة كل جدول على صفحة منفصلة مع عنوان فوق الجدول. أما الحواشي التفسيرية، التي يشار إليها بحرف فوقي، فتكتب أسفل الجدول.

الرسوم التوضيحية: يتم ترقيم الأشكال والرسومات والرسومات البيانية (المخططات) والصور، بصورة متسلسلة كما وردت في النص.

تقبل الرسوم التوضيحية المستخرجة من الحاسوب والصور الرقمية ذات النوعية الجيدة بالأبيض والأسود، على أن تكون أصيلة وليست نسخة عنها، وكل منها على ورقة منفصلة ومعرفة برقمها بالمقابل. ويجب تزويد المجلة بالرسومات بحجمها الأصلي بحيث لا تحتاج إلى معالجة لاحقة، وألا تقل الحروف عن الحجم 8 من نوع Times New Roman، وألا تقل سماكة الخطوط عن 0.5 وبكثافة متجانسة. ويجب إزالة جميع الألوان من الرسومات ما عدا تلك التي ستُنشر ملونة. وفي حالة إرسال الرسومات بصورة رقمية، يجب أن تتوافق مع متطلبات الحد الأدنى من التمايز (1200 dpi Resolution) لرسومات الأبيض والأسود الخطية، و 600 dpi للرسومات باللون الرمادي، و 300 dpi للرسومات الملونة. ويجب تخزين جميع ملفات الرسومات على شكل (jpg)، وأن ترسل الرسوم التوضيحية بالحجم الفعلي الذي سيظهر في المجلة. وسواء أرسل المخطوط بالبريد أو عن طريق الشبكة (Online)، يجب إرسال نسخة ورقية أصلية ذات نوعية جيدة للرسومات التوضيحية.

مواد إضافية: تشجع المجلة الباحثين على إرفاق جميع المواد الإضافية التي يمكن أن تسهل عملية التحكيم. وتشمل المواد الإضافية أي اشتقاقات رياضية مفصلة لا تظهر في المخطوط.

المخطوط المنقح (المعدل) والأقراص المدمجة: بعد قبول البحث للنشر وإجراء جميع التعديلات المطلوبة، فعلى الباحثين تقديم نسخة أصلية ونسخة أخرى مطابقة للأصلية مطبوعة بأسطر مزدوجة، وكذلك تقديم نسخة إلكترونية تحتوي على المخطوط كاملاً مكتوباً على Microsoft Word for Windows 2000 أو ما هو استجد منه. ويجب إرفاق الأشكال الأصلية مع المخطوط النهائي المعدل حتى لو تم تقديم الأشكال إلكترونياً. وتخزن جميع ملفات الرسومات على شكل (jpg)، وتقدم جميع الرسومات التوضيحية بالحجم الحقيقي الذي ستظهر به في المجلة. ويجب إرفاق قائمة ببرامج الحاسوب التي استعملت في كتابة النص، وأسماء الملفات على قرص مدمج، حيث يعلم القرص بالاسم الأخير للباحث، وبالرقم المرجعي للمخطوط للمراسلة، وعنوان المقالة، والتاريخ. ويحفظ في مغلف واقٍ.

حقوق الطبع

يُشكّل تقديم مخطوط البحث للمجلة اعترافاً صريحاً من الباحثين بأن مخطوط البحث لم يُنشر ولم يُقدّم للنشر لدى أي جهة أخرى كانت وبأي صيغة ورقية أو إلكترونية أو غيرها. ويشتترط على الباحثين ملء نموذج ينص على نقل حقوق الطبع لتصبح ملكاً لجامعة البرموك قبل الموافقة على نشر المخطوط. ويقوم رئيس التحرير بتزويد الباحثين بإنموذج نقل حقوق الطبع مع النسخة المرسلّة للتنقيح. كما ويمنع إعادة إنتاج أي جزء من الأعمال المنشورة في المجلة من دون إذن خطّي مُسبق من رئيس التحرير.

إخلاء المسؤولية

إن ما ورد في هذه المجلة يعبر عن آراء المؤلفين، ولا يعكس بالضرورة آراء هيئة التحرير أو الجامعة أو سياسة اللجنة العليا للبحث العلمي أو وزارة التعليم العالي والبحث العلمي. ولا يتحمل ناشر المجلة أي تبعات مادية أو معنوية أو مسؤوليات عن استعمال المعلومات المنشورة في المجلة أو سوء استعمالها.

الفهرسة: المجلة مفهرسة في:

 ULRICHSWEB™ GLOBAL SERIALS DIRECTORY	Emerging Sources Citation Index (ESCI)	
--	---	---

معلومات عامة

المجلة الأردنية للفيزياء هي مجلة بحوث علمية عالمية متخصصة مُحكمة تصدر بدعم من صندوق دعم البحث العلمي، وزارة التعليم العالي والبحث العلمي، عمان، الأردن. وتقوم بنشر المجلة عمادة البحث العلمي والدراسات العليا في جامعة اليرموك، إربد، الأردن. وتُنشر البحوث العلمية الأصلية، إضافة إلى المراسلات القصيرة Short Communications، والملاحظات الفنية Technical Notes، والمقالات الخاصة Feature Articles، ومقالات المراجعة Review Articles، في مجالات الفيزياء النظرية والتجريبية، باللغتين العربية والإنجليزية.

تقديم مخطوط البحث

تقدم البحوث عن طريق إرسالها إلى البريد الإلكتروني : jjp@yu.edu.jo

تقديم المخطوطات إلكترونياً: اتبع التعليمات في موقع المجلة على الشبكة العنكبوتية.

ويجري تحكيم البحوث الأصلية والمراسلات القصيرة والملاحظات الفنية من جانب مُحكمين اثنين في الأقل من ذوي الاختصاص والخبرة. وتُشجّع المجلة الباحثين على اقتراح أسماء المحكمين. أما نشر المقالات الخاصة في المجالات الفيزيائية النشطة، فيتم بدعوة من هيئة التحرير، ويُشار إليها كذلك عند النشر. ويُطلب من كاتب المقال الخاص تقديم تقرير واضح يتسم بالدقة والإيجاز عن مجال البحث تمهيداً للمقال. وتُنشر المجلة أيضاً مقالات المراجعة في الحقول الفيزيائية النشطة سريعة التغير، وتُشجّع كاتبي مقالات المراجعة أو مُستكثبيها على إرسال مقترح من صفحتين إلى رئيس التحرير. ويُرفق مع البحث المكتوب باللغة العربية ملخص (Abstract) وكلمات دالة (Keywords) باللغة الإنجليزية.

ترتيب مخطوط البحث

يجب أن تتم طباعة مخطوط البحث بنظ 12 نوعه Times New Roman، وبسطر مزدوج، على وجه واحد من ورق A4 (21.6 × 27.9 سم) مع حواشي 3.71 سم، باستخدام معالج كلمات ميكروسوفت وورد 2000 أو ما استُجد منه. ويجري تنظيم أجزاء المخطوط وفق الترتيب التالي: صفحة العنوان، الملخص، رموز التصنيف (PACS)، المقدمة، طرق البحث، النتائج، المناقشة، الخلاصة، الشكر والعرفان، المراجع، الجداول، قائمة بدليل الأشكال والصور والإيضاحات، ثم الأشكال والصور والإيضاحات. وتُكتب العناوين الرئيسية بخط غامق، بينما تُكتب العناوين الفرعية بخط مانل.

صفحة العنوان: وتشمل عنوان المقالة، أسماء الباحثين الكاملة وعناوين العمل كاملة. ويكتب الباحث المسؤول عن المراسلات اسمه مشاراً إليه بنجمة، والبريد الإلكتروني الخاص به. ويجب أن يكون عنوان المقالة موجزاً وواضحاً ومعبراً عن فحوى (محتوى) المخطوط، وذلك لأهمية هذا العنوان لأغراض استرجاع المعلومات.

الملخص: المطلوب كتابة فقرة واحدة لا تزيد على مائتي كلمة، موضحة هدف البحث، والمنهج المتبع فيه والنتائج وأهم ما توصل إليه الباحثون.

الكلمات الدالة: يجب أن يلي الملخص قائمة من 4-6 كلمات دالة تعبر عن المحتوى الدقيق للمخطوط لأغراض الفهرسة.

PACS: يجب إرفاق الرموز التصنيفية، وهي متوافرة في الموقع <http://www.aip.org/pacs/pacs06/pacs06-toc.html>.

المقدمة: يجب أن توضّح الهدف من الدراسة وعلاقتها بالأعمال السابقة في المجال، لا أن تكون مراجعة مكثفة لما نشر (لا تزيد المقدمة عن صفحة ونصف الصفحة مطبوعة).

طرائق البحث (التجريبية / النظرية): يجب أن تكون هذه الطرائق موضحة بتفصيل كاف لإتاحة إعادة إجرائها بكفاءة، ولكن باختصار مناسب، حتى لا تكون تكراراً للطرائق المنشورة سابقاً.

النتائج: يستحسن عرض النتائج على صورة جداول وأشكال حيثما أمكن، مع شرح قليل في النص ومن دون مناقشة تفصيلية.

المناقشة: يجب أن تكون موجزة وتركز على تفسير النتائج.

الاستنتاج: يجب أن يكون وصفاً موجزاً لأهم ما توصلت إليه الدراسة ولا يزيد عن صفحة مطبوعة واحدة.

الشكر والعرفان: الشكر والإشارة إلى مصدر المنح والدعم المالي يكتبان في فقرة واحدة تسبق المراجع مباشرة.

Subscription Form

Jordan Journal of
PHYSICS

An International Peer-Reviewed Research Journal issued by the
Support of the Scientific Research Support Fund

Published by the Deanship of Research & Graduate Studies, Yarmouk University, Irbid, Jordan

Name: الأسم:
Specialty:..... التخصص:
Address: العنوان:
P.O. Box:..... صندوق البريد:
City & Postal Code: المدينة/الرمز البريدي:
Country: الدولة:
Phone: رقم الهاتف:
Fax No:..... رقم الفاكس:
E-mail:..... البريد الإلكتروني:
No. of Subscription: عدد الاشتراكات:
Method of Payment:..... طريقة الدفع:
Amount Enclosed:..... المبلغ المرفق:
Signature: التوقيع:

Cheques should be paid to Deanship of Research and Graduate Studies - Yarmouk University.

I would like to subscribe to the Journal
For

- One Year
 Two Years
 Three Years

One Year Subscription Rates

	Inside Jordan	Outside Jordan
Individuals	JD 8	€ 40
Students	JD 4	€ 20
Institutions	JD 12	€ 60

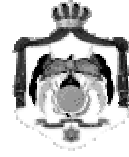
Correspondence

Subscriptions and Sales:

Prof. Ibrahim O. Abu Al-Jarayesh
Deanship of Research and Graduate Studies
Yarmouk University
Irbid – Jordan
Telephone: 00 962 2 711111 Ext. 2075
Fax No.: 00 962 2 7211121



جامعة اليرموك



المملكة الأردنية الهاشمية

المجلة الأردنية
للفيزياء

مجلة بحوث علمية عالمية متخصصة محكمة
تصدر بدعم من صندوق دعم البحث العلمي

المجلة الأردنية
للفيزياء
مجلة بحوث علمية عالمية محكمة

المجلد (11)، العدد (3)، كانون الأول 2018م / ربيع الآخر 1440هـ

المجلة الأردنية للفيزياء: مجلة علمية عالمية متخصصة محكمة تصدر بدعم من صندوق دعم البحث العلمي، عمان، الأردن، وتصدر عن عمادة البحث العلمي والدراسات العليا، جامعة اليرموك، إربد، الأردن.

رئيس التحرير:

ابراهيم عثمان أبو الجرايش
قسم الفيزياء، جامعة اليرموك، إربد، الأردن.
ijaraysh@yu.edu.jo

هيئة التحرير:

ضياء الدين محمود عرفة
قسم الفيزياء، الجامعة الأردنية، عمان، الأردن.
darafah@ju.edu.jo

نبيل يوسف أيوب
رئيس الجامعة الأمريكية في مادبا، مادبا، الأردن.
nabil.ayoub@gju.edu.jo

جميل محمود خليفة
قسم الفيزياء، الجامعة الأردنية، عمان، الأردن.
jkalifa@ju.edu.jo

سامي حسين محمود
قسم الفيزياء، الجامعة الأردنية، عمان، الأردن.
s.mahmood@ju.edu.jo

نهاد عبدالرؤوف يوسف
قسم الفيزياء، جامعة اليرموك، عمان، الأردن.
nihadyusuf@yu.edu.jo

مروان سليمان موسى
قسم الفيزياء، جامعة مؤتة، الكرك، الأردن.
mmousa@mutah.edu.jo

أكرم عبد المجيد الروسان
قسم الفيزياء التطبيقية، جامعة العلوم والتكنولوجيا الأردنية، إربد، الأردن.
akram@just.edu.jo

محمد خالد الصغير
قسم الفيزياء، الجامعة الهاشمية، الزرقاء، الأردن.
msugh@hu.edu.jo

سكرتير التحرير: مجدي الشناق

ترسل البحوث إلى العنوان التالي:

الأستاذ الدكتور إبراهيم عثمان أبو الجرايش
رئيس تحرير المجلة الأردنية للفيزياء
عمادة البحث العلمي والدراسات العليا، جامعة اليرموك
إربد، الأردن

هاتف 00 962 2 7211111 فرعي 2075

E-mail: jpp@yu.edu.jo Website: <http://Journals.yu.edu.jo/jpp>